# Geometry and Precision in Sentinel-1 Processing for Interferometric Applications

Roland Akiki

## ▶ To cite this version:

Roland Akiki. Geometry and Precision in Sentinel-1 Processing for Interferometric Applications. Image Processing [eess.IV]. Université Paris-Saclay, 2023. English. NNT : 2023UPASM029 . tel-04639008

HAL Id: tel-04639008
https://theses.hal.science/tel-04639008v1

Submitted on 8 Jul 2024

**HAL** is a multi-disciplinary open access archive for the deposit and dissemination of scientific research documents, whether they are published or not. The documents may come from teaching and research institutions in France or abroad, or from public or private research centers.

L'archive ouverte pluridisciplinaire **HAL**, est destinée au dépôt et à la diffusion de documents scientifiques de niveau recherche, publiés ou non, émanant des établissements d'enseignement et de recherche français ou étrangers, des laboratoires publics ou privés.

# Geometry and Precision in Sentinel-1 Processing for Interferometric Applications

*Géométrie et Précision dans le Traitement de Sentinel-1 pour des Applications Interférométriques*

**Thèse de doctorat de l'Université Paris-Saclay**

École doctorale n° 574, mathématiques Hadamard (EDMH)
Spécialité de doctorat : Mathématiques aux interfaces
Graduate School : Mathématiques. Référent : ENS Paris-Saclay

Thèse préparée dans l'unité de recherche **Centre Borelli (Université Paris-Saclay, CNRS, ENS Paris-Saclay)**,
sous la direction de **Jean-Michel Morel**, Professeur,
et la co-direction de **Gabriele Facciolo**, Professeur,
et la co-direction de **Raphaël Grandin**, Maître de Conférences HDR,
et le co-encadrement de **Carlo de Franchis**, VP Remote Sensing Kayrros

**Thèse soutenue à Paris-Saclay, le 15 décembre 2023, par**

## Roland Akiki

**Composition du jury**

Membres du jury avec voix délibérative

| | |
|---|---|
| **Florence Tupin**<br>Professeure, Télécom Paris, Institut Polytechnique de Paris | Rapporteur & Présidente |
| **Emmanuel Trouvé**<br>Professeur, Université Savoie Mont Blanc, Polytech Annecy-Chambéry | Rapporteur & Examinateur |
| **Dinh Ho Tong Minh**<br>Chargé de Recherche HDR, Institute for Agriculture, Food and Environment (INRAE) | Examinateur |
| **Muriel Pinheiro**<br>Sentinel-1 Data Quality Manager - European Space Agency (ESA) - ESRIN | Examinatrice |

THESE DE DOCTORAT

NNT : 2023UPASM029

université PARIS-SACLAY
ÉCOLE DOCTORALE
de mathématiques
Hadamard (EDMH)

**Titre:** Géométrie et Précision dans le Traitement de Sentinel-1 pour des Applications Interférométriques

**Mots clés:** Interférométrie, Géométrie, Précision, Sentinel-1, Double différence de phase, Déformation

**Résumé:** Cette thèse explore les techniques avancées de traitement des données du radar à synthèse d'ouverture (RSO, ou SAR en anglais) du satellite Sentinel-1 et se concentre sur les questions liées à la précision, à la géométrie et à l'efficacité avec des applications à l'interférométrie (InSAR). La première partie de la thèse étudie le recalage et la modélisation géométrique de Sentinel-1. Tout d'abord, nous comparons différentes approches de *deramping* pour Sentinel-1 et mettons en évidence les compromis entre efficacité et précision. Ensuite, nous appliquons avec succès un algorithme pour estimer les modèles de caméra RPC à partir de correspondances de points 3D-2D sur les images Sentinel-1 et Wordlview-3. Le dernier chapitre de la première partie propose une méthode pour améliorer la précision de l'assemblage des *bursts* de Sentinel-1 et du recalage géométrique en tenant compte des corrections fines du modèle de géolocalisation. Il en résulte une série temporelle de mosaïques Sentinel-1 bien alignées et géométriquement cohérentes. La deuxième partie de la thèse évalue la performance des méthodes d'apprentissage profond existantes pour les tâches InSAR telles que le débruitage de phase, l'estimation de la cohérence et le déroulement de phase. La dernière partie présente une application InSAR sur les cuves de stockage de pétrole brut. Nous montrons la corrélation entre la double différence de la phase InSAR sur les réflecteurs fixes voisins des cuves et la double différence du taux de remplissage des cuves. Nos résultats indiquent que les réflecteurs sur le toit d'une cuve s'éloignent du satellite d'environ 1 cm lorsqu'elle se remplit. Notre étude souligne la nécessité d'exigences strictes en matière de précision et de traitement de certaines applications InSAR localisées. En conclusion, ce travail met en évidence les aspects liés à la géométrie et à la précision du traitement de Sentinel-1, qui pourraient bénéficier à la fois aux applications SAR et InSAR à grande échelle et localisées.

**Title:** Geometry and Precision in Sentinel-1 Processing for Interferometric Applications

**Keywords:** Interferometry, Geometry, Precision, Sentinel-1, Double phase difference, Deformation

**Abstract:** This thesis explores advanced techniques for processing Sentinel-1 Synthetic Aperture Radar (SAR) data and focuses on questions related to precision, geometry, and efficiency with applications to interferometry (InSAR). The first part of the thesis studies the coregistration and geometric modeling of Sentinel-1. First, we compare different deramping approaches for Sentinel-1 and highlight the tradeoffs between efficiency and precision. Then, we successfully apply an algorithm to fit RPC camera models from 3D-2D point correspondences on Sentinel-1 and Wordlview-3 images. The last chapter in the first part proposes a method to improve the precision of Sentinel-1 burst stitching and geometric coregistration by accounting for fine corrections of the geolocation model. This results in a time series of well-aligned, geometrically consistent Sentinel-1 mosaics. The second part of the thesis evaluates the performance of existing deep learning methods for InSAR tasks such as phase denoising, coherence estimation, and phase unwrapping. The last part presents an InSAR application on crude oil storage tanks. We show the correlation between the double difference of the InSAR phase on neighboring fixed reflectors on the tanks and the double difference of the tanks' fill ratio. Our results indicate that the reflectors on the roof of a tank move away from the satellite by around 1 cm when it fills up. Our study underlines the need for stringent requirements on the precision and processing of some localized InSAR applications. In conclusion, in this work, we highlight aspects related to the geometry and the precision of Sentinel-1 processing, which could benefit both wide-area and localized SAR and InSAR applications.

# Remerciements

Je tiens à exprimer ma profonde gratitude envers mon directeur de thèse, Jean-Michel Morel, ainsi que mes codirecteurs, Gabriele Facciolo, Raphaël Grandin et Carlo de Franchis. Votre soutien inestimable a été déterminant pour mon intégration au Centre Borelli et à Kayrros, pour l'obtention du financement nécessaire, ainsi que pour la navigation des démarches administratives dans une période compliquée marquée par la pandémie de COVID-19. Je suis particulièrement reconnaissant pour le temps que vous avez généreusement consacré à nos réunions régulières, qui ont été à la fois enrichissantes et cruciales pour l'avancement de nos recherches. Je tiens également à remercier Raphaël pour m'avoir accueilli à l'IPGP, pour m'avoir accordé un accès à la chaîne de traitement NSBAS, et pour avoir partagé son expertise précieuse en matière de traitements interférométriques avec Sentinel-1.

Je souhaite exprimer ma sincère reconnaissance envers Florence Tupin et Emmanuel Trouvé d'avoir accepté d'être les rapporteurs de ma thèse, ainsi qu'envers les membres du jury, Muriel Pinheiro et Dinh Ho Tong Minh. C'est un privilège immense de pouvoir vous présenter mes travaux.

Un grand merci à tous les membres du Centre Borelli, avec qui j'ai partagé des moments inoubliables au cours de ces années. Travailler et participer à des séminaires tels que le groupe de travail sur le traitement d'images et le séminaire MLBriefs a été un véritable plaisir. Je tiens à remercier tout particulièrement Roger Marí Molas, Jérémy Anger et Axel Davy pour leur dévouement exceptionnel et leur excellence dans nos recherches communes. Je remercie aussi l'équipe administrative et l'ensemble des membres du secrétariat du Centre Borelli pour leur accompagnement durant les démarches diverses et les missions.

Mes remerciements s'adressent également à Alexandre d'Aspremont, Benjamin Dubois-Taine, Houssem Ouled Alaya et Alexandre Achard de Lustrac, avec qui j'ai exploré des thématiques cruciales relatives au déroulement de phase, ainsi qu'aux étudiants du master MVA que j'ai eu le privilège de co-encadrer dans des projets liés à l'InSAR.

Je tiens à exprimer ma gratitude envers mes collègues chez Kayrros pour leur accueil chaleureux, en particulier les membres actuels et anciens de mon équipe "rs-geo-mlops". Vous m'avez appris à manier les outils de Kayrros, facilité l'accès aux images SAR, présenté des études de cas fascinantes, et vos commentaires et conseils lors de nos réunions ont été inestimables. Les repas et les moments agréables partagés ensemble ont également été grandement appréciés.

Je remercie l'ANRT pour avoir financé cette thèse par le biais du dispositif CIFRE, qui m'a offert une expérience professionnelle précieuse tout au long de ma thèse. J'ai également eu le privilège de participer à plusieurs conférences, notamment IGARSS 2019-2023, MDIS 2022 à Ax-les-Thermes, et FRINGE 2023 à Leeds. Ma visite à Duke University pendant quelques semaines a été une expérience enrichissante, et je remercie chaleureusement Guillermo Sapiro, Matias di Martino et l'équipe de Duke pour leur accueil exceptionnel.

Enfin, ma famille et mes amis méritent une mention spéciale pour leur soutien indéfectible au cours de ces années de recherche. Chaque moment passé avec vous a été une source de motivation et d'inspiration inestimable.

# Contents

# 1 Introduction

## 1.1 Motivation

A Synthetic Aperture Radar (SAR) imaging device is an active system. It is usually composed of an antenna mounted on a spaceborne or airborne platform. The antenna emits electromagnetic (EM) pulses in a side-looking geometry and then receives echoes that are backscattered on the ground surface. Radar waves with a carrier wavelength $\lambda \in [1 - 20]$ cm experience minimal interactions with atmospheric gases or aerosols, rendering the propagation medium transparent and non-absorbing. Thus, unlike optical sensors, SAR has day-night cloud-penetrating imaging capacities.

The SAR signal is a complex number, where the amplitude is related to the ground reflectivity and the phase contains information about the satellite-target path delay. Therefore, under certain constraints on the acquisition configuration, it is possible to perform Interferometric SAR (InSAR). This technique consists of comparing the phase of at least two SAR images of the same area from slightly different viewing positions to deduce information about the ground topography (metric precision) and deformation (millimetric precision). More precisely, Differential InSAR (DInSAR) uses InSAR to measure the deformation from repeat-pass acquisitions of the same area at different times.

Throughout the years, this technique has proved to be very useful in fields such as volcanology, seismology, glaciology, ground subsidence and uplift. In recent years, there has been a substantial increase in the InSAR data availability, namely thanks to the full, free and open data policy of the Copernicus programme, including in particular Sentinel-1 SAR data since the beginning of the mission in 2014. Until the recent failure of Sentinel-1B in December 2021, Sentinel-1 consisted of a constellation of two identical polar-orbiting satellites (A and B) with a combined repeat cycle of 6 days (12 days each) allowing for a nearly global coverage of the Earth [PINYM+17, PMR+22]. With this amount of data acquired and distributed, it is of the utmost importance to improve our processing algorithms and achieve a good tradeoff between precision and efficiency.

Considering that the Sentinel-1 images are distributed as products that span hundreds of kilometers and that a datatake usually consists of many consecutive products that can be concatenated, there has been a legitimate growing interest in Wide Area Processing (WAP) algorithms [AGPB13, MDZ+19, LSG+20, TCD+21, CSM+20]. In this case, the goal is usually to observe medium to large-scale deformation phenomena, and this is reflected in the processing which performs numerous filtering operations and often contains some interpolations and/or undersampling. However, for some applications, it is also interesting to be able to perform localized processing on many small areas all over the world. This is the case of the monitoring of specific assets, such as the crude oil storage tank use case explored in Chapter 8. In contrast with the WAP, one could argue that the requirements for precise processing and modeling should be more stringent, because of the need to extract insights from a few pixels on the asset.

The idea of localized InSAR processing is not new and is in fact more intuitive since the most atomic InSAR measurement is a relative phase difference between neighboring points in the image. This has actually been explored mainly through the full-resolution *Persistent Scatterer* (PS) processing [CMCG+16]. However, even in this case, many filters with smoothness assumptions are used, which brings into question the spatio-temporal independence of the final estimated deformation, and the amount of processing-induced correlations. Another goal of this research is to contribute to the automation of the processing chain, where results can be produced fully with no human intervention. Since one of the ways to achieve this goal might involve machine learning in the future, we explore some of the deep learning models that are available today to perform some InSAR tasks such as phase unwrapping or phase denoising.

This thesis has been conducted at Kayrros, an environmental intelligence company, which measures the impact of human activity on the environment with satellite-based technology. The work conducted has mainly led to advancement in SAR processing algorithms, the filing of two patents [AAdF+nt,AdFF+nt], and a Python package called EOS-SAR (Earth Observation and Sensing - SAR). At Kayrros, these algorithms are routinely used in R&D activities, and various products are being developed for applications such as crude oil storage monitoring. It has also attracted the attention of various researchers among our collaborators, who have started to use EOS-SAR for their work [HG23].

## 1.2 SAR and InSAR processing

In this section, we delve into key concepts in SAR and InSAR processing. We begin by exploring the fundamentals of SAR image acquisition and formation, followed by an introduction to interferometry. We then examine the SAR camera model, discuss coregistration, and introduce the concept of differential interferometry. Lastly, we present advanced techniques in differential interferometry.

### 1.2.1 SAR acquisition and image formation

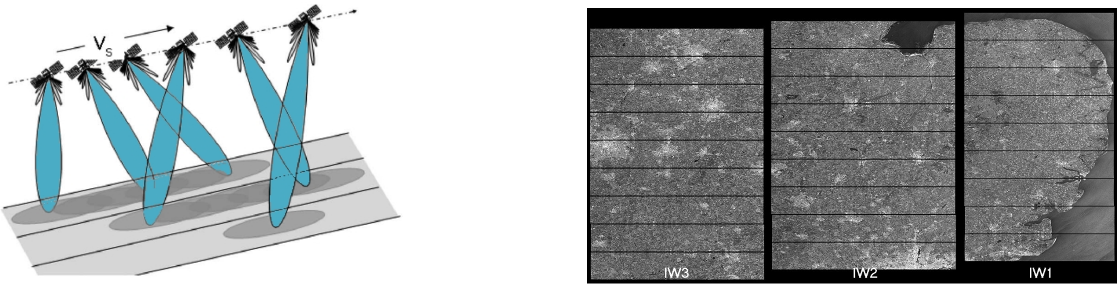

Figure 1.1: The TOPSAR acquisition, taken from [web]. On the left, we see how the EM pulses are sent, with a continuous rotation of the EM beam in the along-track direction and overlapping footprints. We also see the instantaneous rotation of the beam in the across-track direction to acquire the different swaths. An actual Sentinel-1 IW image is shown on the right, with multiple bursts in each of the 3 swaths IW1, IW2, and IW3.

In this section, we briefly revisit the SAR acquisition process and image formation as shown in Figure 1.1. More details can be found in [CW05]. The satellite flight direction is called along-track or azimuth, while the direction of the beam is called across-track or range. At each azimuth pulse repetition interval (PRI), an EM pulse is sent and then the satellite receives the echoes, demodulates (removes the carrier), samples them at a range sampling frequency, orders them by range, and stores them as complex numbers by separately extracting amplitudes in-phase and quadrature components of the signal. The resulting image is in the raw format (often designated as Level 0 or L0). Because of the large footprint of the electromagnetic beam, and because of the length of the pulse that was sent, in this format, the response from a single scatterer on the ground is spread over many pixels and the data resolution is very low. The resolution can be improved through a process known as focusing, which yields a Single Look Complex (SLC) image at processing Level 1 (L1). To understand focusing, it is beneficial to study the pulse compression of a simple one-dimensional chirp. Consider that the sent signal is a chirp of length $T$ seconds with a chirp rate of $K$

$$s(t) = \mathrm{rect}\left(\frac{t}{T}\right)\exp\{j\pi K t^2\}, \tag{1.1}$$

where $t$ is the time and

$$\mathrm{rect}(x) = \begin{cases} 1 & \text{if } |x| \leq 0.5 \\ 0 & \text{otherwise.} \end{cases} \tag{1.2}$$

This chirp is characterized by a frequency that varies linearly with time

$$f_{chirp}(t) = \frac{1}{2\pi}\frac{\partial\{\pi K t^2\}}{\partial t} = Kt \quad \text{(Hz)}. \tag{1.3}$$

Since $t \in [-T/2, T/2]$, the central frequency at $t = 0$ is $f_{chirp}(0) = 0$ Hz, and the chirp is considered a baseband signal.

Consider that the received signal is equal to the sent signal with a delay of $t_0$:

$$s_r(t) = \mathrm{rect}\left(\frac{t-t_0}{T}\right)\exp\{j\pi K(t-t_0)^2\}. \tag{1.4}$$

We define a matched filter as the time-reversed, complex conjugate of s(t):

$$h(t) = \mathrm{rect}\left(\frac{t}{T}\right)\exp\{-j\pi K t^2\}. \tag{1.5}$$

The output of pulse compression is defined by the convolution:

$$s_{out}(t) = s_r(t) \otimes h(t) = \int_{-\infty}^{+\infty} s_r(u)h(t-u)du \propto \mathrm{sinc}\{KT(t-t_0)\}, \tag{1.6}$$

where

$$\mathrm{sinc}(x) = \frac{\sin(\pi x)}{\pi x}. \tag{1.7}$$

It is clear from the following equations how the received chirp of length T was compressed to a cardinal sine whose 3 dB (decibel) width is $\frac{0.886}{|K|T}$. The compression factor is $\approx |K|T^2$. This principle is behind the image resolution enhancement during focusing. Now consider a non-baseband signal, which can be viewed as one in which the time of zero frequency is offset from the pulse center by $t_c$:

$$s(t) = \text{rect}\left(\frac{t}{T}\right)\exp\{j\pi K(t-t_c)^2\}. \tag{1.8}$$

The frequency of the signal is in this case $f_{chirp}(t) = K(t-t_c)$ for $t \in [-T/2, T/2]$, and the central frequency is $f_c = f_{chirp}(0) = -Kt_c$. By following the same reasoning as previously, the compressed signal will be written as

$$s_{out}(t) \propto \exp\{j2\pi f_c(t-t_0-t_c)\}\,\text{sinc}\{KT(t-t_0-t_c)\}. \tag{1.9}$$

Notice the presence of a linear phase ramp $2\pi f_c(t-t_0-t_c)$ centered at the peak of the sinc, with a slope proportional to $f_c$ (the central frequency of the chirp). For more details on pulse compression, see Chapter 3 of [CW05].

In practice, during a SAR acquisition, each pulse sent is a chirp in range time $\tau$ with a chirp rate of $K_r$. Therefore, each pulse can be compressed into a cardinal sine in the range dimension.

As for the azimuth dimension, we can also prove that there is a chirp in this direction. Consider a single-point target located on the ground and a satellite platform progressing at speed $v$ in the rectilinear geometry. The plane that contains the sensor and is orthogonal to the sensor velocity vector is known as the Zero-Doppler plane as shown in Figure 1.2. The Zero-Doppler time is the time when the Zero-Doppler plane crosses the target. Let $R(\eta)$ be the range (the sensor-target distance) at a specific azimuth time $\eta$ measured with respect to the Zero-Doppler time of the target. $\text{R} = R(0)$ is the range at the Zero-Doppler time, also known as the range of closest approach. Using the Pythagorean theorem, we can write

$$R(\eta) = \sqrt{\text{R}^2 + v^2\eta^2} \approx \text{R} + \frac{v^2\eta^2}{2\text{R}}. \tag{1.10}$$

The previous equation is known as the hyperbolic range equation. Without going into the details of the derivation (see Equation 4.42 in [CW05]), Equation 1.11 shows the expression of one of the phase components present in the impulse response of the raw target:

$$\Phi_{dop} = \frac{-4\pi R(\eta)}{\lambda} \approx \frac{-4\pi}{\lambda}\left(\text{R} + \frac{v^2\eta^2}{2\text{R}}\right). \tag{1.11}$$

Therefore, the raw phase of a target exhibits a quadratic evolution with respect to the azimuth time $\eta$, i.e., a chirp is also present in azimuth and can be compressed as well. This is the basis of the Synthetic Aperture Radar concept, in which the responses of the different pulses along the azimuth are combined in a way that emulates a larger synthetic antenna aperture. Another remark is about the Doppler designation in azimuth. This analogy comes from the fact that the chirp whose frequency is linearly varying with azimuth time can be seen as a Doppler effect since the platform is approaching the target before the Zero-Doppler time and is leaving it afterward. In fact, the Doppler shift can be written as

$$f_{dop} = \frac{1}{2\pi}\frac{\partial\Phi_{dop}}{\partial\eta} = \frac{-2}{\lambda}\frac{\partial R(\eta)}{\partial\eta} \approx \frac{-2v^2\eta}{\lambda\text{R}} = K_a\eta, \tag{1.12}$$

where $K_a = \frac{-2v^2}{\lambda\text{R}}$ is the azimuth Doppler rate.

If the center of the EM beam is pointing in the Zero-Doppler plane, it is said to have no squint angle, and the chirp in azimuth is a baseband signal. When it is pointing forward or backward with a squint angle, the center of the chirp is at a time $\eta_c$ (beam center crossing time), and we obtain a non-baseband chirp. The Doppler centroid frequency at this time will no longer be zero and will be equal to $f_{DC} = K_a \eta_c$, and as previously seen in Equation 1.9 for pulse compression, this will induce a linear phase term in the focused data with a slope of $2\pi f_{DC}$.

For Sentinel-1, the SAR images can be acquired with different modes. The most common acquisition mode shown in Figure 1.1 is the Interferometric Wide (IW) swath mode, which uses the Terrain Observation with Progressive Scans SAR (TOPS, or TOPSAR) technique. The data is acquired by bursts, and during the acquisition of a single burst, the EM beam is rotated with azimuth time from a backward-pointing to a forward-pointing position. Since this is a squinted acquisition with a uniform rotation rate of the beam, the Doppler centroid $f_{DC}$ can be considered linear with the azimuth time. Thus, the focused data will contain a phase term, which in this case is quadratic with azimuth time. Understanding this concept is crucial to manipulate SAR images since it affects how we resample this type of data as can be seen in Chapter 3, and imposes high co-registration accuracy requirements in azimuth as will be explained in Section 1.2.4.

The presence of the previously detailed phase ramp needs to be often considered for processing purposes but will be dropped from the following InSAR equations in this chapter to simplify the notation. Indeed, the main phase component of interest in the focused SAR image is related to the target-satellite Zero-Doppler distance R as can be seen in the following simplified Equation

$$\Gamma = A \exp\{j\Phi\} = A \exp\left\{ j \left( \frac{-4\pi \mathrm{R}}{\lambda} + \zeta \right) \right\}, \tag{1.13}$$

where $A$ is the amplitude of the SAR image, and $\zeta$ is the phase related to the scattering shift due to the interactions of the microwave with the targets.

One final concept is the intensity $I = \|\Gamma\|^2 = A^2$, which is the amplitude squared. The intensity is sometimes used instead of the amplitude because of some advantages related to noise modeling ( [TN15]) and the spectral characterization of the signal in the Fourier domain (see point target analysis and concepts of power detection and magnitude detection in [CW05]).

### 1.2.2 Interferometry

When at least two aligned (coregistered) SAR acquisitions $\Gamma_1$, $\Gamma_2$ of the same scene are available, they can be combined to form an interferogram as can be seen in the following Equation

$$\Gamma_{12} = \Gamma_1 \times \Gamma_2^* = A_1 A_2 \exp\{j(\Phi_1 - \Phi_2)\} = A_1 A_2 \exp\left\{ -j\frac{4\pi}{\lambda}(\mathrm{R}_1 - \mathrm{R}_2) + j(\zeta_1 - \zeta_2) \right\}. \tag{1.14}$$

Notice that the phase of the interferogram (the interferometric phase) is related to the change in the satellite-target distance. InSAR (Interferometric SAR) is therefore based on this principle and can be used to measure the ground topography or the ground motion as will be shown in subsequent sections.

### 1.2.3 SAR SLC camera model

In this section, we will explain the SAR camera model, used to relate 3D points to their 2D coordinates in the image and vice-versa. The model will be explained for a focused

SLC image. The acquisition geometry of a SAR satellite is shown in Figure 1.2. The coordinate system used is the ECR (Earth Centered Rotational), where the origin is the center of the Earth, the X axis points to the intersection of the equator and the prime meridian, the Z axis points to the north pole, the Y axis can be easily deduced.

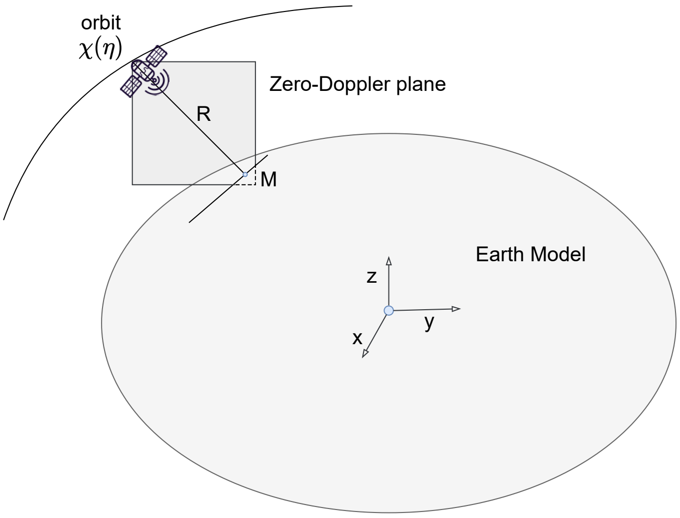

Figure 1.2: Simplified SAR acquisition geometry. The Earth is represented as an inflated ellipsoid on which point M lies. The point M is also in the Zero-Doppler plane at the Zero-Doppler time $\eta$. Point M is also at a distance of R from the satellite at this time.

As mentioned previously, the time of flight of a pulse from the sensor to a specific point target M on the ground will determine the impulse response peak position along the range direction in the SLC data. For simplicity, we will consider that the focusing in azimuth has been done to Zero-Doppler, i.e. the azimuth time of the samples is their Zero-Doppler time. Considering a target with Zero-Doppler Range R, and that the range is the column direction in the SLC image, Equation 1.15 gives us the relationship with the column coordinate col

$$\mathrm{R} = \frac{c}{2}\tau = \frac{c}{2}\left(\tau_0 + \frac{\mathrm{col}}{F_r}\right), \tag{1.15}$$

where $c$ is the speed of light in vacuum, $\tau_0$ is the two-way path delay to the first column of the SLC and $F_r$ is the range sampling frequency.

For the azimuth direction, the line number row is related to the azimuth time $\eta$ by Equation 1.16, where $F_a$ is the azimuth sampling frequency and $\eta_0$ is the time of the first line in the SLC image

$$\eta = \eta_0 + \frac{\mathrm{row}}{F_a}. \tag{1.16}$$

$F_r$, $F_a$, $\eta_0$, and $\tau_0$ are usually given in the metadata of the SLC product.

In order to transform from 3D world coordinates to image space (projection) and vice versa (localization), the Range-Doppler model can be used with the three fundamental equations defined in [Cur82]. Denote $\mathrm{M} = (x_\mathrm{M}, y_\mathrm{M}, z_\mathrm{M})^T$ and $\chi(\eta) = (x_\chi(\eta), y_\chi(\eta), z_\chi(\eta))^T$ the point target and the satellite position in vector representation respectively. The satellite position can be retrieved from the ephemeris as metadata. The ephemeris data consists of equally spaced samples containing the time, position and velocity of the platform before, during, and after the acquisition (called "state vectors" in radar parlance). Therefore, it is common to apply an interpolation technique such that we can query for the position and the higher-order derivatives (speed $\dot{\chi}(\eta)$, acceleration $\ddot{\chi}(\eta)$...) at any moment along the orbit. The distance between M and $\chi(\eta)$ is equal to the range, as shown in the Equation 1.17, known as the SAR range equation

$$E_1 = \mathrm{R}^2 - \|\chi(\eta) - \mathrm{M}\|^2 = 0. \tag{1.17}$$

Then Equation 1.18 states that the point should be in the Zero-Doppler plane:

$$E_2 = \dot{\chi}(\eta).\,(\chi(\eta) - \mathrm{M}) = 0. \tag{1.18}$$

Lastly, the last relation shown in Equation 1.19 states that the point should have an altitude $h$ with respect to the ellipsoid representation of the Earth (depends on the coordinate reference system datum in which $h$ is given, but usually the world geodetic system WGS84 reference ellipsoid)

$$E_3 = \frac{x_{\mathrm{M}}^2 + y_{\mathrm{M}}^2}{(a+h)^2} + \frac{z_{\mathrm{M}}^2}{(b+h)^2} - 1 = 0, \tag{1.19}$$

where $a$ denotes the mean equatorial radius, $b$ is the mean polar radius of the Earth's oblate ellipsoid, and $h$ is the height of point M above the ellipsoid. Therefore, a simple but slightly inaccurate way to encode the height information is to place the point on the inflated ellipsoid that has an equatorial radius of $a + h$ and a polar radius of $b + h$.

When doing a projection, Equation 1.18 is sufficient to solve for $\eta$ [KH08]. The problem amounts to finding the root of $E_2(\eta)$. Therefore, the solution is found in an iterative manner using the Newton-Raphson method, see Algorithm 1.

**Algorithm 1:** Projection $\mathcal{P}(\mathrm{M})$

```
Result: col, row
Input: M : target;   tol : tolerance;   χ(η) : orbit;   c : speed of light;
       τ_0 : range time of the first column;   F_r : range sampling frequency;
       η_0 : azimuth time of the first line;   F_a : azimuth sampling frequency;
$\eta = \eta_0$;
repeat
    $E_2(\eta) = \dot{\chi}(\eta).(\chi(\eta) - \mathrm{M})$;
    $E_2'(\eta) = \ddot{\chi}(\eta).(\chi(\eta) - \mathrm{M}) + (\dot{\chi}(\eta))^2$;
    $d\eta = -\frac{E_2(\eta)}{E_2'(\eta)}$;
    $\eta = \eta + d\eta$;
until $d\eta < tol$;
Use Equation 1.16 to get row;
Use Equation 1.17 to get R;
Use Equation 1.15 to get col;
```

When performing localization, we now want to retrieve the point M from the pixel coordinates (col, row) and a given height $h$. Define

$$E(\mathrm{M}) = (E_1(\mathrm{M}), E_2(\mathrm{M}), E_3(\mathrm{M}))^T = 0. \tag{1.20}$$

We get a system of three unknowns $x_{\mathrm{M}}, y_{\mathrm{M}}, z_{\mathrm{M}}$, and three equations. This system can again be solved iteratively by linearization (first-order Taylor expansion)

$$E(\mathrm{M}) = E(\mathrm{M}_0) + \Delta(\mathrm{M}_0).d\mathrm{M}, \tag{1.21}$$

where

$$\Delta(\mathrm{M}) = \begin{bmatrix} \dfrac{\partial E_1}{\partial \mathrm{M}} \\ \dfrac{\partial E_2}{\partial \mathrm{M}} \\ \dfrac{\partial E_3}{\partial \mathrm{M}} \end{bmatrix} = \begin{bmatrix} & 2(\chi(\eta) - \mathrm{M})^T & \\ & -\dot{\chi}(\eta)^T & \\ \dfrac{2x_\mathrm{M}}{(a+h)^2} & \dfrac{2y_\mathrm{M}}{(a+h)^2} & \dfrac{2z_\mathrm{M}}{(b+h)^2} \end{bmatrix}. \tag{1.22}$$

Since we look for $E(\mathrm{M}) = 0$, we need to solve iteratively for $d\mathrm{M}$

$$-E(\mathrm{M}_0) = \Delta(\mathrm{M}_0).d\mathrm{M}. \tag{1.23}$$

```
Algorithm 2: Localization $\mathcal{L}(\mathrm{row}, \mathrm{col}, h)$
Result: $\mathrm{M} = (x_\mathrm{M}, y_\mathrm{M}, z_\mathrm{M})^T$
Input: (row, col) : SAR image coordinates;   $h$ : height;
       $tol$ : tolerance;   $\chi(\eta)$ : orbit;   $c$ : speed of light;
       $\tau_0$ : range time of the first column;   $F_r$ : range sampling frequency;
       $\eta_0$ : azimuth time of the first line;   $F_a$ : azimuth sampling frequency;
       $\mathrm{M}_{init}$: Initial guess;   ($a$, $b$) : Earth ellipsoid semi-major and semi-minor axis;
$\mathrm{M} = \mathrm{M}_{init}$ ;
Use Equation 1.16 to get $\eta$ from row ;
Use Equation 1.15 to get R from col;
repeat
    Compute $E(\mathrm{M})$;
    Compute $\Delta(\mathrm{M})$;
    Solve $-E(\mathrm{M}) = \Delta(\mathrm{M}).d\mathrm{M}$ to find $d\mathrm{M}$;
    $\mathrm{M} = \mathrm{M} + d\mathrm{M}$
until $dM_x < tol$ , $dM_y < tol$ , $dM_z < tol$;
```

To initialize M in Algorithm 2, we can use the longitude and latitude coordinates of the centroid of the image $(lon_{mid}, lat_{mid})$ since this can be usually inferred from the metadata (rough location of the imaged scene). Then, we convert the point $(lon_{mid}, lat_{mid}, h)$ to the ECR coordinate system to get $\mathrm{M}_{init}$.

The previous equations and algorithms give a first approximation of the geolocation for a SAR image, usually with subpixel accuracy (depending on the ephemeris and timing information accuracy). However, in practice, to achieve the highest precision possible, one needs to consider many effects that occur due to some physical phenomena and data processing details. The effects that need to be considered [GSB+20] are path delays introduced by the Earth's atmosphere (troposphere, ionosphere), the effects of tides (mainly solid Earth tides, ocean loading...), the plate tectonics (given as deformation velocities in the International Terrestrial Reference System ITRF for instance), and various timing effects (bistatic effects, intra-pulse Doppler shift, FM-rate mismatch...). In Chapter 5, we consider some of these effects in our study, such as the tropospheric delay, the intra-pulse effect in range, and the bistatic effect in azimuth.

The tropospheric delay comes from the fact that the EM wave's velocity is actually lower than the speed of light in vacuum. Even though precise methods relying on advanced modeling of the atmospheric state exist [HIKK08, JGL+11, YLPC18, CBGE18] a simple model can also give a good approximation of this effect [JPS+08]:

$$\delta \mathrm{R} = \frac{1}{\cos \alpha_{\mathrm{inc}}} \left( \frac{h^2}{8.55 \cdot 10^7} - \frac{h}{3411} + 2.41 \right) \quad [\mathrm{m}], \tag{1.24}$$

where $\delta$R is range offset, which would induce the atmospheric lag in vacuum, h is the height, and $\alpha_{inc}$ is the incidence angle.

As for the bistatic offset observed in azimuth, it can be explained when looking at the send-receive system of the satellite. This correction takes into account the fact that the satellite does not stop at a fixed position in orbit in order to wait for the pulse to reflect on the ground until reception (stop-and-go approximation). The satellite will actually keep moving and transmitting pulses each Pulse Repetition Interval (PRI). Within a PRI, after each transmission window, there is a reception window. A pulse transmitted in the $i^{th}$ PRI is received in the (i + rank)$^{th}$ PRI receive window. The 1D echo packets then need to be reorganized as a 2D image, by associating to each echo an azimuth time, which is ideally in the middle between transmission and reception. When this is not already considered when constructing the SAR image, which is the case of Sentinel-1, an azimuth shift which is linear with range will be present in the data [GSB+20].

The intra-pulse effect in Sentinel-1 comes from the fact that the Doppler frequency of a target varies along the azimuth even within a burst, whereas the burst-level processor assumes a single frequency for the duration of the burst. As a result, a range bias will be introduced for a given target that depends on its azimuth offset from the burst center. For IW products, this effect may cause range errors that reach the order of 0.5 m at the burst upper and lower limits.

The timing correction effects need to be computed on the level of a Sentinel-1 burst. Furthermore, for some of them, the 3D geometry with the sensor is also needed, like the topographic-induced shift in azimuth due to Doppler FM-rate mismatch [GSB+20]. Therefore, the computation of some of the shifts is only relevant in the context of the geolocation of a Sentinel-1 burst. Also, the extended timing annotation dataset (ETAD) product recently developed for Sentinel-1 provides the most important timing corrections per burst. It was shown that using those timing corrections improves the processing flows established SAR applications such as absolute ranging of targets, offset tracking, and interferometry [GLM+22, SGB+23].

As can be seen in this section, the physical sensor model for the SAR data requires a good amount of knowledge of the acquisition process. This is why it would be interesting to replace this complex model with a simpler one, for instance, the Rational Polynomial Coefficients (RPC) camera model. Some space agencies have started to adopt this approach, as seen in the Chinese satellite Gaofen 3 [WZY+17]. Another reason to use the rational functional model is for its computational efficiency. Applying a geolocation function amounts to evaluating the value of polynomials, whereas Algorithms 1 and 2 are more costly since they use an iterative optimization procedure. In Chapter 4, we show that we can fit precise RPC models from the Sentinel-1 physical model.

### 1.2.4 Coregistration

In this section, we will examine some of the different methods that can be used to align SAR images. Coregistration is usually a necessary pre-processing step for any time series analysis and refers to the process of resampling a secondary image onto the reference system of a primary image such that the same ground features would be located at the same pixel position in both images. The first technique is the geometric method, which relies on the projection of a set of 3D points sampled from a Digital Elevation Model into the primary image and the secondary image. The projection is performed via the camera model detailed in Section 1.2.3, which can be either physical or provided as RPC functions. The set of 2D correspondences obtained can be used to fit a warp function. In [SBM+06], a bias term in the warp function is estimated from tie points, because of potential errors in the projection function. In other words, the alignment estimated with the geometric method is often refined using the estimates from the SAR data. Among the different methods that can perform this fine estimation, we distinguish between correlation and spectral diversity (or split-band interferometry). For distributed Gaussian scatterers, it was shown [BE05] that coherent cross-correlation using the complex samples reaches the best attainable precision (the Cramér-Rao bound), but special care must be taken in the removal of systematic non-noise phase differences. It is also possible to perform incoherent cross-correlation (also known as speckle tracking) on the amplitude or the intensity (square of the amplitude), even though these estimates are theoretically less accurate than their coherent counterpart [De 14]. As for the spectral diversity method, it relies on the concept of splitting the image into lower and upper frequency-range band-pass filtered sub-apertures. Then lower and upper-range interferograms are formed, and a final differential interferogram is generated, where the phase is proportional to the residual shift, with a sensitivity related to the spectral separation between the central frequencies of the sub-apertures [SM00]. The principle behind this method is to artificially generate SAR sub-aperture images that are not in baseband so that the impulse response in the focused data contains a phase term linear with the pixel dimension (either range or azimuth), as seen in Equation 1.9. This method has an accuracy that is very close to the Cramér Rao bound [BE05].

Furthermore, the *Enhanced Spectral Diversity* (ESD) technique [PISM+12] was proposed for the TOPS mode of TerraSAR-X, mainly for interferometry. Indeed, as mentioned in Section 1.2.1, for the TOPS mode, because of the rotation of the EM beam during the burst acquisition, the Doppler centroid frequency increases linearly with the azimuth time and reaches high values at the burst edges. An azimuth misregistration will induce non-negligible azimuth phase ramps in the burst interferograms. The required accuracy to keep the error less than 3.6° (1 / 100 cycle) is around $8 \times 10^{-4}$ pixels and can be reached with the ESD technique. ESD uses the burst overlap regions analogously to the sub-apertures in the spectral diversity technique. The overlap regions are images representing the same ground features, but characterized by very high Doppler centroid frequencies with opposite signs. Thus, to apply the spectral diversity technique, it is not necessary to synthesize sub-apertures in azimuth and the overlaps can directly be used instead. Because of the big spectral separation of the overlap's central frequencies, the azimuth registration accuracy that can be reached with this technique is the highest possible among the different methods and is usually sufficient to avoid azimuth phase ramps. ESD can also be used to retrieve the deformation in the along-track direction at the overlaps [GKMV16, YMPIPJ19]. Some improvements have been made through the years to the ESD technique, such as the inversion of pairwise shifts in a time series setting as seen in [YMDPI17] or in the Network-based ESD method (NESD) [FAS17].

Looking specifically at the co-registration of Sentinel-1, many pipelines and variations exist [WWS+16, Gra15, YMPIG+16, HNBM16, FAS17, MDZ+19, LSG+20], but the general idea is mostly the same. First, a geometric registration is performed using precise satellite orbits and a DEM. Then, refinement can be done with a cross-correlation technique for instance, but this step is sometimes skipped or only applied in range. Lastly, the ESD technique is used to attain the maximal accuracy in azimuth if the desired application is interferometry. Also, coregistration is sometimes performed on individual bursts, which are later stitched together, or on a mosaic of the bursts. In Chapter 5, we perform a geometric registration per burst and then stitch the bursts together to get a precise mosaic.

### 1.2.5 Differential Interferometry - DInSAR

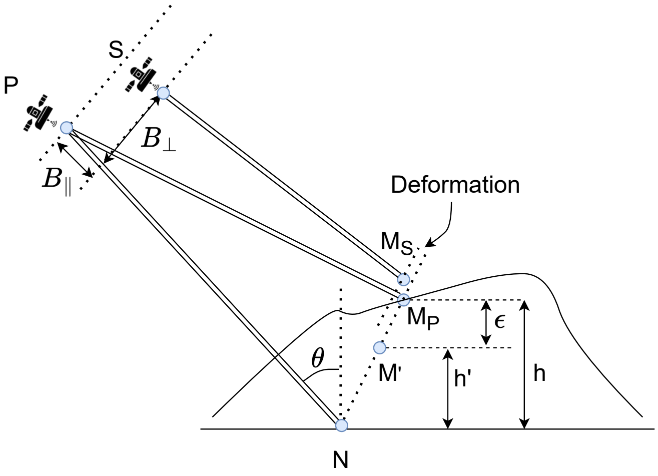

Figure 1.3: Differential Interferometry (DInSAR) principle. The scene is acquired from a satellite at two positions P (Primary) and S (Secondary), corresponding to two passes at different dates along the same orbit. Between the two dates, the target moved from position $\mathrm{M_P}$ to position $\mathrm{M_S}$. The scale of the figure is inaccurate for visualization purposes: the deformation (millimetric) is actually many orders of magnitude smaller than the satellite-target distance (hundreds of kilometers) and the topography (meters, depending on the terrain). The figure shows as well point N, which would have been acquired in the same range sampling cell in the absence of topography on the reference surface. Also, point $\mathrm{M}'$ is the location of point M given by an external data source, such as DEM. The assumed height $h'$ of $\mathrm{M}'$ has an error w.r.t. the true height $h$ of $\epsilon$. The geometric baselines $B_\perp$ and $B_\parallel$ and the incidence angle $\theta$ are also represented.

Most interferometric SAR satellites can acquire the same scene from a similar viewing geometry after a few days. This ability to make repeat pass acquisitions enables the measurement of the ground deformation throughout time with the Differential Interferometry principle (DInSAR), illustrated in Figure 1.3. The satellite is at the primary position (P) for one date and at the secondary position (S) for another. Their spatial separation $B = \|\mathrm{PS}\|$ is called the geometric baseline and can reach values up to a couple of hundred meters for Sentinel-1 [PINYM+17]. Suppose point M undergoes a small deformation (order of millimeters) between the two dates. By Looking at Equation 1.14, the interferometric phase can be written as:

$$\Phi_{12} = -\frac{4\pi}{\lambda}(\|\mathrm{PM_P}\| - \|\mathrm{SM_S}\|) + \zeta_1(\mathrm{M_P}) - \zeta_2(\mathrm{M_S}). \tag{1.25}$$

We suppose that the scattering phases are equal for the two dates and cancel each other.

We can also rewrite Equation 1.25 as

$$\Phi_{12} = O_{12} + \Xi_{12} + \mu_{12}\,, \tag{1.26}$$

where

$$O_{12} = -\frac{4\pi}{\lambda}(\|\mathrm{PN}\| - \|\mathrm{SN}\|)\,, \tag{1.27}$$

is the orbital phase and

$$\Xi_{12} = -\frac{4\pi}{\lambda}\left\{(\|\mathrm{PM_P}\| - \|\mathrm{SM_P}\|) - (\|\mathrm{PN}\| - \|\mathrm{SN}\|)\right\}\,, \tag{1.28}$$

is the topographic phase and

$$\mu_{12} = -\frac{4\pi}{\lambda}(\|\mathrm{SM_P}\| - \|\mathrm{SM_S}\|) = -\frac{4\pi}{\lambda}\mathrm{D}_{12}, \tag{1.29}$$

is the deformation phase, with $\mathrm{D}_{12} = (\|\mathrm{SM_P}\| - \|\mathrm{SM_S}\|)$ defined as the deformation between the two dates (with this convention, a positive deformation corresponds to a movement towards the satellite). The orbital and topographic phase components can be approximated [Han02] with

$$O_{12} = -\frac{4\pi}{\lambda}B_{\|,12}, \tag{1.30}$$

$$\Xi_{12} = -\frac{4\pi}{\lambda}\frac{B_{\perp,12}}{\mathrm{R}\sin\theta}h. \tag{1.31}$$

Since the goal is to measure the deformation, the orbital and topographic phases are simulated for each pixel in the interferogram using the camera model (for ex. Algorithms 1 and 2) and a Digital Elevation Model (DEM). For instance, one way to perform the simulation is described as follows. For a set of points (N) on the ellipsoid, it's possible to determine the satellite positions of the closest approach (P or S from $\chi(\eta)$) and the range R using Algorithm 1, and therefore compute the baselines ($B_{\perp,12}$, $B_{\|,12}$) and incidence angles ($\theta$) for these points; Since Algorithm 1 also gives us the coordinates in the SAR image, the baselines and incidence angles can be interpolated for all the pixels in the primary image. At this stage, a simulation of the orbital phase $O_{12}^{sim}$ can already be computed with Equation 1.30. If a DEM is also available, giving us the 3D location of a set of points $\mathrm{M}'$ in the scene, Algorithm 1 can also be applied to deduce the coordinates of each 3D point in the primary image, and the height $h'$ can then be interpolated for all the pixels (backgeocoding [LCRCPIP21]). Then Equation 1.31 can be used to compute the simulated topographic phase $\Xi_{12}^{sim}$. Lastly, the differential interferometric phase is obtained with

$$\phi_{12} = \angle\left\{\Gamma_{12}\cdot e^{-jO_{12}^{sim}}e^{-j\Xi_{12}^{sim}}\right\}, \tag{1.32}$$

where $\angle$ gives the phase in the $[-\pi,\pi)$ interval. In practice, the simulated phases are not perfect mainly due to inaccuracies in the orbits and DEM. After the compensation, a residual orbital phase $o_{12}$ and a residual topographic phase $\xi_{12}$ remain. $\xi_{12}$ can also be linked to the DEM residual topographic error (RTE $\epsilon = h - h'$), by replacing $\Xi_{12}$ and $h$ with $\xi_{12}$ and $\epsilon$ in Equation 1.31 respectively: $\xi_{12} = -\frac{4\pi}{\lambda}\frac{B_{\perp,12}}{\mathrm{R}\sin\theta}\epsilon$. Furthermore, one needs to take into account the wave propagation delays through the atmosphere $\alpha_{12}$, noise expressed as $n_{12}$, and the phase ambiguity expressed $2\pi k_{12}$ since the phase can only be observed in the $[-\pi,\pi)$ interval. Hence, the DInSAR equation can be now written as:

$$\begin{aligned}\phi_{12} &= \mu_{12} + \xi_{12} + o_{12} + \alpha_{12} + n_{12} + 2\pi k_{12}\\ &= -\frac{4\pi}{\lambda}\mathrm{D}_{12} - \frac{4\pi}{\lambda}\frac{B_{\perp,12}}{\mathrm{R}\sin\theta}\epsilon + o_{12} + \alpha_{12} + n_{12} + 2\pi k_{12}.\end{aligned} \tag{1.33}$$

The phase in Equation 1.33 is not only related to deformation but also contains many other contributions. To overcome this limitation, first of all, the atmospheric phase $\alpha_{12}$ can be mitigated using simulations of the EM wave delays through the troposphere with Numerical Weather Models [HIKK08, JGL$^+$11, YLPC18, CBGE18] or by modeling their linear dependence to topography [CAT$^+$07, CDLB07, LQDT$^+$09, Zeb21]. The noise $n_{12}$ can be reduced through denoising, for which a review can be found at [XGLX20]. Often related to denoising is the coherence, i.e. the magnitude of the normalized complex cross-correlation. Indeed, phase denoising and coherence computation both fall under the umbrella of interferometric parameter estimation [VTCB04, DDT11, DDT$^+$15, SGRB21]. The coherence can be useful for subsequent processing such as phase unwrapping, which is the process of solving the $2\pi k_{12}$ ambiguity [GZW88, PS94, PJJ94, TNM98, Cos98, GP98, CZ01, YLY$^+$19]. Lastly, one way to mitigate the orbital phase $o_{12}$ is to model it as a fitted polynomial with respect to the image coordinates in azimuth and range [DFL$^+$21, LQDT$^+$09]. All mitigation methods are also not perfect, and DInSAR is therefore mostly suited to use cases where the deformation signal is high enough to dominate over all the other contributions, such as when dealing with earthquakes. On a final note, looking at the deformation phase $\mu_{12}$ from Equation 1.29, we notice that:

- The deformation is measured in the Line Of Sight (LOS) to the satellite, i.e. in the direction defined by the line joining the satellite to the target.
- The sensitivity to the deformation is really high. Indeed, a deformation of $\frac{\lambda}{2}$ will induce a cycle ($2\pi$ radians). For ex., for Sentinel-1 operating in the C-band, $\frac{\lambda}{2} \approx 2.8$ cm.

Therefore, the DInSAR technique allows measuring the deformation in the LOS with cm precision. It is applicable when the phase gradient between neighboring points is less than $\pi$ in absolute value (related to phase unwrapping Itoh condition [GP98]). This translates to having small deformation gradients, i.e. the relative deformation between neighboring points in absolute value should be less than $\frac{\lambda}{4}$, which is $\approx 1.4$ cm for Sentinel-1. In Chapters 6 and 7, we explore the performance of some deep learning networks on DInSAR tasks, namely phase denoising and coherence estimation, as well as phase unwrapping.

### 1.2.6 Advanced-DInSAR

The Advanced-DInSAR (A-DInSAR, or time series radar interferometry, multitemporal InSAR...) methods work not only on a couple of SAR images (yielding a single interferogram) but on a stack of $\mathrm{L}+1$ SAR images. Therefore, there are L independent DInSAR interferograms that can be formed w.r.t. a single image (for ex. the middle one in the time series), or $\frac{(\mathrm{L}+1)\mathrm{L}}{2}$ maximal amount of redundant interferograms. Using this temporal information, we could solve Equation 1.33 more easily to get the deformation (time series of deformation $\mathrm{D}_{1u}$ for $u = \{2 \dots \mathrm{L}+1\}$). Indeed, the deformation is usually modeled as having a smooth evolution throughout time, where linear, polynomial or seasonal models are sometimes adopted [FPC23]. Also, the orthogonal baseline will vary for each pair of images in the stack, making it possible to fit the residual topographic height $\epsilon$. As for the phase unwrapping, it must take into account the temporal dimension, either by combining a 2D spatial unwrapping with a 1D temporal unwrapping (or consistency check) [DCM$^+$14, BPPJL20, LQDT$^+$09] or adopting a full 3D unwrapping approach [HZ07, CMM12, PL06]. Lastly, the atmospheric phase is assumed to have low variations in space and high variations in time and can thus be filtered out from the unwrapped phases [FPR00]. These are some of the elements used to perform the deformation estimation, but many methods were developed throughout the years from which we distinguish three classes:

- PS: A family of methods that detect and restrict the estimation on strong, stable reflectors in the image with low noise level through the time series called *Persistent Scatterers* [FPR00, FPR01].
- SBAS (or DS): A family of methods that work on *Distributed Scatterers*, i.e. targets that do not have a stable response on their own but exhibit a coherent phase when aggregated with neighboring targets with similar characteristics [BFLS02, LMM+04].
- Hybrid methods PS + DS: Jointly process PS and DS, like in [FFN+11, ADB18, MN22].

Please refer to [MHR20, CMCG+16] for a more exhaustive overview. These methods have made great advances in the development of automated processing chains to retrieve the deformation time series. The PS and SBAS methods are complementary and detect deformation phenomena on different scales. Since the PS method works on the scale of individual scatterers, it is more interesting for localized measurements. However, some of the assumptions made in a generic PS processor can still be too severe, especially on pixels exhibiting nonlinear or even fast discontinuous deformation. For instance, the linear motion assumption is sometimes used to detect PS pixels, and can overlook some pixels exhibiting non-linear behavior [YDLQ+12, CSM+20]. Furthermore, even if the pixel is detected, some temporal filtering to remove the atmospheric components can also oversmooth the retrieved deformation time series. Therefore, when performing our localized measurements in Chapter 8, we don't apply a generic PS processing scheme to avoid losing any information but only use some concepts from the PS technique.

## 1.3 Short outline of the thesis

This thesis is divided into three parts. The first part, comprising Chapters 3 to 5, contains our contributions to the SAR processing pipeline. In particular, we first study different approaches related to deramping, i.e. removing the Doppler centroid phase ramp introduced in Section 1.2.1, a crucial step for Sentinel-1 burst resampling. Then we show the possibility of replacing Sentinel-1's SAR physical sensor model with an RPC camera model. To conclude the first part, we introduce a method to obtain a time series of geometrically precise coregistered Sentinel-1 burst mosaics. In the second part, comprising Chapters 6 to 7, we briefly evaluate some deep learning networks applied to InSAR tasks such as phase denoising, coherence estimation, and phase unwrapping. Lastly, the third part containing Chapter 8 applies DInSAR on crude oil storage tanks and shows the potential of the technique in measuring the crude oil volume.

**Chapter 3: Comparison of Sentinel-1 TOPS deramping techniques**
This chapter compares the different spectral centering methods (referred to as deramping) for the Sentinel-1 images acquired with the TOPSAR mode, in the context of interferometry. The spectral shift (the Doppler centroid frequency) increases linearly with the burst azimuth time due to the uniform EM beam rotation. It is, therefore, necessary to center the frequencies in the Fourier domain around 0 Hz prior to image interpolation. We show the analogy between two approaches in the literature, the conventional deramping function prescribed by ESA and the one implemented in the NSBAS software. We show that the NSBAS deramping function might induce a small quadratic phase ramp error in the interferometric phase along the azimuth. We propose a deramping method that does

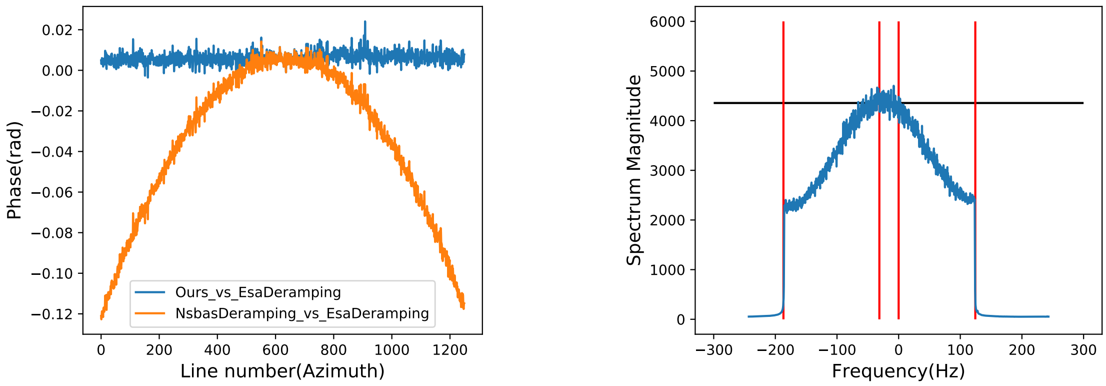

(a) The InSAR phase difference profile

(b) The spectral shift of "Ours"

Figure 1.4: Deramping experiments in Chapter 3. On the left, we show that "NsbasDeramping" introduces a quadratic phase along the azimuth, which is not present in "Ours". On the right, both methods feature a spectral shift prior to resampling

not suffer from this imprecision. The method is analogous to applying the primary image deramping function for all the time series, similarly to what was proposed in [HNBM16]. We validate with experiments on real Sentinel-1 data that the error that reaches 0.12 rad on the burst boundaries with the NSBAS deramping is not present in our method as can be seen in Figure 1.4. However, both the proposed and the NSBAS deramping methods only approximately re-center the spectrum, meaning that a small residual spectral shift remains. We derive a closed-form expression for the expected residual shift and show that the residual shift is typically small on a Sentinel-1 dataset (less than 35 Hz). We also verify that interpolating the images containing this residual spectral shift should not induce considerable drops in interferometric coherence. The proposed deramping method is only advantageous when co-registering a time series of N secondary SAR images onto a primary image. In this case, N + 1 deramping operations are needed with the proposed method, in contrast with the 2 * N de/re-ramping operations with the conventional approach.

### Chapter 4: Robust RPC camera Modelling

This chapter describes a terrain-independent algorithm to accurately derive a Rational Polynomial Coefficients (RPC) model from a set of 3D-2D point correspondences based on a regularized least squares fit. The RPC camera model can be used to describe a variety of image acquisition systems in remote sensing, notably optical and Synthetic Aperture Radar (SAR) sensors. RPC functions relate 3D to 2D coordinates and vice versa, regardless of physical sensor specificities, which has made them an essential tool to harness satellite images in a generic way. The described fitting algorithm automatically sets the regularization parameter using an L-curve heuristic and is also iteratively weighted, i.e. the solution of an iteration is used to set the weight for the next iteration. The precision of the fitted RPC is assessed by varying the number of point correspondences and the size of the area that they cover. We test the algorithm on Sentinel-1 SAR and WorldView-3 optical data, to derive RPCs from physical sensor models or from other RPC models after composition with corrective functions. The results for Sentinel-1 can be seen in Figure 1.5. We show that increasing the number of correspondences slightly reduces the RMSE. We also show that it is easier to fit the RPC function on a smaller surface area. For most configurations, the RPC fitted has errors on the order of $10^{-4}$ pixels in terms of RMSE on a validation grid of points, confirming the ability of the model to capture complex

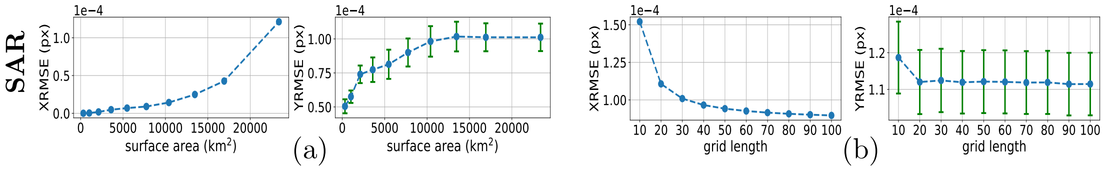

(a) (b)

Figure 1.5: RPC reprojection error varying grid length and surface area on the Sentinel-1 SAR dataset in Chapter 4. Each vertical bar corresponds to the $[-\sigma/2, \mu, \sigma/2]$ values of the root-mean-square error (RMSE) evaluated across the different images of the dataset, in each dimension of the image plane, where $\mu$ corresponds to the mean and $\sigma$ to the standard deviation.

geolocation mappings.

**Chapter 5: Sentinel-1 IW geolocation based burst stitching**
This chapter proposes a method to construct a precise Sentinel-1 burst mosaic. Indeed, since the commissioning phase of Sentinel-1A, several calibration studies have improved the geolocation and geometric modeling of the data as seen in Section 1.2.3. The implementation of the corrections presented in these studies is left to the user, and the topic is gaining more attention with the anticipated release of the Extended Timing Annotation Dataset (ETAD). The corrections might be confusing when working with bursts in the interferometric wide swath mode because the geometric shifts in the data are not usually the same at the burst boundaries. This might introduce small inconsistencies in a mosaic product if not properly handled, which is especially inconvenient in high-precision applications. We propose a method to account for the precise geolocation and timing corrections by resampling each Sentinel-1 burst before stitching into the mosaic. The method is based on a geolocation of a set of 3D points sampled from a Digital Elevation Model. This enables the method to support the computation of corrective shifts which not only rely on the image coordinates but also on their corresponding 3D geographic coordinates. The corrections are used in the fitting of an affine resampling matrix per burst. This procedure can be applied on a primary Sentinel-1 mosaic for a single date. It can also be used on secondary acquisitions to get a coregistered time series of geometrically precise Sentinel-1 mosaics. The method is validated with experiments on real Sentinel-1 data, where we show an improvement in the alignment of the burst overlaps. Indeed, the method successfully corrects intra-pulse shifts in the order of 0.5 meters in range between consecutive bursts as shown in Table 1.1.

| | Before correction | After correction |
|---|---|---|
| az shift (m) | 0.086 ± 0.35 | 0.15 ± 0.334 |
| rg shift (m) | -0.57 ± 0.16 | -0.021 ± 0.15 |

Table 1.1: Measured registration shift shown in Chapter 5 between the overlaps of bursts "i" and "i+1". The measurement was performed on 31 S1 images on the first swath and on the 8 overlaps. Each measurement is shown with and without the application of the proposed resampling method. The table shows the average value and the standard deviation in meters. Notice the improvement in alignment in the range direction, where a bias of half a meter was successfully compensated.

**Chapter 6: Phase denoising and coherence estimation network**
This chapter examines the joint denoising and coherence estimation performance of the

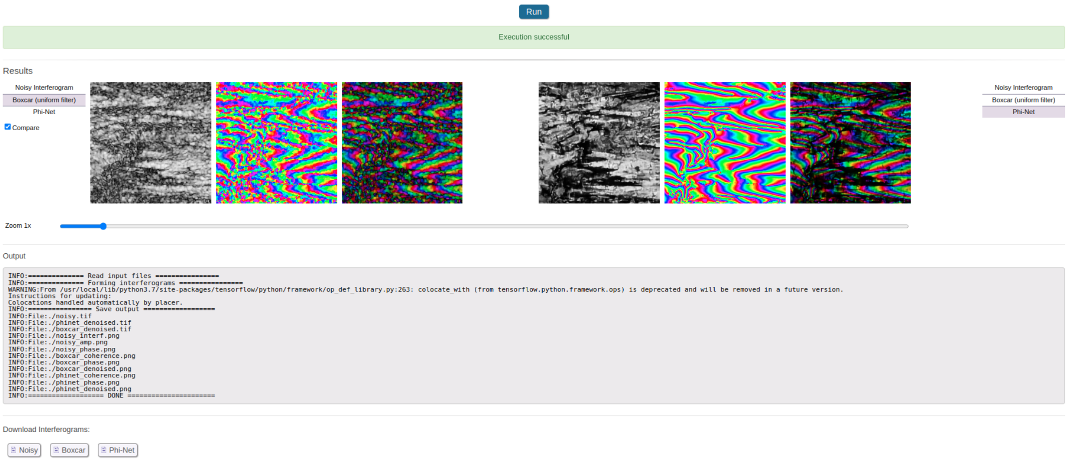

```
INFO:============== Read input files ================
INFO:============== Forming interferograms ================
WARNING:From /usr/local/lib/python3.7/site-packages/tensorflow/python/framework/op_def_library.py:263: colocate_with (from tensorflow.python.framework.ops) is deprecated and will be removed in a future version.
Instructions for updating:
Colocations handled automatically by placer.
INFO:================ Save output ==================
INFO:File:./noisy.tif
INFO:File:./phinet_denoised.tif
INFO:File:./boxcar_denoised.tif
INFO:File:./noisy_interf.png
INFO:File:./noisy_amp.png
INFO:File:./noisy_phase.png
INFO:File:./boxcar_coherence.png
INFO:File:./boxcar_phase.png
INFO:File:./boxcar_denoised.png
INFO:File:./phinet_coherence.png
INFO:File:./phinet_phase.png
INFO:File:./phinet_denoised.png
INFO:=================== DONE ======================
```

Figure 1.6: The demo developed on the Φ-Net network and used for the experiments in Chapter 6. We can see the coherence, denoised phase, and complex image representation for the boxcar filter (on the left) and the Φ-Net network (on the right).

network known as Φ-Net (Sica et al. 2021). We briefly inspect the method, network architecture, training data, and strategy. Then, in the experimental section, we compare the network's performance against the simple boxcar uniform filter on real Sentinel-1 interferograms containing topographic fringes and provide an online demo to reproduce the experiments as shown in Figure 1.6. We verify the observations made by the authors, in particular concerning the superior denoising performance and preservation of fine details in the coherence estimation. Furthermore, we notice a link between the boxcar filter and Φ-Net when comparing their results, especially in areas heavily impacted by noise. We assume that this is naturally explainable by interpreting Φ-Net as a network that acts on the residual of a strided boxcar filter. Lastly, we notice some discontinuities in the Φ-Net fringes. Hence, it is likely that an end-to-end deep learning method might bring a small improvement to the patch-based approach by increasing the receptive field.

### Chapter 7: Phase unwrapping network

This chapter aims to explain and evaluate the phase unwrapping method proposed by

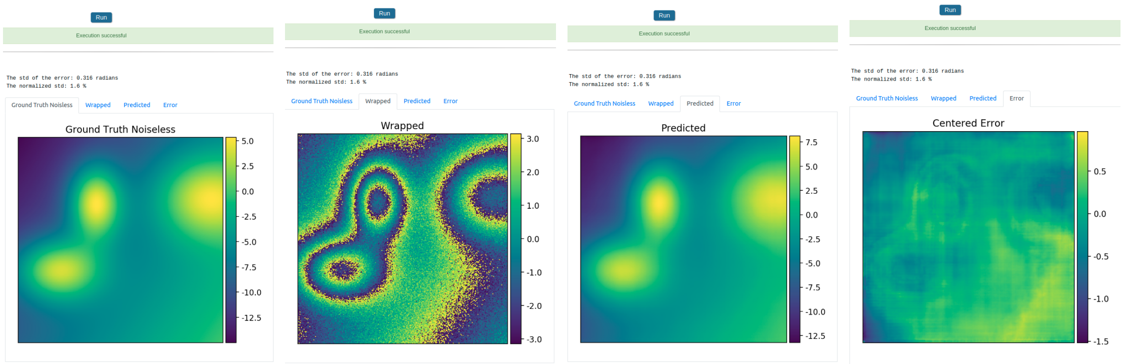

```
The std of the error: 0.316 radians
The normalized std: 1.6 %
```

The std of the error: 0.316 radians
The normalized std: 1.6 %

The std of the error: 0.316 radians
The normalized std: 1.6 %

The std of the error: 0.316 radians
The normalized std: 1.6 %

Figure 1.7: The output of the demo of the phase unwrapping network examined in Chapter 7. The metrics are displayed on top of a tabset. Four tabs are available for the ground truth, wrapped noisy phase, predicted unwrapped image with the network, and error image.

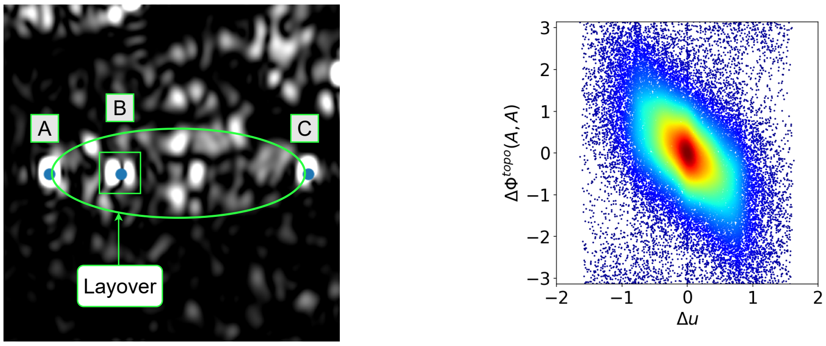

Figure 1.8: Results of Chapter 8. On the left, we see a zoomed image of a storage tank, with the three bright corners seen in Sentinel-1: the fixed roof (A), the fixed base (B), and the floating roof (C). Because of the layover effect, InSAR measurements on (B) are noisier than on (A). On the right, the scatterplot shows a trend relating the double difference of the phase on the neighboring tank roofs (A) with the double difference of the tanks' fill ratio.

Perera et al. in [A joint convolutional and spatial quad-directional LSTM network for phase unwrapping, ICASSP 2021]. The method is based on deep learning and has been recently proposed to tackle the phase unwrapping problem. We provide an online demo to simulate phase images and run them through the network. The network performance can be tested visually and through metrics such as the error standard deviation, as can be seen in Figure 1.7. The simulation can provide some out-of-distribution data, especially with the added atmospheric signal specific to the InSAR phase. We observe from our experiments that the network performance is adequate on in-domain data, with some deterioration on out-of-domain data. The resulting error is structured and might contain stripes, textures, and under-estimated peaks. Lastly, we address the fact that the network mutually performs the tasks of phase denoising and unwrapping. We propose to separate the two tasks and restrict the network responsibility on phase unwrapping, which would simplify the evaluation procedure.

**Chapter 8: InSAR on crude oil storage tanks**
This chapter examines the possibility of using the interferometric phase on some fixed corners of storage tanks to infer the tank fill ratio. For the study, we use Sentinel-1 data on a site of floating roof tanks for which the fill ratio can be inferred from the floating roof position. We observe a correlation between the phase double difference taken at the fixed roof of neighboring tanks and the fill ratio double difference as can be seen in Figure 1.8. The trend suggests that when a tank fills up, the fixed roof corner undergoes a deformation of around 1 cm away from the satellite. We highlight the presence of uncompensated topographic effects and slow temporal trends. We also show the relationship between the noise level in the scatterplots and the amplitude dispersion of the reflectors. We also interpret the poor scatterplots obtained at the fixed base reflector as a result of the layover effect from the floating roof. The previously listed challenges require further investigation and the development of adapted InSAR techniques.

## 1.4 Summary of contributions

This thesis revisits the Sentinel-1 InSAR pipeline, with the objective of clarifying some concepts and improving the precision of others. This work has also contributed to the development of an InSAR processing chain at Kayrros implemented in a Python package called EOS-SAR.

The first part of the thesis offers different contributions leading to the construction of precise Sentinel-1 mosaics. In Chapter 3, we study the deramping of Sentinel-1 bursts, a necessary step before resampling. We compare the conventional deramping prescribed by ESA with the one implemented in the NSBAS software and show the analogy between them. This leads us to propose a deramping approach that achieves a tradeoff between precision and computation (measured in the number of de/re-ramping operations). Then, in Chapter 4, we provide an open-source implementation of an RPC camera model fitting method using an iterative regularized weighted least-squares optimization algorithm. We validate that the fitted RPCs from Sentinel-1's physical sensor model have errors on the order of $10^{-4}$ pixels in terms of RMSE. Lastly, in Chapter 5, we introduce a method to obtain a time series of geometrically precise Sentinel-1 burst mosaics. The resampling matrices are estimated per burst from the geolocation of 3D points sampled from a DEM, while taking into account precise corrective shifts. These shifts are detailed in the literature of Sentinel-1 geolocation precision studies and may induce some small geometric inconsistencies at the burst boundaries if not properly handled during stitching.

The next part of the thesis contains a secondary contribution, which is a brief evaluation of deep learning applications to InSAR. In this part, we mainly provide evaluation studies and online demos for the user to try, and we do not re-train or construct the models ourselves. Our main conclusion is that the networks have promising performances for tasks such as phase denoising, coherence estimation, and phase unwrapping. In Chapter 6, we validate the Φ-Net network's satisfying denoising and coherence estimation performance and establish an analogy with the boxcar filter. We also suggest replacing the patch decomposition in this method with an end-to-end deep-learning approach which might improve large-scale fringe estimation. For phase unwrapping in Chapter 7, we suggest separating the unwrapping and denoising tasks instead of training the network to do both.

The final part of the thesis in Chapter 8 shows the potential of InSAR for the measurement of the crude oil volume from the deformation of storage tanks. Besides the novelty of this application, it also provides a small contribution to localized interferometry. Indeed, with only the use of a simple phase double difference between neighboring reflectors, we show the possibility of extracting some meaningful information from Sentinel-1 interferograms on specific assets.

It is beneficial at this point to summarize how each contribution is being used or can be used in a processing chain. First, in EOS-SAR, we chose to implement the standard ESA deramping method. Indeed, in a full interferometric pipeline, the gain in speed that we get by skipping a few deramping operations might not justify the risk of inducing processing errors. Nonetheless, our comparative study in Chapter 3 was key in understanding the subtleties of deramping and making the choice depending on the listed tradeoffs.

Then, for fitting RPC functions, we distribute rpcfit as an open-source package that provides fitted coefficients from point grid inputs using the algorithm explained in Chapter 4. We intend to validate the potential gain in efficiency that we could get by using RPCs for operations such as backgeocoding (transforming quantities from geographic to radar coordinates using a DEM) or geocoding (the inverse operation, also known as orthorectification) or geometric co-registration as in Chapter 5. These operations are key to combining data sources acquired by different sensors with SAR (optical images, weather data, GPS data...). Using RPCs is a simple alternative to camera models and should be more efficient computationally. We encourage more SAR image vendors to include RPCs in their metadata in the future. In addition, this tool was used by other members of the team for adjusting camera models in optical imagery in [MdFML+21, MEA+22].

As for the precise burst resampling and stitching methodology for the geometric coregistration of Sentinel-1 shown in Chapter 5, it has been integrated into the EOS-SAR package where it is applied systematically. This topic of using fine corrections to achieve precise coregistration on a common grid is gaining traction with the upcoming release of the ETAD product [GLM+22]. Also, the upcoming OPERA coregistered SLC product [FBJ+23] should also use ETAD-like corrections to perform the fine alignment.

For the Deep Learning networks shown in Chapters 6 and 7, we have seen that their results are encouraging, but do not use them systematically for now, even though they are well adapted to methods such as SBAS briefly mentioned in Section 1.2.6. For denoising and coherence estimation, deep learning seems well suited to solve this problem, and Φ-Net results are already interesting to generate and/or improve downstream tasks. As for the unwrapping network, because this operation is risky and might induce large errors, we cannot recommend using the network for precise applications. We hope for the future to see more InSAR problems solved using machine learning.

Lastly, for the application of crude oil storage tanks, we show that using the double-phase difference could highlight the challenging atypical deformation phenomenon. We intend to continue to explore more sites and develop an adapted processing scheme.

## 1.5 List of publications

**Presented in this thesis**

- Roland Akiki, Raphaël Grandin, Carlo de Franchis, Gabriele Facciolo, and Jean Michel Morel. A Comparative Study of Deramping Techniques for Sentinel-1 Tops in the Context of Interferometry. In *International Geoscience and Remote Sensing Symposium (IGARSS)*, pages 3372–3375. IEEE, 2021
- Roland Akiki, Roger Marí, Carlo de Franchis, Jean Michel Morel, and Gabriele Facciolo. Robust Rational Polynomial Camera Modelling for Sar and Pushbroom Imaging. In *International Geoscience and Remote Sensing Symposium (IGARSS)*, pages 7908–7911. IEEE, 2021
- Roland Akiki, Jeremy Anger, Carlo De Franchis, Gabriele Facciolo, Jean Michel Morel, and Raphael Grandin. Improved Sentinel-1 IW Burst Stitching Through Geolocation Error Correction Considerations. In *International Geoscience and Remote Sensing Symposium (IGARSS)*, pages 3404–3407. IEEE, 2022
- Roland Akiki, Jérémy Anger, Carlo de Franchis, Gabriele Facciolo, Jean-Michel Morel, and Raphaël Grandin. A brief evaluation of InSAR phase denoising and coherence estimation with Φ -Net. *Image Processing On Line*, submitted paper
- Roland Akiki, Carlo de Franchis, Gabriele Facciolo, Jean-Michel Morel, and Raphaël Grandin. Phase Unwrapping using a Joint CNN and SQD-LSTM Network. *Image Processing On Line*, 12:378–388, oct 2022
- Roland Akiki, Carlo de Franchis, Gabriele Facciolo, Raphaël Grandin, and Jean-

Michel Morel. On The Potential Of Insar For Estimating Crude Oil Volume Changes From The Deformation Of Storage Tanks. In *International Geoscience and Remote Sensing Symposium (IGARSS)*, pages 7993–7996. IEEE, 2023

### Submitted patents

- Roland Akiki, Jérémy Anger, Carlo de Franchis, Gabriele Facciolo, and Jean-Michel Morel. Method, device and storage medium for reconstructing a corrected mosaic image from burst images, submitted patent
- Roland Akiki, Carlo de Franchis, Gabriele Facciolo, Raphaël Grandin, and Jean-Michel Morel. Method, device and computer program for measuring a difference of fill ratio of a tank, submitted patent

### Open-source software and online demos

- RPC fitting software: rpcfit
- Demo for phase denoising and coherence estimation network here
- Demo for phase unwrapping network here
- EOS-SAR: Software for the SAR and InSAR processing pipeline. Access can be granted to known collaborators in the research community. Among the supported features are time series coregistration and stitching of Sentinel-1 SLC bursts, orbital and topographic fringe simulation, phase denoising with the uniform filter or Goldstein filter [GW98], phase unwrapping with the minimum cost flow method [Cos98]. An interesting feature is also the possibility of performing mosaics on small areas of interest without the need to process the data from the whole burst.

### Others

- Oral presentation at the MDIS-2022 seminar titled: "Improved Sentinel-1 IW Burst Stitching through geolocation error correction considerations"
- Poster at the FRINGE 2023 workshop titled: "Measuring The Deformation Of Crude Oil Storage Tanks With Interferometry"

# 2 Introduction (en français)

## 2.1 Motivation

Un dispositif d'imagerie par radar à synthèse d'ouverture (RSO ou SAR en anglais) est un système actif. Il se compose généralement d'une antenne montée sur une plate-forme spatiale ou aérienne. L'antenne émet des impulsions électromagnétiques (EM) dans une géométrie à visée latérale et reçoit ensuite des échos qui sont rétro diffusés sur la surface du sol. Les ondes radar d'une longueur d'onde porteuse de $\lambda \in [1 - 20]$ cm subissent des interactions minimales avec les gaz atmosphériques ou les aérosols, ce qui rend le milieu de propagation transparent et non absorbant. Ainsin, contrairement aux capteurs optiques, le SAR a des capacités d'imagerie qui pénètrent les nuages de jour comme de nuit.

Le signal SAR est un nombre complexe, dont l'amplitude est liée à la réflectivité du sol et la phase contient des informations sur le retard du trajet entre le satellite et la cible. Par conséquent, sous certaines contraintes de configuration d'acquisition, il est possible de réaliser un SAR interférométrique (InSAR). Cette technique consiste à comparer la phase d'au moins deux images SAR de la même zone prises à partir de positions d'observation légèrement différentes pour en déduire des informations sur la topographie (précision métrique) et la déformation (précision millimétrique) du sol. Plus précisément, l'InSAR différentiel (DInSAR) utilise l'InSAR pour mesurer la déformation à partir d'acquisitions répétées de la même zone à des moments différents.

Au fil des ans, cette technique s'est révélée très utile dans des domaines tels que la volcanologie, la sismologie, la glaciologie, l'affaissement et le soulèvement du sol. Ces dernières années, la disponibilité des données InSAR a considérablement augmenté, notamment grâce à la politique de données complètes, gratuites et ouvertes du programme Copernicus, y compris en particulier les données SAR de Sentinel-1 depuis le début de la mission en 2014. Jusqu'à l'incident récent de Sentinel-1B en décembre 2021, Sentinel-1 se composait d'une constellation de deux satellites identiques en orbite polaire (A et B) avec un cycle de répétition combiné de 6 jours (12 jours chacun) permettant une couverture quasi globale de la Terre [PINYM+17, PMR+22]. Avec cette quantité de données acquises et distribuées, il est de la plus haute importance d'améliorer nos algorithmes de traitement et de parvenir à un bon compromis entre précision et efficacité.

Étant donné que les images Sentinel-1 sont distribuées sous forme de produits s'étendant sur des centaines de kilomètres et qu'un ensemble de données se compose généralement de nombreux produits consécutifs pouvant être concaténés, les algorithmes de traitement en zone étendue (wide area processing WAP) ont suscité un intérêt croissant et légitime [AGPB13, MDZ+19, LSG+20, TCD+21, CSM+20]. Dans ce cas, l'objectif est généralement d'observer des phénomènes de déformation à moyenne ou grande échelle, ce qui se reflète dans le traitement qui effectue de nombreuses opérations de filtrage et contient souvent des interpolations et/ou un sous-échantillonnage. Cependant, pour certaines applications, il est également intéressant de pouvoir effectuer un traitement localisé sur de nombreuses petites zones dans le monde entier. C'est le cas de la surveillance d'actifs spécifiques, comme les cuves de stockage de pétrole brut étudié au Chapitre 8. Contrairement au WAP, on pourrait affirmer que les exigences en matière de traitement et de modélisation précis devraient être plus strictes, en raison de la nécessité d'extraire des informations à partir de quelques pixels sur l'actif.

L'idée d'un traitement InSAR localisé n'est pas nouvelle et est en fait plus intuitive puisque la mesure InSAR la plus atomique est une différence de phase relative entre des points voisins de l'image. En fait, cette idée a été explorée principalement dans le cadre du traitement *Persistent Scatterer* (PS) à pleine résolution [CMCG+16]. Cependant, même dans ce cas, de nombreux filtres avec des hypothèses de lissage sont utilisés, ce qui remet en question l'indépendance spatio-temporelle de la déformation estimée finale et la quantité de corrélations induites par le traitement. Un autre objectif de cette recherche est de contribuer à l'automatisation de la chaîne de traitement, où les résultats peuvent être produits entièrement sans intervention humaine. Puisque l'une des façons d'atteindre cet objectif pourrait impliquer l'apprentissage automatique à l'avenir, nous explorons certains des modèles d'apprentissage profond qui sont disponibles aujourd'hui pour effectuer certaines tâches InSAR telles que le déroulement de phase ou le débruitage de phase.

Cette thèse a été réalisée chez Kayrros, une société d'intelligence environnementale qui mesure l'impact de l'activité humaine sur l'environnement à l'aide de technologies basées sur les satellites. Les travaux menés ont principalement conduit à l'avancement des algorithmes de traitement SAR, au dépôt de deux brevets [AAdF+nt, AdFF+nt], et à un package Python appelé EOS-SAR (Earth Observation and Sensing - SAR). À Kayrros, ces algorithmes sont couramment utilisés dans les activités de recherche et de développement, et divers produits sont en cours de développement pour des applications telles que la surveillance du stockage du pétrole brut. Ils ont également attiré l'attention de plusieurs chercheurs parmi nos collaborateurs, qui ont commencé à utiliser EOS-SAR dans le cadre de leurs travaux [HG23].

## 2.2 Traitement des données SAR et InSAR

Dans cette section, nous nous penchons sur les concepts clés du traitement SAR et InSAR. Nous commençons par explorer les principes fondamentaux de l'acquisition et de la formation des images SAR, suivis d'une introduction à l'interférométrie. Nous examinons ensuite le modèle de caméra SAR, discutons du recalage et introduisons le concept d'interférométrie différentielle. Enfin, nous présentons des techniques avancées d'interférométrie différentielle.

### 2.2.1 Acquisition SAR et formation d'image

Dans cette section, nous reviendrons brièvement sur le processus d'acquisition SAR et la formation de l'image, comme le montre la Figure 2.1. Pour plus de détails, voir [CW05]. La direction de vol du satellite le long de la trajectoire est appelée azimut, tandis que la direction du faisceau est appelée portée (range). À chaque intervalle de répétition des impulsions en azimut (pulse repetition interval PRI), une impulsion EM est envoyée, puis le satellite reçoit les échos, les démodule (supprime la porteuse), les échantillonne à une

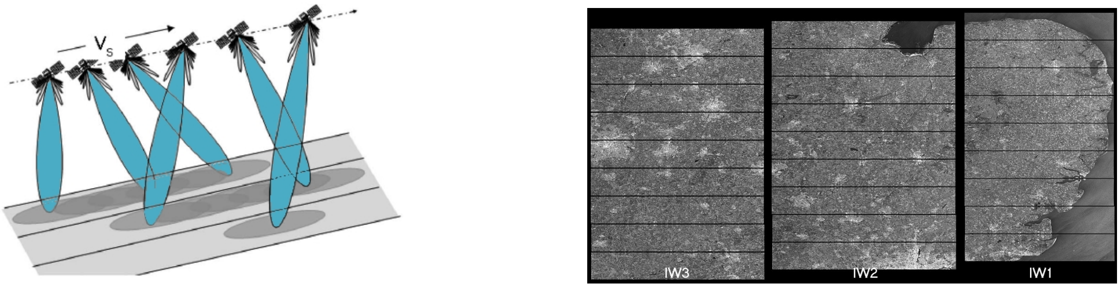

Figure 2.1 : L'acquisition TOPSAR, extraite de [web]. À gauche, nous voyons comment les impulsions EM sont envoyées, avec une rotation continue du faisceau EM dans le sens de la trajectoire et des empreintes qui se chevauchent. Nous voyons également la rotation instantanée du faisceau dans le sens transversal pour acquérir les différentes fauchées. Une image IW de Sentinel-1 est montrée à droite, avec plusieurs bursts dans chacune des trois fauchées IW1, IW2 et IW3.

fréquence d'échantillonnage de portée, les ordonne par distance et les stocke sous forme de nombres complexes en extrayant séparément les amplitudes des composantes en phase et en quadrature du signal. L'image résultante est au format brut (souvent appelé niveau 0 ou L0). En raison de la grande empreinte du faisceau électromagnétique et de la longueur de l'impulsion envoyée, dans ce format, la réponse d'un seul diffuseur au sol est répartie sur de nombreux pixels et la résolution des données est très faible. La résolution peut être améliorée grâce à un processus connu sous le nom de focalisation, qui permet d'obtenir une image SLC (Single Look Complex) au niveau de traitement 1 (L1). Pour comprendre la focalisation, il est utile d'étudier la compression d'impulsion d'un simple chirp unidimensionnel. Considérons que le signal envoyé est un chirp d'une longueur de $T$ secondes avec un taux de chirp de $K$

$$s(t) = \mathrm{rect}\left(\frac{t}{T}\right) \exp\{j\pi K t^2\}, \tag{2.1}$$

où $t$ est le temps et

$$\mathrm{rect}(x) = \begin{cases} 1 & \text{si } |x| \leq 0.5 \\ 0 & \text{sinon.} \end{cases} \tag{2.2}$$

Ce chirp est caractérisé par une fréquence qui varie linéairement avec le temps

$$f_{chirp}(t) = \frac{1}{2\pi} \frac{\partial\{\pi K t^2\}}{\partial t} = Kt \quad \text{(Hz)}. \tag{2.3}$$

Puisque $t \in [-T/2, T/2]$, la fréquence centrale à $t = 0$ est $f_{chirp}(0) = 0$ Hz, et le chirp est considéré comme un signal en bande de base. On considère que le signal reçu est égal au signal envoyé avec un retard de $t_0$ :

$$s_r(t) = \mathrm{rect}\left(\frac{t - t_0}{T}\right) \exp\{j\pi K (t - t_0)^2\}. \tag{2.4}$$

Nous définissons un filtre adapté comme le conjugué complexe inversé dans le temps de s(t) :

$$h(t) = \mathrm{rect}\left(\frac{t}{T}\right) \exp\{-j\pi K t^2\}. \tag{2.5}$$

La sortie de la compression d'impulsion est définie par la convolution :

$$s_{out}(t) = s_r(t) \otimes h(t) = \int_{-\infty}^{+\infty} s_r(u)h(t-u)du \propto \operatorname{sinc}\{KT(t-t_0)\}, \tag{2.6}$$

où

$$\operatorname{sinc}(x) = \frac{\sin(\pi x)}{\pi x}. \tag{2.7}$$

Les équations suivantes montrent clairement comment le chirp reçu de longueur T a été comprimé en un sinus cardinal dont la largeur à 3 dB (décibels) est $\frac{0{,}886}{|K|T}$. Le facteur de compression est $\approx |K|T^2$. Ce principe est à la base de l'amélioration de la résolution de l'image pendant la focalisation. Considérons maintenant un signal hors bande de base, que l'on peut considérer comme un signal dont le temps de fréquence nulle est décalé du centre de l'impulsion de $t_c$ :

$$s(t) = \operatorname{rect}\left(\frac{t}{T}\right)\exp\{j\pi K(t-t_c)^2\}. \tag{2.8}$$

La fréquence du signal est dans ce cas $f_{chirp}(t) = K(t-t_c)$ pour $t \in [-T/2, T/2]$, et la fréquence centrale est $f_c = f_{chirp}(0) = -Kt_c$. En suivant le même raisonnement que précédemment, le signal

$$s_{out}(t) \propto \exp\{j2\pi f_c(t-t_0-t_c)\}\operatorname{sinc}\{KT(t-t_0-t_c)\}. \tag{2.9}$$

On remarque la présence d'une rampe de phase linéaire $2\pi f_c(t-t_0-t_c)$ centrée sur le pic de sinc, avec une pente proportionnelle à $f_c$ (la fréquence centrale du chirp). Pour plus de détails sur la compression d'impulsion, voir le Chapitre 3 de [CW05].

En pratique, lors d'une acquisition SAR, chaque impulsion envoyée est un chirp selon la plage de temps de portée $\tau$ avec un taux de chirp de $K_r$. Par conséquent, chaque impulsion peut être compressée en un sinus cardinal dans la dimension de l'intervalle.

En ce qui concerne la dimension azimutale, nous pouvons également prouver qu'il existe un chirp dans cette direction. Considérons une cible à point unique située au sol et une plate-forme satellitaire progressant à la vitesse $v$ dans une géométrie rectiligne. Le plan qui contient le capteur et qui est orthogonal au vecteur vitesse du capteur est appelé plan Zéro-Doppler, comme le montre la Figure 2.2. Le temps Zéro-Doppler est le moment où le plan Zéro-Doppler traverse la cible. Soit $R(\eta)$ la portée (la distance entre le capteur et la cible) à un temps d'azimut spécifique $\eta$ mesuré par rapport au temps Zéro-Doppler de la cible. $\mathrm{R} = R(0)$ est la portée au temps Zéro-Doppler. En utilisant le théorème de Pythagore, nous pouvons écrire

$$R(\eta) = \sqrt{\mathrm{R}^2 + v^2\eta^2} \approx \mathrm{R} + \frac{v^2\eta^2}{2\mathrm{R}}. \tag{2.10}$$

Sans entrer dans les détails de la dérivation (voir l'équation 4.42 dans [CW05]), l'Équation 2.11 montre l'expression de l'une des composantes de phase présentes dans la réponse impulsionnelle de la cible brute :

$$\Phi_{dop} = \frac{-4\pi R(\eta)}{\lambda} \approx \frac{-4\pi}{\lambda}\left(\mathrm{R} + \frac{v^2\eta^2}{2\mathrm{R}}\right). \tag{2.11}$$

Par conséquent, la phase brute d'une cible présente une évolution quadratique par rapport au temps en azimut $\eta$, c'est-à-dire qu'un chirp est également présent en azimut et peut alors être compressé. C'est la base du concept de radar à synthèse d'ouverture, dans lequel les réponses des différentes impulsions le long de l'azimut sont combinées de manière à imiter une plus grande ouverture d'antenne synthétique. Une autre remarque concerne la désignation Doppler en azimut. Cette analogie vient du fait que le chirp dont la fréquence varie linéairement avec le temps azimutal peut être considéré comme un effet Doppler puisque la plate-forme s'approche de la cible avant le temps Zéro-Doppler et la quitte après. En fait, le décalage Doppler peut s'écrire

$$f_{dop} = \frac{1}{2\pi}\frac{\partial \Phi_{dop}}{\partial \eta} = \frac{-2}{\lambda}\frac{\partial R(\eta)}{\partial \eta} \approx \frac{-2v^2\eta}{\lambda \mathrm{R}} = K_a\eta, \tag{2.12}$$

où $K_a = \frac{-2v^2}{\lambda \mathrm{R}}$ est le taux Doppler azimutal.

Si le centre du faisceau EM pointe dans le plan Zéro-Doppler, on dit qu'il n'a pas d'angle de dépointage et que le chirp en azimut est un signal en bande de base. Lorsqu'il pointe vers l'avant ou vers l'arrière avec un angle de dépointage, le centre du chirp se trouve à un moment $\eta_c$ (temps de croisement de la cible et du centre du faisceau), et nous obtenons un chirp hors bande de base. La fréquence du centroïde Doppler à cet instant ne sera plus nulle et sera égale à $f_{DC} = K_a\eta_c$, et comme nous l'avons vu précédemment dans l'Équation 2.9 pour la compression d'impulsion, cela induira un terme de phase linéaire dans les données focalisées avec une pente de $2\pi f_{DC}$.

Pour Sentinel-1, les images SAR peuvent être acquises selon différents modes. Le mode d'acquisition le plus courant, illustré à la Figure 2.1, est le mode interférométrique à large fauchée (Interferometric Wide IW), qui utilise la technique Terrain Observation with Progressive Scans SAR (TOPS, ou TOPSAR). Les données sont acquises par bursts et, pendant l'acquisition d'un seul burst, le faisceau EM est tourné avec le temps d'azimut d'une position orientée vers l'arrière à une position orientée vers l'avant. Étant donné qu'il s'agit d'une acquisition dépointée avec un taux de rotation uniforme du faisceau, le centroïde Doppler $f_{DC}$ peut être considéré comme linéaire avec le temps d'azimut. Ainsi, les données focalisées contiendront un terme de phase qui, dans ce cas, est quadratique avec le temps d'azimut. La compréhension de ce concept est cruciale pour la manipulation des images SAR car il affecte la manière dont nous rééchantillonnons ce type de données, comme on peut le voir au Chapitre 3, et impose des exigences élevées en matière de précision du recalage en azimut, comme on l'expliquera à la Section 2.2.4.

La présence de la rampe de phase détaillée précédemment doit souvent être prise en compte à des fins de traitement, mais elle sera supprimée des équations InSAR suivantes dans ce chapitre afin de simplifier la notation. En effet, la principale composante de phase intéressante dans l'image SAR focalisée est liée à la distance Zéro-Doppler cible-satellite R comme on peut le voir dans l'équation simplifiée suivante

$$\Gamma = A \exp\{j\Phi\} = A \exp\left\{j\left(\frac{-4\pi \mathrm{R}}{\lambda} + \zeta\right)\right\}, \tag{2.13}$$

où $A$ est l'amplitude de l'image SAR, et $\zeta$ est la phase liée au décalage de diffusion dû aux interactions des micro-ondes avec les cibles.

Un dernier concept est l'intensité $I = \|\Gamma\|^2 = A^2$, qui est l'amplitude au carré. L'intensité est parfois utilisée à la place de l'amplitude en raison de certains avantages liés à la modélisation du bruit ( [TN15]) et à la caractérisation spectrale du signal dans le domaine de Fourier (voir l'analyse des cibles ponctuelles et les concepts de détection de puissance et de magnitude dans [CW05]).

### 2.2.2 Interférométrie

Lorsque l'on dispose d'au moins deux acquisitions SAR alignées (recalées) $\Gamma_1$, $\Gamma_2$ de la même scène, elles peuvent être combinées pour former un interférogramme, comme le montre l'équation suivante

$$\Gamma_{12} = \Gamma_1 \times \Gamma_2^* = A_1 A_2 \exp\left\{j\left(\Phi_1 - \Phi_2\right)\right\} = A_1 A_2 \exp\left\{-j\frac{4\pi}{\lambda}\left(\mathrm{R}_1 - \mathrm{R}_2\right) + j(\zeta_1 - \zeta_2)\right\}. \tag{2.14}$$

On remarque que la phase de l'interférogramme (phase interférométrique) est liée à la variation de la distance satellite-cible. L'InSAR (Interferometric SAR) est donc basé sur ce principe et peut être utilisé pour mesurer la topographie du sol ou le mouvement du sol, comme nous le verrons dans les sections suivantes.

### 2.2.3 Modèle de caméra SAR SLC

Dans cette section, nous expliquerons le modèle de caméra SAR, utilisé pour relier les points 3D à leurs coordonnées 2D dans l'image et vice-versa. Le modèle sera expliqué pour une image SLC focalisée. La géométrie d'acquisition d'un satellite SAR est illustrée à la Figure 2.2. Le système de coordonnées utilisé est l'ECR (Earth Centered Rotational), où l'origine est le centre de la Terre, l'axe X pointe vers l'intersection de l'équateur et du méridien d'origine, l'axe Z pointe vers le pôle nord, l'axe Y peut être facilement déduit.

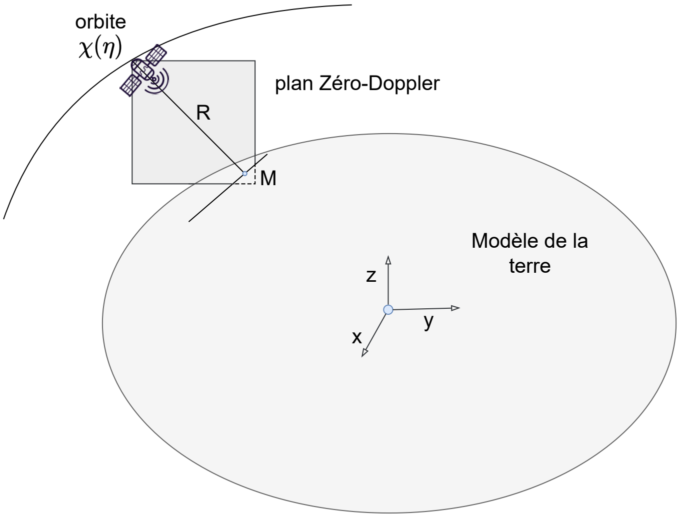

Figure 2.2 : Géométrie simplifiée de l'acquisition SAR. La Terre est représentée par un ellipsoïde gonflé sur lequel se trouve le point M. Le point M est également dans le plan Zéro-Doppler au temps Zéro-Doppler $\eta$. Le point M est également à une distance de R du satellite à ce moment.

Comme indiqué précédemment, le temps de vol d'une impulsion entre le capteur et une cible ponctuelle M au sol déterminera la position du pic de la réponse impulsionnelle le long de la direction de la portée dans les données SLC. Pour simplifier, nous considérerons que la focalisation en azimut a été effectuée à Zéro-Doppler, c'est-à-dire que le temps en azimut des échantillons est leur temps Zéro-Doppler. Si l'on considère une cible dont la portée Zéro-Doppler est R, et que la portée est la direction de la colonne dans l'image

SLC, l'Équation 2.15 nous donne la relation avec la coordonnée de la colonne col

$$\mathrm{R} = \frac{c}{2}\tau = \frac{c}{2}\left(\tau_0 + \frac{\mathrm{col}}{F_r}\right), \tag{2.15}$$

où $c$ est la vitesse de la lumière dans le vide, $\tau_0$ est le délai d'acheminement dans les deux sens jusqu'à la première colonne du SLC et $F_r$ est la fréquence d'échantillonnage de la portée.

Pour la direction azimutale, le numéro de ligne ligne est lié au temps azimutal $\eta$ par l'Équation 2.16, où $F_a$ est la fréquence d'échantillonnage azimutale et $\eta_0$ est le temps de la première ligne dans l'image SLC

$$\eta = \eta_0 + \frac{\mathrm{ligne}}{F_a}. \tag{2.16}$$

$F_r$, $F_a$, $\eta_0$, et $\tau_0$ sont généralement indiqués dans les métadonnées du produit SLC.

Afin de transformer les coordonnées 3D en espace image (projection) et vice versa (localisation), le modèle Range-Doppler peut être utilisé avec les trois équations fondamentales définies dans [Cur82]. Notons $\mathrm{M} = (x_\mathrm{M}, y_\mathrm{M}, z_\mathrm{M})^T$ et $\chi(\eta) = (x_\chi(\eta), y_\chi(\eta), z_\chi(\eta))^T$ respectivement la cible ponctuelle et la position du satellite en représentation vectorielle. La position du satellite peut être extraite des éphémérides en tant que métadonnées. Les données de l'éphéméride consistent en des échantillons régulièrement espacés contenant le temps, la position et la vitesse de la plate-forme avant, pendant et après l'acquisition (appelés "vecteurs d'état" dans le jargon radar). Il est donc courant d'appliquer une technique d'interpolation permettant d'obtenir la position et les dérivées d'ordre supérieur (vitesse $\dot{\chi}(\eta)$, accélération $\ddot{\chi}(\eta)$...) à n'importe quel moment de l'orbite. La distance entre M et $\chi(\eta)$ est égale à la portée, comme le montre l'Équation 2.17

$$E_1 = \mathrm{R}^2 - \|\chi(\eta) - \mathrm{M}\|^2 = 0. \tag{2.17}$$

L'Équation 2.18 indique alors que le point doit se trouver dans le plan Zéro-Doppler :

$$E_2 = \dot{\chi}(\eta).\,(\chi(\eta) - \mathrm{M}) = 0. \tag{2.18}$$

Enfin, la dernière relation présentée dans l'Équation 2.19 indique que le point doit avoir une altitude $h$ par rapport à la représentation ellipsoïdale de la terre (cela dépend du système de référence des coordonnées dans lequel $h$ est indiqué, mais il s'agit généralement de l'ellipsoïde de référence du système géodésique mondial WGS84)

$$E_3 = \frac{x_\mathrm{M}^2 + y_\mathrm{M}^2}{(a+h)^2} + \frac{z_\mathrm{M}^2}{(b+h)^2} - 1 = 0, \tag{2.19}$$

où $a$ représente le rayon équatorial moyen, $b$ le rayon polaire moyen de l'ellipsoïde aplati de la Terre, et $h$ la hauteur du point M au-dessus de l'ellipsoïde. Par conséquent, une façon simple mais légèrement inexacte d'encoder l'information sur la hauteur consiste à placer le point sur l'ellipsoïde gonflé qui a un rayon équatorial de $a + h$ et un rayon polaire de $b + h$.

Lors d'une projection, l'Équation 2.18 suffit à résoudre $\eta$ [KH08]. Le problème revient à trouver la racine de $E_2(\eta)$. La solution est donc trouvée de manière itérative en utilisant la méthode de Newton-Raphson, voir l'Algorithme 3.

```
Algorithme 3: Projection $\mathcal{P}(\mathrm{M})$
Résultat: col, ligne
Entrées: M : cible;  $tol$ : tolérance;  $\chi(\eta)$ : orbite;  $c$ : vitesse de la lumière;
         $\tau_0$ : delai d'acheminenement de la première colonne;
         $F_r$ : fréquence d'échantillonnage de la portée;
         $\eta_0$ : temps azimut de la première ligne;
         $F_a$ : fréquence d'échantillonnage en azimut;
$\eta = \eta_0$;
répéter
    $E_2(\eta) = \dot{\chi}(\eta).(\chi(\eta) - \mathrm{M})$;
    $E_2'(\eta) = \ddot{\chi}(\eta).(\chi(\eta) - \mathrm{M}) + (\dot{\chi}(\eta))^2$;
    $d\eta = -\frac{E_2(\eta)}{E_2'(\eta)}$;
    $\eta = \eta + d\eta$;
jusqu'à $d\eta < tol$;
Utiliser Équation 2.16 pour obtenir ligne;
Utiliser Équation 2.17 pour obtenir R;
Utiliser Équation 2.15 pour obtenir col;
```

Lors de la localisation, nous voulons maintenant récupérer le point M à partir des coordonnées du pixel (col, ligne) et d'une hauteur donnée $h$. Définissons

$$E(\mathrm{M}) = (E_1(\mathrm{M}), E_2(\mathrm{M}), E_3(\mathrm{M}))^T = 0. \tag{2.20}$$

Nous obtenons un système de trois inconnues $x_\mathrm{M}, y_\mathrm{M}, z_\mathrm{M}$ et trois équations. Ce système peut à nouveau être résolu de manière itérative par linéarisation (expansion de Taylor du premier ordre)

$$E(\mathrm{M}) = E(\mathrm{M}_0) + \Delta(\mathrm{M}_0).d\mathrm{M}, \tag{2.21}$$

où

$$\Delta(\mathrm{M}) = \begin{bmatrix} \dfrac{\partial E_1}{\partial \mathrm{M}} \\ \dfrac{\partial E_2}{\partial \mathrm{M}} \\ \dfrac{\partial E_3}{\partial \mathrm{M}} \end{bmatrix} = \begin{bmatrix} \multicolumn{3}{c}{2(\chi(\eta) - \mathrm{M})^T} \\ \multicolumn{3}{c}{-\dot{\chi}(\eta)^T} \\ \dfrac{2x_\mathrm{M}}{(a+h)^2} & \dfrac{2y_\mathrm{M}}{(a+h)^2} & \dfrac{2z_\mathrm{M}}{(b+h)^2} \end{bmatrix}. \tag{2.22}$$

Puisque nous cherchons $E(\mathrm{M}) = 0$, nous devons résoudre itérativement pour $d\mathrm{M}$

$$-E(\mathrm{M}_0) = \Delta(\mathrm{M}_0).d\mathrm{M}. \tag{2.23}$$

Pour initialiser M dans l'Algorithme 4, nous pouvons utiliser les coordonnées de longitude et de latitude du centroïde de l'image ($lon_{mid}, lat_{mid}$) car elles peuvent généralement être déduites des métadonnées (emplacement approximatif de la scène imagée). Ensuite, nous convertissons le point ($lon_{mid}, lat_{mid}, h$) dans le système de coordonnées ECR pour obtenir $\mathrm{M}_{init}$.

```
Algorithme 4: Localisation $\mathcal{L}(\text{ligne}, \text{col}, h)$
Résultat: $\mathrm{M} = (x_{\mathrm{M}}, y_{\mathrm{M}}, z_{\mathrm{M}})^T$
Entrées: (ligne, col) : Coordonnées dans l'image SAR ;   $h$ : hauteur ;
        $tol$ : tolérance ;   $\chi(\eta)$ : orbite ;   $c$ : vitesse de la lumière ;
        $\tau_0$ : delai d'acheminenement de la première colonne ;
        $F_r$ : fréquence d'échantillonnage de la portée ;
        $\eta_0$ : temps azimut de la première ligne ;
        $F_a$ : fréquence d'échantillonnage en azimut ;
        $\mathrm{M}_{init}$ : Estimation initiale ;   $(a, b)$ : Dimensions ellipsoïde terrestre ;
$\mathrm{M} = \mathrm{M}_{init}$ ;
Utiliser Équation 2.16 pour obtenir $\eta$ à partir de ligne ;
Utiliser Équation 2.15 pour obtenir R à partir de col;
répéter
    Calculer $E(\mathrm{M})$;
    Calculer $\Delta(\mathrm{M})$;
    Résoudre $-E(\mathrm{M}) = \Delta(\mathrm{M}).d\mathrm{M}$ pour trouver $d\mathrm{M}$;
    $\mathrm{M} = \mathrm{M} + d\mathrm{M}$
jusqu'à $dM_x < tol$ , $dM_y < tol$ , $dM_z < tol$;
```

Les équations et algorithmes précédents donnent une première approximation de la géolocalisation d'une image SAR, généralement avec une précision inférieure au pixel (en fonction de l'éphéméride et de la précision des informations temporelles). Toutefois, dans la pratique, pour obtenir la plus grande précision possible, il faut tenir compte de nombreux effets dus à des phénomènes physiques et à des détails du traitement des données. Les effets à prendre en compte [GSB+20] sont les retards de trajectoire introduits par l'atmosphère terrestre (troposphère, ionosphère), les effets des marées (principalement les marées terrestres solides, la charge océanique...), la tectonique des plaques (donnée sous forme de vitesses de déformation dans le Système international de référence terrestre ITRF par exemple), et divers effets temporels (effets bistatiques, décalage Doppler intra-impulsion, décalage du taux Doppler FM...). Dans le Chapitre 5, nous considérons certains de ces effets dans notre étude, tels que le retard troposphérique et l'effet intra-impulsion en portée, et l'effet bistatique en azimut.

Le retard troposphérique est dû au fait que la vitesse de l'onde électromagnétique est en fait inférieure à la vitesse de la lumière dans le vide. Même s'il existe des méthodes précises reposant sur une modélisation avancée de l'état de l'atmosphère [HIKK08, JGL+11, YLPC18, CBGE18], un modèle simple peut également donner une bonne approximation de cet effet [JPS+08] :

$$\delta \mathrm{R} = \frac{1}{\cos \alpha_{\mathrm{inc}}} \left( \frac{h^2}{8.55 \cdot 10^7} - \frac{h}{3411} + 2.41 \right) \quad [\mathrm{m}], \tag{2.24}$$

ou $\delta$R est le décalage de distance qui induirait le retard atmosphérique dans le vide, h est la hauteur, et $\alpha_{inc}$ est l'angle d'incidence.

Quant au décalage bistatique observé en azimut, il s'explique par l'examen du système d'émission-réception du satellite. Cette correction tient compte du fait que le satellite ne s'arrête pas à une position fixe en orbite pour attendre que l'impulsion se réfléchisse sur le sol jusqu'à la réception (approximation "stop-and-go"). En réalité, le satellite continue à se déplacer et à transmettre des impulsions à chaque intervalle PRI. À l'intérieur d'un

PRI, après chaque fenêtre de transmission, il y a une fenêtre de réception. Une impulsion transmise dans la fenêtre $(i)$ est reçue dans la fenêtre de réception $(i + rang)$. Les paquets d'échos 1D doivent ensuite être réorganisés sous la forme d'une image 2D, en associant à chaque écho un temps d'azimut, qui se situe idéalement au milieu entre l'émission et la réception. Lorsque cela n'est pas déjà pris en compte lors de la construction de l'image SAR, ce qui est le cas de Sentinel-1, un décalage azimutal linéaire en fonction de la portée sera présent dans les données [GSB+20].

L'effet intra-impulsion dans Sentinel-1 vient du fait que la fréquence Doppler d'une cible varie le long de l'azimut même à l'intérieur d'un burst, alors que le processeur au niveau du burst suppose une fréquence unique pour la durée du burst. Par conséquent, un biais de portée sera introduit pour une cible donnée qui dépend de son décalage azimutal par rapport au centre du burst. Pour les produits IW, cet effet peut entraîner des erreurs de portée de l'ordre de 0,5 m aux limites supérieure et inférieure du burst.

Les effets de la correction temporelle doivent être calculés au niveau d'un burst de Sentinel-1. En outre, pour certains d'entre eux, la géométrie 3D avec le capteur est également nécessaire, comme le décalage en azimut induit par la topographie et dû à la non-concordance des taux FM Doppler [GSB+20]. Par conséquent, le calcul de certains décalages n'est pertinent que dans le contexte de la géolocalisation d'un burst Sentinel-1. En outre, le produit ETAD (extended timing annotation dataset) récemment développé pour Sentinel-1 fournit les corrections temporelles les plus importantes par burst. Il a été démontré que l'utilisation de ces corrections temporelles améliore les flux de traitement des applications SAR établies telles que le télémétrage absolu des cibles, le suivi des décalages et l'interférométrie [GLM+22, SGB+23].

Comme on peut le voir dans cette section, le modèle physique du capteur pour les données SAR nécessite une bonne connaissance du processus d'acquisition. C'est pourquoi il serait intéressant de remplacer ce modèle complexe par un modèle plus simple, par exemple le modèle de caméra à coefficients polynomiaux rationnels RPC. Certaines agences spatiales ont commencé à adopter cette approche, comme le montre le satellite chinois Gaofen 3 [WZY+17]. Une autre raison d'utiliser le modèle fonctionnel rationnel est son efficacité informatique. L'application d'une fonction de géolocalisation revient à évaluer la valeur de polynômes, alors que les Algorithmes 3 et 4 sont plus coûteux car ils utilisent une procédure d'optimisation itérative. Dans le Chapitre 4, nous montrons que nous pouvons estimer des modèles RPC précis à partir du modèle physique de Sentinel-1.

### 2.2.4 Recalage

Dans cette section, nous examinerons quelques-unes des différentes méthodes qui peuvent être utilisées pour aligner les images SAR. Le recalage est généralement une étape de prétraitement nécessaire pour toute analyse de série temporelle et se réfère au processus de rééchantillonnage d'une image secondaire sur le système de référence d'une image primaire de telle sorte que les mêmes éléments au sol soient situés à la même position de pixel dans les deux images. La première technique est la méthode géométrique qui repose sur la projection d'un ensemble de points 3D échantillonnés à partir d'un modèle numérique d'élevation (MNE) sur l'image primaire et l'image secondaire. La projection est réalisée via le modèle de caméra détaillé dans la Section 2.2.3, qui peut être soit physique, soit fourni sous forme de fonctions RPC. L'ensemble des correspondances 2D obtenues peut être utilisé pour estimer une transformation. Dans [SBM+06], un terme de biais dans la transformation est estimé à partir de points de rattachement, en raison d'erreurs potentielles dans la fonction de projection. En d'autres termes, l'alignement estimé avec la méthode géométrique est souvent affiné à l'aide d'estimations à partir des données SAR.

Parmi les différentes méthodes permettant d'effectuer cette estimation fine, nous distinguons la corrélation et la diversité spectrale (ou interférométrie à bandes séparées). Pour des diffuseurs gaussiens distribués, il a été démontré que la corrélation croisée cohérente utilisant les échantillons complexes atteint la meilleure précision possible (la limite de Cramér-Rao), mais une attention particulière doit être apportée à l'élimination des différences de phase systématiques non bruitées. Il est également possible d'effectuer une corrélation croisée incohérente (également connue sous le nom de "speckle tracking") sur l'amplitude ou l'intensité (carré de l'amplitude), même si ces estimations sont théoriquement moins précises que leur équivalent cohérent [De 14]. Quant à la méthode de diversité spectrale, elle repose sur le concept de la division de l'image en sous-ouvertures filtrées par passe-bande dans les gammes de fréquences inférieure et supérieure. Les interférogrammes des gammes inférieure et supérieure sont ensuite formés et un interférogramme différentiel final est généré, où la phase est proportionnelle au décalage résiduel, avec une sensibilité liée à la séparation spectrale entre les fréquences centrales des sous-ouvertures [SM00]. Le principe de cette méthode consiste à générer artificiellement des images SAR de sous-ouverture qui ne sont pas en bande de base, de sorte que la réponse impulsionnelle dans les données focalisées contient un terme de phase linéaire avec la dimension du pixel (portée ou azimut), comme le montre l'Équation 2.9. Cette méthode a une précision très proche de la limite de Cramér Rao [BE05].

En outre, la technique *Enhanced Spectral Diversity* (ESD) a été proposée pour le mode TOPS de TerraSAR-X, principalement pour l'interférométrie. En effet, comme indiqué dans la Section 2.2.1, pour le mode TOPS, en raison de la rotation du faisceau EM pendant l'acquisition des bursts, la fréquence du centroïde Doppler augmente linéairement avec le temps d'azimut et atteint des valeurs élevées sur les bords des bursts. Un mauvais recalage azimutal induira des rampes de phase azimutales non négligeables dans les interférogrammes des bursts. La précision requise pour que l'erreur reste inférieure à 3.6° (1 / 100 cycle) est d'environ $8 \times 10^{-4}$ pixels, et peut être atteinte avec la technique ESD. La technique ESD utilise les régions de chevauchement des bursts de la même manière que les sous-ouvertures dans la technique de diversité spectrale. Les régions de chevauchement sont des images représentant les mêmes caractéristiques au sol, mais caractérisées par des fréquences centroïdes Doppler très élevées et de signes opposés. Ainsi, pour appliquer la technique de diversité spectrale, il n'est pas nécessaire de synthétiser des sous-ouvertures en azimut et les chevauchements peuvent être directement utilisés à la place. En raison de la grande séparation spectrale des fréquences centrales du chevauchement, la précision de recalage en azimut que l'on peut atteindre avec cette technique est la plus élevée possible parmi les différentes méthodes et est généralement suffisante pour éviter les rampes de phase en azimut. L'ESD peut également être utilisée pour récupérer la déformation dans le sens de la trace au niveau des chevauchements [GKMV16,YMPIPJ19]. Certaines améliorations ont été apportées à la technique ESD au fil des ans, comme l'inversion des décalages par paire dans le cadre d'une série chronologique, comme indiqué dans [YMDPI17] ou dans la méthode ESD basée sur le réseau (Network-based ESD method - NESD) [FAS17].

En ce qui concerne plus particulièrement le recalage de Sentinel-1, il existe de nombreuses méthodes et variantes [WWS+16,Gra15,YMPIG+16,HNBM16,FAS17,MDZ+19,LSG+20], mais l'idée générale est en grande partie la même. Tout d'abord, un recalage géométrique est effectué à l'aide d'orbites satellitaires précises et d'un MNE. Ensuite, le raffinement peut être effectué avec une technique de corrélation croisée par exemple, mais cette étape est parfois omise ou seulement appliquée dans la direction de portée. Enfin, la technique ESD est utilisée pour atteindre une précision maximale en azimut si l'application souhaitée est l'interférométrie. En outre, le recalage est parfois réalisée sur des bursts individuels qui sont ensuite assemblés, ou sur une mosaïque de bursts. Dans le Chapitre 5, nous effectuons un recalage géométrique par burst, puis nous assemblons les bursts pour obtenir une mosaïque précise.

### 2.2.5 Interférométrie différentielle - DInSAR

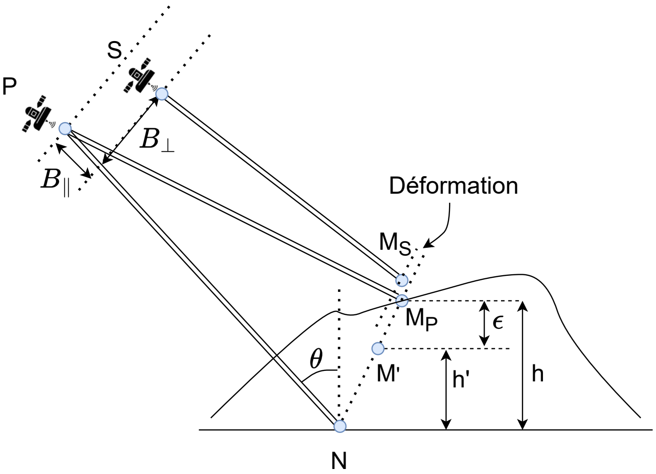

Figure 2.3 : Principe de l'interférométrie différentielle (DInSAR). La scène est acquise à partir d'un satellite à deux positions P (Primaire) et S (Secondaire), correspondant à deux passages à des dates différentes le long de la même orbite. Entre les deux dates, la cible s'est déplacée de la position $\mathrm{M_P}$ à la position $\mathrm{M_S}$. L'échelle de la figure est inexacte à des fins de visualisation : la déformation (millimétrique) est en fait inférieure de plusieurs ordres de grandeur à la distance satellite-cible (centaines de kilomètres) et à la topographie (mètres, en fonction du terrain). La figure montre également le point N, qui aurait été acquis dans la même cellule d'échantillonnage en l'absence de topographie sur la surface de référence. De même, le point $\mathrm{M}'$ est la localisation du point M donnée par une source de données externe, telle qu'un MNE. La hauteur supposée $h'$ de $\mathrm{M}'$ comporte une erreur par rapport à la hauteur réelle $h$ de $\epsilon$. Les bases géométriques $B_\perp$ et $B_\parallel$ et l'angle d'incidence $\theta$ sont également représentés.

La plupart des satellites SAR interférométriques peuvent acquérir la même scène à partir d'une géométrie d'observation similaire après quelques jours. Cette capacité à effectuer des acquisitions répétées permet de mesurer la déformation du sol au cours du temps grâce au principe de l'interférométrie différentielle (DInSAR), illustré à la Figure 2.3. Le satellite est en position primaire (P) pour une date et en position secondaire (S) pour une autre. Leur séparation spatiale $B = \|\mathrm{PS}\|$ est appelée base géométrique et peut atteindre des valeurs de quelques centaines de mètres pour Sentinel-1 [PINYM+17]. Supposons que le point M subisse une légère déformation (de l'ordre du millimètre) entre les deux dates. En regardant l'Équation 2.14, la phase interférométrique peut être écrite comme :

$$\Phi_{12} = -\frac{4\pi}{\lambda}(\|\mathrm{PM_P}\| - \|\mathrm{SM_S}\|) + \zeta_1(\mathrm{M_P}) - \zeta_2(\mathrm{M_S}). \tag{2.25}$$

Nous supposons que les phases de diffusion sont égales pour les deux dates et qu'elles se compensent. Nous pouvons également réécrire l'Équation 2.25 comme suit

$$\Phi_{12} = O_{12} + \Xi_{12} + \mu_{12}\,, \tag{2.26}$$

où

$$O_{12} = -\frac{4\pi}{\lambda}(\|\mathrm{PN}\| - \|\mathrm{SN}\|)\,, \tag{2.27}$$

est la phase orbitale et

$$\Xi_{12} = -\frac{4\pi}{\lambda}\left\{(\|\mathrm{PM_P}\| - \|\mathrm{SM_P}\|) - (\|\mathrm{PN}\| - \|\mathrm{SN}\|)\right\}\,, \tag{2.28}$$

est la phase topographique et

$$\mu_{12} = -\frac{4\pi}{\lambda}(\|\mathrm{SM_P}\| - \|\mathrm{SM_S}\|) = -\frac{4\pi}{\lambda}\mathrm{D}_{12}, \tag{2.29}$$

est la phase de déformation, avec $\mathrm{D}_{12} = (\|\mathrm{SM_P}\| - \|\mathrm{SM_S}\|)$ définie comme la déformation entre les deux dates (avec cette convention, une déformation positive correspond à un mouvement vers le satellite). Les composantes de la phase orbitale et topographique peuvent être approximées avec

$$O_{12} = -\frac{4\pi}{\lambda}B_{\parallel,12}, \tag{2.30}$$

$$\Xi_{12} = -\frac{4\pi}{\lambda}\frac{B_{\perp,12}}{\mathrm{R}\sin\theta}h. \tag{2.31}$$

L'objectif étant de mesurer la déformation, les phases orbitales et topographiques sont simulées pour chaque pixel de l'interférogramme à l'aide du modèle de caméra (par exemple, les Algorithmes 3 et 4) et d'un modèle numérique d'élévation (MNE). Par exemple, une façon d'effectuer la simulation est décrite comme suit. Pour un ensemble de points (N) sur l'ellipsoïde, il est possible de déterminer les positions satellitaires Zéro-Doppler (P ou S de $\chi(\eta)$) et la portée R en utilisant l'Algorithme 3, et donc de calculer les bases ($B_{\perp,12}$, $B_{\parallel,12}$) et les angles d'incidence ($\theta$) pour ces points ; Comme l'Algorithme 3 nous donne également les coordonnées dans l'image SAR, les bases et les angles d'incidence peuvent être interpolés pour tous les pixels de l'image primaire. À ce stade, une simulation de la phase orbitale $O_{12}^{sim}$ peut déjà être calculée avec l'Équation 2.30. Si un MNE est également disponible, nous donnant la localisation 3D d'un ensemble de points $\mathrm{M}'$ dans la scène, l'Algorithme 3 peut également être appliqué pour déduire les coordonnées de chaque point 3D dans l'image primaire, et la hauteur $h'$ peut alors être interpolée pour tous les pixels ("backgeocoding" [LCRCPIP21]). L'Équation 2.31 peut ensuite être utilisée pour calculer la phase topographique simulée $\Xi_{12}^{sim}$. Enfin, la phase interférométrique différentielle est obtenue avec

$$\phi_{12} = \angle\left\{\Gamma_{12}\cdot e^{-jO_{12}^{sim}}e^{-j\Xi_{12}^{sim}}\right\}, \tag{2.32}$$

où $\angle$ donne la phase dans l'intervalle $[-\pi, \pi)$. En pratique, les phases simulées ne sont pas parfaites, principalement en raison de l'imprécision des orbites et du MNE. Après la compensation, il reste une phase orbitale résiduelle $o_{12}$ et une phase topographique résiduelle $\xi_{12}$. On peut également relier $\xi_{12}$ à l'erreur topographique résiduelle du MNE (RTE $\epsilon = h - h'$), en remplaçant $\Xi_{12}$ et $h$ par $\xi_{12}$ et $\epsilon$ dans l'Équation 2.31 respectivement : $\xi_{12} = -\frac{4\pi}{\lambda}\frac{B_{\perp,12}}{\mathrm{R}\sin\theta}\epsilon$. En outre, il faut tenir compte des délais de propagation des ondes dans l'atmosphère $\alpha_{12}$, du bruit exprimé par $n_{12}$, et de l'ambiguïté de phase exprimée $2\pi k_{12}$

puisque la phase ne peut être observée que dans l'intervalle $[-\pi, \pi)$. L'équation DInSAR peut donc s'écrire comme suit :

$$\begin{aligned}\phi_{12} &= \mu_{12} + \xi_{12} + o_{12} + \alpha_{12} + n_{12} + 2\pi k_{12} \\ &= -\frac{4\pi}{\lambda}\mathrm{D}_{12} - \frac{4\pi}{\lambda}\frac{B_{\perp,12}}{\mathrm{R}\sin\theta}\epsilon + o_{12} + \alpha_{12} + n_{12} + 2\pi k_{12}.\end{aligned} \tag{2.33}$$

La phase de l'Équation 2.33 n'est pas seulement liée à la déformation mais contient également de nombreuses autres contributions. Pour surmonter cette limitation, on peut tout d'abord atténuer la phase atmosphérique $\alpha_{12}$ en simulant les retards des ondes électromagnétiques dans la troposphère à l'aide de modèles météorologiques numériques [HIKK08, JGL+11, YLPC18, CBGE18] ou en modélisant leur dépendance linéaire par rapport à la topographie [CAT+07, CDLB07, LQDT+09, Zeb21]. Le bruit $n_{12}$ peut être réduit par le débruitage, pour lequel une revue peut être trouvée à [XGLX20]. La cohérence, c'est-à-dire la magnitude de la corrélation croisée complexe normalisée, est souvent liée au débruitage. En effet, le débruitage de la phase et le calcul de la cohérence relèvent tous deux de l'estimation des paramètres interférométriques [VTCB04, DDT11, DDT+15, SGRB21]. La cohérence peut être utile pour des traitements ultérieurs tels que le déroulement de phase, qui est le processus de résolution de l'ambiguïté $2\pi k_{12}$ [GZW88, PS94, PJJ94, TNM98, Cos98, GP98, CZ01, YLY+19]. Enfin, une façon d'atténuer la phase orbitale $o_{12}$ est de la modéliser comme un polynôme ajusté par rapport aux coordonnées de l'image en azimut et en portée [DFL+21, LQDT+09]. Toutes les méthodes d'atténuation ne sont pas parfaites, et le DInSAR est donc principalement adapté aux cas d'utilisation où le signal de déformation est suffisamment élevé pour dominer toutes les autres contributions, comme dans le cas des tremblements de terre. Enfin, en examinant la phase de déformation $\mu_{12}$ de l'Équation 2.29, nous remarquons que :

- La déformation est mesurée dans la ligne de visée (LDV) du satellite, c'est-à-dire dans la direction définie par la ligne reliant le satellite à la cible.
- La sensibilité à la déformation est très élevée. En effet, une déformation de $\frac{\lambda}{2}$ induira un cycle ($2\pi$ radians). Par exemple, pour Sentinel-1 opérant dans la bande C, $\frac{\lambda}{2} \approx 2.8$ cm.

Par conséquent, la technique DInSAR permet de mesurer la déformation dans la LDV avec une précision de l'ordre du centimètre. Elle est applicable lorsque le gradient de phase entre les points voisins est inférieur à $\pi$ en valeur absolue (condition d'Itoh liée au déroulement de la phase [GP98]). Cela signifie que les gradients de déformation sont faibles, c'est-à-dire que la déformation relative entre les points voisins en valeur absolue doit être inférieure à $\frac{\lambda}{4}$, soit $\approx 1.4$ cm pour Sentinel-1. Dans les Chapitres 6 et 7, nous explorons les performances de certains réseaux d'apprentissage profond sur les tâches DInSAR, à savoir le débruitage de phase et l'estimation de la cohérence, ainsi que le déroulement de la phase.

### 2.2.6 DInSAR Avancé

Les méthodes DInSAR Avancé (A-DInSAR, ou interférométrie radar à séries temporelles, InSAR multitemporel...) fonctionnent non seulement sur un couple d'images SAR (produisant un seul interférogramme) mais aussi sur une pile de $\mathrm{L}+1$ images SAR. Par conséquent, il existe L d'interférogrammes DInSAR indépendants qui peuvent être formés par rapport à une seule image (par exemple, celle du milieu de la série temporelle), ou $\frac{(\mathrm{L}+1)\mathrm{L}}{2}$ quantité maximale d'interférogrammes redondants. En utilisant cette information temporelle, nous pourrions résoudre l'Équation 2.33 plus facilement pour obtenir la déformation (série temporelle de la déformation $\mathrm{D}_{1u}$ pour $u = \{2 \dots \mathrm{L}{+}1\}$). En effet, la déformation est généralement modélisée comme ayant une évolution régulière dans le temps, des modèles linéaires, polynomiaux ou saisonniers étant parfois adoptés [FPC23]. En outre, la base orthogonale varie pour chaque paire d'images de la pile, ce qui permet d'ajuster la hauteur topographique résiduelle $\epsilon$. Quant au déroulement de la phase, il doit prendre en compte la dimension temporelle, soit en combinant un déroulement spatial 2D avec un déroulement temporel 1D (ou un contrôle de conformité temporel) [DCM+14,BPPJL20,LQDT+09], soit en adoptant une approche de déroulement 3D complète [HZ07, CMM12, PL06]. Enfin, la phase atmosphérique est supposée présenter de faibles variations dans l'espace et de fortes variations dans le temps et peut donc être filtrée à partir des phases déroulées [FPR00]. Il s'agit là de quelques éléments utilisés pour réaliser l'estimation de la déformation, mais de nombreuses méthodes ont été développées au fil des ans, parmi lesquelles nous distinguons trois classes :

- PS : Une famille de méthodes qui détectent et restreignent l'estimation sur des réflecteurs forts et stables dans l'image avec un faible niveau de bruit à travers la série temporelle appelée *Persistent Scatterers* [FPR00, FPR01].
- SBAS (ou DS) : Une famille de méthodes qui travaillent sur des *Distributed Scatterers*, c'est-à-dire des cibles qui n'ont pas de réponse stable par elles-mêmes mais qui présentent une phase cohérente lorsqu'elles sont regroupées avec des cibles voisines ayant des caractéristiques similaires [BFLS02, LMM+04].
- Méthodes hybrides PS + DS : Traitement conjoint des PS et DS, comme dans [FFN+11, ADB18, MN22].

Veuillez vous référer à [MHR20, CMCG+16] pour un aperçu plus exhaustif. Ces méthodes ont permis de grandes avancées dans le développement de chaînes de traitement automatisées pour récupérer les séries temporelles de déformation. Les méthodes PS et SBAS sont complémentaires et détectent les phénomènes de déformation à différentes échelles. Comme la méthode PS travaille à l'échelle des diffuseurs individuels, elle est plus intéressante pour les mesures localisées. Cependant, certaines des hypothèses faites dans un processeur PS générique peuvent encore être trop sévères, en particulier pour les pixels présentant une déformation non linéaire ou même une déformation discontinue rapide. Par exemple, l'hypothèse de mouvement linéaire est parfois utilisée pour détecter les pixels PS, et peut négliger certains pixels présentant un comportement non linéaire [YDLQ+12, CSM+20]. En outre, même si le pixel est détecté, un filtrage temporel visant à supprimer les composantes atmosphériques peut également lisser excessivement la série temporelle de déformation récupérée. Par conséquent, lorsque nous effectuons nos mesures localisées dans le Chapitre 8, nous n'appliquons pas un schéma de traitement PS générique pour éviter de perdre des informations, mais nous utilisons seulement certains concepts de la technique PS.

## 2.3 Aperçu bref de la thèse

Cette thèse est divisée en trois parties. La première partie, qui comprend les Chapitres 3 à 5, contient nos contributions à la chaîne de traitement SAR. En particulier, nous étudions d'abord différentes approches liées au deramping, c'est-à-dire à la suppression de la rampe de phase du centroïde Doppler introduite dans la Section 2.2.1. Le deramping est une étape cruciale pour le rééchantillonnage des bursts de Sentinel-1. Nous montrons ensuite la possibilité de remplacer le modèle physique du capteur SAR de Sentinel-1 par un

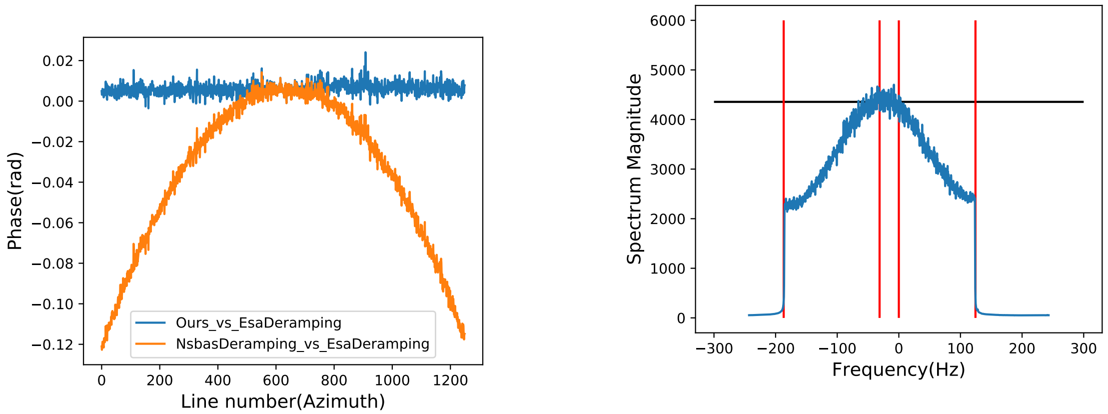

(a) Le profil de différence de phase InSAR

(b) Le décalage fréquentiel de notre méthode "Ours"

FIGURE 2.4 : Expériences de deramping dans le Chapitre 3. À gauche, nous montrons que "NsbasDeramping" introduit une phase quadratique le long de l'azimut, qui n'est pas présente dans notre méthode "Ours". À droite, les deux méthodes présentent un décalage spectral avant le rééchantillonnage

modèle de caméra RPC. Pour conclure la première partie, nous présentons une méthode permettant d'obtenir une série temporelle de mosaïques de bursts de Sentinel-1 géométriquement précises et recalées. Dans la deuxième partie, qui comprend les Chapitres 6 à 7, nous évaluons brièvement certains réseaux d'apprentissage profond appliqués à des tâches InSAR telles que le débruitage de phase, l'estimation de la cohérence et le déroulement de phase. Enfin, la troisième partie contenant le Chapitre 8 applique DInSAR aux cuves de stockage de pétrole brut et montre le potentiel de la technique dans la mesure du volume de pétrole brut.

**Chapitre 3 : Comparaison des techniques de deramping TOPS de Sentinel-1**
Ce chapitre compare les différentes méthodes de centrage spectral (appelées deramping) pour les images Sentinel-1 acquises en mode TOPSAR, dans le contexte de l'interférométrie. Le décalage spectral (la fréquence du centroïde Doppler) augmente linéairement avec le temps d'azimut du burst en raison de la rotation uniforme du faisceau EM. Il est donc nécessaire de centrer les fréquences dans le domaine de Fourier autour de 0 Hz avant l'interpolation de l'image. Nous montrons l'analogie entre deux approches dans la littérature, la fonction de deramping conventionnelle prescrite par l'ESA et celle mise en œuvre dans le logiciel NSBAS. Nous montrons que la fonction de deramping de NSBAS peut induire une petite erreur de rampe de phase quadratique dans la phase interférométrique le long de l'azimut. Nous proposons une méthode de deramping qui ne souffre pas de cette imprécision. La méthode est analogue à l'application de la fonction de deramping de l'image primaire pour toutes la série temporelle, comme cela a été proposé dans [HNBM16]. Nous validons par des expériences sur des données réelles de Sentinel-1 que l'erreur qui atteint 0.12 rad sur les limites des bursts avec le deramping NSBAS n'est pas présente dans notre méthode, comme le montre la Figure 2.4. Cependant, les deux méthodes de deramping proposée et celle d'NSBAS ne recentrent qu'approximativement le spectre, ce qui signifie qu'un petit décalage spectral résiduel subsiste. Nous dérivons une expression de forme fermée pour le décalage résiduel prévu et montrons que le décalage résiduel est généralement faible sur un ensemble de données Sentinel-1 (moins de 35 Hz). Nous vérifions également que l'interpolation des images contenant ce décalage spectral

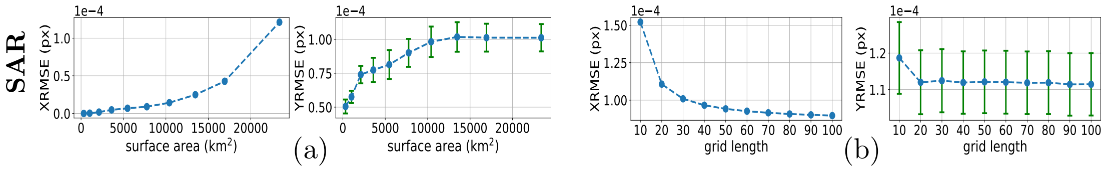

(a) (b)

Figure 2.5 : Erreur de reprojection des RPC en fonction de la longueur de la grille et de la surface sur l'ensemble de données SAR Sentinel-1 dans le Chapitre 4. Chaque barre verticale correspond aux valeurs $[-\sigma/2, \mu, \sigma/2]$ de l'erreur quadratique moyenne (RMSE) évaluée sur les différentes images de l'ensemble de données, dans chaque dimension du plan de l'image, où $\mu$ correspond à la moyenne et $\sigma$ à l'écart-type.

résiduel ne devrait pas induire de baisses considérables de la cohérence interférométrique. La méthode de deramping proposée n'est avantageuse que lorsqu'il s'agit de recaler une série temporelle de N images SAR secondaires sur une image primaire. Dans ce cas, N + 1 opérations de deramping sont nécessaires avec la méthode proposée, contrairement aux 2 * N opérations de deramping avec l'approche conventionnelle.

**Chapitre 4 : Modélisation robuste de la caméra RPC**

Ce chapitre décrit un algorithme indépendant du terrain permettant de dériver avec précision un modèle à coefficients polynomiaux rationnels (RPC) à partir d'un ensemble de correspondances de points 3D-2D sur la base d'une estimation par moindres carrés régularisés. Le modèle de caméra RPC peut être utilisé pour décrire une variété de systèmes d'acquisition d'images en télédétection, notamment les capteurs optiques et les radars à synthèse d'ouverture (SAR). Les fonctions RPC relient les coordonnées 3D aux coordonnées 2D et vice versa, indépendamment des spécificités physiques des capteurs, ce qui en fait un outil essentiel pour exploiter les images satellite de manière générique. L'algorithme d'estimation décrit définit automatiquement le paramètre de régularisation à l'aide d'une heuristique de courbe en L et est également pondéré de manière itérative, c'est-à-dire que la solution d'une itération est utilisée pour définir le poids de l'itération suivante. La précision du RPC ajusté est évaluée en faisant varier le nombre de correspondances de points et la taille de la zone qu'ils couvrent. Nous testons l'algorithme sur les données SAR de Sentinel-1 et les données optiques de WorldView-3, pour dériver des RPC à partir de modèles de capteurs physiques ou d'autres modèles de RPC après composition avec des fonctions de correction. Les résultats pour Sentinel-1 sont présentés dans la Figure 2.5. Nous montrons que l'augmentation du nombre de correspondances réduit légèrement le RMSE. Nous montrons également qu'il est plus facile d'ajuster la fonction RPC sur une surface plus petite. Pour la plupart des configurations, le RPC estimé présente des erreurs de l'ordre de $10^{-4}$ pixels en termes de RMSE sur une grille de points de validation, ce qui confirme la capacité du modèle à représenter des correspondances de géolocalisation complexes.

**Chapitre 5 : Assemblage des bursts basé sur la géolocalisation pour Sentinel-1 IW**

Ce chapitre propose une méthode pour construire une mosaïque précise des bursts de Sentinel-1. En effet, depuis la phase de mise en service de Sentinel-1A, plusieurs études de calibration ont permis d'améliorer la géolocalisation et la modélisation géométrique des données, comme indiqué dans la Section 2.2.3. La mise en œuvre des corrections présentées dans ces études est laissée à l'utilisateur, et le sujet gagne en attention avec la publication prévue de l'ensemble de données ETAD (Extended Timing Annotation Dataset). Les cor-

| | Avant la correction | Après la correction |
|---|---|---|
| décalage az (m) | 0.086 ± 0.35 | 0.15 ± 0.334 |
| décalage rg (m) | -0.57 ± 0.16 | -0.021 ± 0.15 |

Tableau 2.1 : Décalage de recalage mesuré indiqué au Chapitre 5 entre les chevauchements des bursts "i" et "i+1". La mesure a été effectuée sur 31 images S1 sur la première fauchée et sur les 8 chevauchements. Chaque mesure est présentée avec et sans l'application de la méthode de rééchantillonnage proposée. Le tableau indique la valeur moyenne et l'écart-type en mètres. Remarquez l'amélioration de l'alignement dans la direction de la portée, où un biais d'un demi-mètre a été compensé avec succès.

rections peuvent être source de confusion lorsque l'on travaille avec des bursts en mode interférométrique IW, car les décalages géométriques dans les données ne sont généralement pas les mêmes aux limites des bursts. Cela peut introduire de petites incohérences dans un produit mosaïque s'il n'est pas correctement traité, ce qui est particulièrement gênant dans les applications de haute précision. Nous proposons une méthode pour prendre en compte les corrections précises de géolocalisation et de synchronisation en rééchantillonnant chaque burst de Sentinel-1 avant de l'assembler dans la mosaïque. La méthode est basée sur la géolocalisation d'un ensemble de points 3D échantillonnés à partir d'un modèle numérique d'élévation. Cela permet à la méthode de prendre en charge le calcul des décalages correctifs qui reposent non seulement sur les coordonnées de l'image, mais aussi sur les coordonnées géographiques 3D correspondantes. Les corrections sont utilisées dans l'estimation d'une matrice de rééchantillonnage affine par burst. Cette procédure peut être appliquée à une mosaïque primaire de Sentinel-1 pour une seule date. Elle peut également être utilisée sur des acquisitions secondaires pour obtenir une série temporelle recalée de mosaïques Sentinel-1 géométriquement précises. La méthode est validée par des expériences sur des données réelles de Sentinel-1, où nous montrons une amélioration dans l'alignement des chevauchements de bursts. En effet, la méthode corrige avec succès les décalages intra-pulse de l'ordre de 0,5 mètre entre les bursts consécutifs, comme le montre le Tableau 2.1.

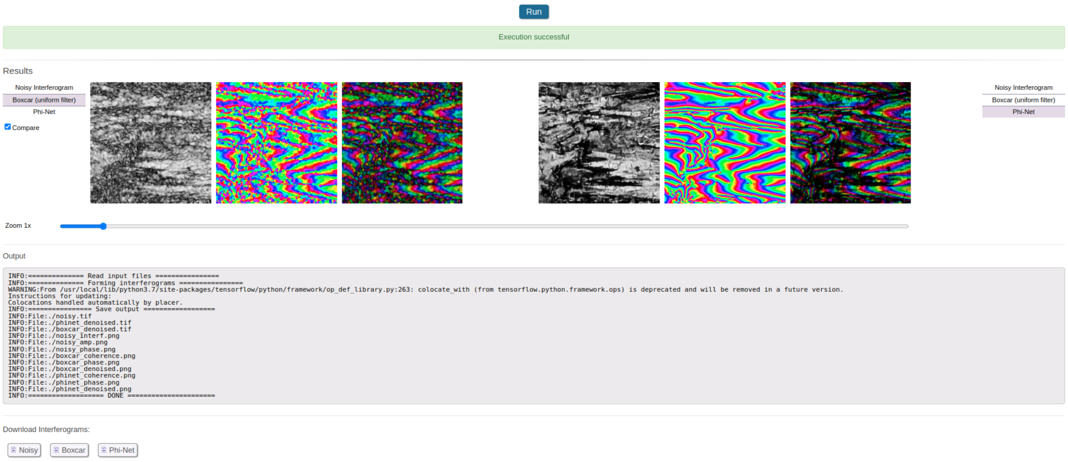

```
INFO:============== Read input files ================
INFO:============== Forming interferograms ================
WARNING:From /usr/local/lib/python3.7/site-packages/tensorflow/python/framework/op_def_library.py:263: colocate_with (from tensorflow.python.framework.ops) is deprecated and will be removed in a future version.
Instructions for updating:
Colocations handled automatically by placer.
INFO:================ Save output ==================
INFO:File:./noisy.tif
INFO:File:./phinet_denoised.tif
INFO:File:./boxcar_denoised.tif
INFO:File:./noisy_interf.png
INFO:File:./noisy_amp.png
INFO:File:./noisy_phase.png
INFO:File:./boxcar_coherence.png
INFO:File:./boxcar_phase.png
INFO:File:./boxcar_denoised.png
INFO:File:./phinet_coherence.png
INFO:File:./phinet_phase.png
INFO:File:./phinet_denoised.png
INFO:=================== DONE =====================
```

Figure 2.6 : La démo développée sur le réseau Φ-Net et utilisée pour les expériences du Chapitre 6. Nous pouvons voir la cohérence, la phase débruitée et la représentation de l'image complexe pour le filtre boxcar (à gauche) et le réseau Φ-Net (à droite).

### Chapitre 6 : Réseau de débruitage de phase et d'estimation de cohérence

Ce chapitre examine les performances combinées de débruitage et d'estimation de la cohérence du réseau connu sous le nom de Φ-Net (Sica et al. 2021). Nous examinons brièvement la méthode, l'architecture du réseau, les données d'entraînement et la stratégie. Ensuite, dans la section expérimentale, nous comparons les performances du réseau à celles du simple filtre uniforme boxcar sur des interférogrammes réels de Sentinel-1 contenant des franges topographiques et fournissons une démo en ligne pour reproduire les expériences, comme le montre la Figure 2.6. Nous vérifions les observations faites par les auteurs, en particulier en ce qui concerne la performance supérieure de débruitage et la préservation des détails fins dans l'estimation de la cohérence. De plus, nous remarquons un lien entre le filtre boxcar et Φ-Net lorsque nous comparons leurs résultats, en particulier dans les zones fortement affectées par le bruit. Nous supposons que cela s'explique naturellement en interprétant Φ-Net comme un réseau qui agit sur le résidu d'un filtre boxcar (avec enjambée, *stride*). Enfin, nous remarquons quelques discontinuités dans les franges de Φ-Net. Il est donc probable qu'une méthode d'apprentissage profond de bout en bout puisse apporter une légère amélioration à l'approche basée sur les patchs en augmentant le champ réceptif.

### Chapitre 7 : Réseau de déroulement de phase

Ce chapitre vise à expliquer et à évaluer la méthode de déroulement de phase proposée par Perera et al. dans [A joint convolutional and spatial quad-directional LSTM network for phase unwrapping, ICASSP 2021]. La méthode est basée sur l'apprentissage profond et a été récemment proposée pour résoudre le problème du déroulement de la phase. Nous fournissons une démo en ligne pour simuler des images de phase et les faire passer par le réseau. Les performances du réseau peuvent être testées visuellement et à l'aide de mesures telles que l'écart-type d'erreur, comme le montre la Figure 2.7. La simulation peut fournir des données hors distribution, en particulier avec l'ajout du signal atmosphérique spécifique à la phase InSAR. Nous observons dans nos expériences que la performance du réseau est adéquate sur les données du domaine, avec une certaine détérioration sur les données hors domaine. L'erreur résultante est structurée et peut contenir des bandes, des textures et des pics sous-estimés. Enfin, nous nous penchons sur le fait que le réseau exécute mutuellement les tâches de débruitage et de déroulement de phase. Nous proposons de séparer les deux tâches et de limiter la responsabilité du réseau au déroulement de phase, ce qui simplifierait la procédure d'évaluation.

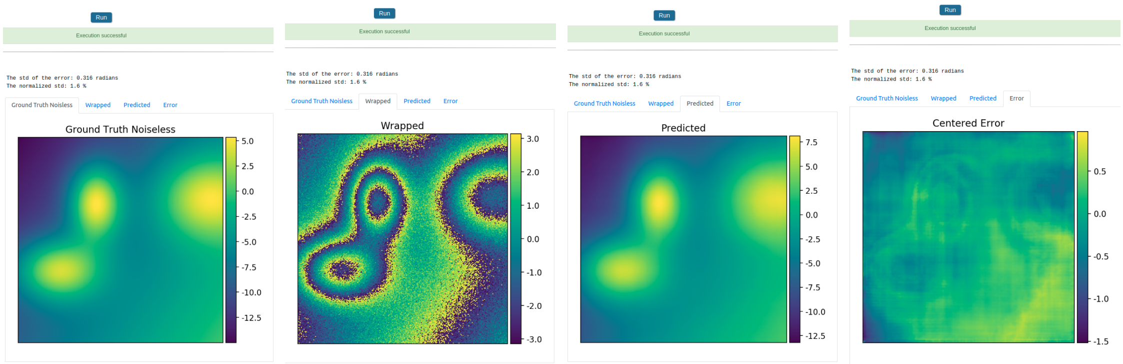

```
The std of the error: 0.316 radians
The normalized std: 1.6 %
```

```
The std of the error: 0.316 radians
The normalized std: 1.6 %
```

```
The std of the error: 0.316 radians
The normalized std: 1.6 %
```

```
The std of the error: 0.316 radians
The normalized std: 1.6 %
```

Figure 2.7 : La sortie de la démo du réseau de déroulement de phase examinée au Chapitre 7. Les mesures sont affichées au-dessus d'un ensemble d'onglets. Quatre onglets sont disponibles pour la vérité de terrain, la phase bruitée enroulée, l'image déroulée prédite avec le réseau et l'image d'erreur.

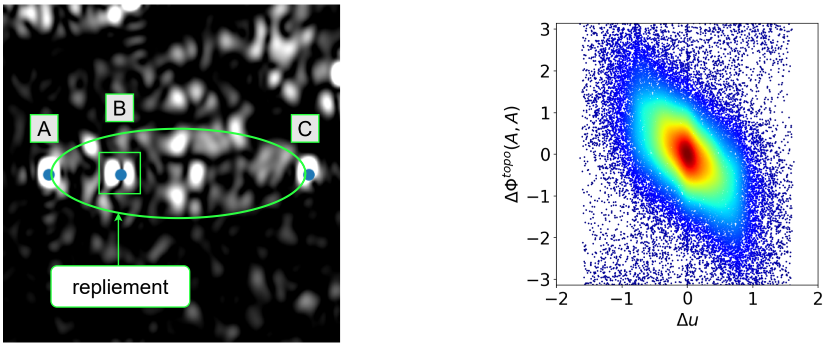

FIGURE 2.8 : Résultats du Chapitre 8. À gauche, nous voyons une image zoomée d'une cuve de stockage, avec les trois coins brillants vus dans Sentinel-1 : le toit fixe (A), la base fixe (B), le toit flottant (C). En raison de l'effet de repliement, les mesures InSAR sur (B) sont plus bruitées que sur (A). A droite, le nuage de points montre une tendance reliant la double différence de phase sur les toits des cuves voisines (A) à la double différence du taux de remplissage des cuves.

**Chapitre 8 : InSAR sur les cuves de stockage de pétrole brut**
Ce chapitre examine la possibilité d'utiliser la phase interférométrique sur certains coins fixes de cuves de stockage pour déduire le taux de remplissage des cuves. Pour cette étude, nous utilisons les données Sentinel-1 sur un site de cuves à toit flottant pour lesquelles le taux de remplissage peut être déduit de la position du toit flottant. Nous observons une corrélation entre la double différence de phase prise au niveau du toit fixe des cuves voisines et la double différence du taux de remplissage, comme le montre la Figure 2.8. La tendance suggère que lorsqu'une cuve se remplit, le coin du toit fixe subit une déformation d'environ 1 cm par rapport au satellite. Nous mettons en évidence la présence d'effets topographiques non compensés et de tendances temporelles lentes. Nous montrons également la relation entre le niveau de bruit dans les diagrammes de nuages de points et la dispersion de l'amplitude des réflecteurs. Nous interprétons également les diagrammes de nuages points de mauvaise qualité obtenus au niveau du réflecteur à base fixe comme étant le résultat de l'effet repliement du toit flottant. Les défis énumérés ci-dessus nécessitent des recherches plus approfondies et le développement de techniques InSAR adaptées.

## 2.4 Résumé des contributions

Cette thèse revisite le pipeline InSAR de Sentinel-1, avec l'objectif de clarifier certains concepts et d'améliorer la précision d'autres. Ce travail a également contribué au développement d'une chaîne de traitement InSAR à Kayrros, implémentée dans un package Python appelé EOS-SAR.

La première partie de la thèse présente différentes contributions menant à la construction de mosaïques Sentinel-1 précises. Dans le Chapitre 3, nous étudions le deramping des bursts de Sentinel-1, une étape nécessaire avant le rééchantillonnage. Nous comparons le deramping conventionnel prescrit par l'ESA avec celui implémenté dans le logiciel NSBAS et montrons l'analogie entre les deux. Ceci nous amène à proposer une approche de deramping qui réalise un compromis entre la précision et le calcul (mesuré en nombre d'opérations de de/re-ramping). Ensuite, dans le Chapitre 4, nous fournissons une implémentation open-source d'une méthode d'estimation de modèle de caméra RPC utilisant un algorithme itératif d'optimisation par moindres carrés pondérés et régularisés. Nous validons que les RPC ajustés à partir du modèle physique du capteur de Sentinel-1 ont des erreurs de l'ordre de $10^{-4}$ pixels en termes de RMSE. Enfin, dans le Chapitre 5, nous présentons une méthode permettant d'obtenir une série temporelle de mosaïques de bursts de Sentinel-1 géométriquement précises. Les matrices de rééchantillonnage sont estimées pour chaque burst à partir de la géolocalisation de points 3D échantillonnés à partir d'un MNE, tout en tenant compte de décalages correctifs précis. Ces décalages sont détaillés dans la littérature sur la précision de la géolocalisation de Sentinel-1.

La partie suivante de la thèse contient une contribution secondaire qui est une évaluation brève des applications de l'apprentissage profond à InSAR. Dans cette partie, nous fournissons principalement des études d'évaluation et des démos en ligne que l'utilisateur peut essayer, et nous ne ré-entraînons pas ou ne construisons pas les modèles nous-mêmes. Notre principale conclusion est que les réseaux ont des performances prometteuses pour des tâches telles que le débruitage de phase, l'estimation de la cohérence et le déroulement de phase. Dans le Chapitre 6, nous validons les performances satisfaisantes du réseau Φ-Net en matière de débruitage et d'estimation de la cohérence et nous établissons une analogie avec le filtre boxcar. Nous suggérons également de remplacer la décomposition de patch dans cette méthode par une approche d'apprentissage profond de bout en bout qui pourrait améliorer l'estimation des franges à grande échelle. Pour le déroulement de la phase dans le Chapitre 7, nous suggérons de séparer les tâches de déroulement et de débruitage au lieu d'entraîner le réseau à faire les deux en même temps.

La dernière partie de la thèse au Chapitre 8 montre le potentiel de l'InSAR pour la mesure du volume de pétrole brut à partir de la déformation des cuves de stockage. Outre la nouveauté de cette application, elle apporte également une petite contribution à l'interférométrie localisée. En effet, avec l'utilisation d'une simple double différence de phase entre des réflecteurs voisins, nous montrons la possibilité d'extraire des informations significatives des interférogrammes Sentinel-1 sur des actifs spécifiques.

Il est utile à ce stade de résumer la manière dont chaque contribution est utilisée ou peut être utilisée dans une chaîne de traitement. Tout d'abord, dans EOS-SAR, nous avons choisi de mettre en œuvre la méthode de deramping standard de l'ESA. En effet, dans une chaîne interférométrique complète, le gain de vitesse que nous obtenons en évitant quelques opérations de deramping n'ai potentiellement pas suffisant pour justifier le risque d'induire des erreurs de traitement. Néanmoins, notre étude comparative au Chapitre 3 a été essentielle pour comprendre les subtilités du deramping et faire un choix en fonction des compromis énumérés.

Ensuite, pour l'estimation des fonctions RPC, nous distribuons rpcfit en tant que package open-source qui fournit des coefficients ajustés à partir de grilles de points en utilisant l'algorithme expliqué dans le Chapitre 4. Nous avons l'intention de valider le gain potentiel d'efficacité que nous pourrions obtenir en utilisant des RPC pour des opérations telles que le backgeocoding (transformation de quantités de coordonnées géographiques en coordonnées radar à l'aide d'un MNE) ou le géocoding (l'opération inverse, également connue sous le nom d'orthorectification) ou le recalage géométrique comme dans le Chapitre 5. Ces opérations sont essentielles pour combiner des sources de données acquises par différents capteurs avec le SAR (images optiques, données météorologiques, données GPS...). L'utilisation des RPC est une alternative simple aux modèles de caméra et devrait être plus efficace en termes de calcul. Nous encourageons les fournisseurs d'images SAR à inclure les RPC dans leurs métadonnées à l'avenir. En outre, cet outil a été utilisé par d'autres membres de l'équipe pour ajuster les modèles de caméra dans l'imagerie optique dans [MdFML+21, MEA+22].

Quant à la méthodologie de rééchantillonnage et d'assemblage de bursts précise pour le recalage géométrique de Sentinel-1 présentée au Chapitre 5, elle a été intégrée dans le package EOS-SAR où elle est appliquée de manière systématique. Cette question de l'utilisation de corrections fines pour obtenir un recalage précis sur une grille commune gagne en importance avec la sortie prochaine du produit ETAD [GLM+22]. De même, le prochain produit SLC coregistré OPERA [FBJ+23] devrait également utiliser des corrections de type ETAD pour réaliser l'alignement fin.

Pour les réseaux de Deep Learning présentés dans les Chapitres 6 et 7, nous avons vu que leurs résultats sont encourageants, mais nous ne les utilisons pas systématiquement pour l'instant, même s'ils sont bien adaptés à des méthodes comme la technique SBAS brièvement mentionnée dans la Section 2.2.6. Pour le débruitage et l'estimation de la cohérence, l'apprentissage profond semble bien adapté pour résoudre ce problème, et les résultats du Φ-Net sont déjà intéressants pour générer et/ou améliorer les tâches en aval. En ce qui concerne le réseau de déroulement de phase, comme cette opération est risquée et peut induire de grandes erreurs, nous ne pouvons pas recommander l'utilisation du réseau pour des applications précises. Nous espérons voir à l'avenir davantage de problèmes InSAR résolus à l'aide de l'apprentissage automatique.

Enfin, pour l'application des cuves de stockage de pétrole brut, nous montrons que l'utilisation de la double différence de phase peut mettre en évidence le phénomène de déformation atypique et complexe. Nous avons l'intention de continuer à explorer d'autres sites et de développer un schéma de traitement adapté.

## 2.5 Liste des publications

### Présenté dans cette thèse

- Roland Akiki, Raphaël Grandin, Carlo de Franchis, Gabriele Facciolo, and Jean Michel Morel. A Comparative Study of Deramping Techniques for Sentinel-1 Tops in the Context of Interferometry. In *International Geoscience and Remote Sensing Symposium (IGARSS)*, pages 3372–3375. IEEE, 2021
- Roland Akiki, Roger Marí, Carlo de Franchis, Jean Michel Morel, and Gabriele Facciolo. Robust Rational Polynomial Camera Modelling for Sar and Pushbroom Imaging. In *International Geoscience and Remote Sensing Symposium (IGARSS)*, pages 7908–7911. IEEE, 2021
- Roland Akiki, Jeremy Anger, Carlo De Franchis, Gabriele Facciolo, Jean Michel Morel, and Raphael Grandin. Improved Sentinel-1 IW Burst Stitching Through Geolocation Error Correction Considerations. In *International Geoscience and Remote Sensing Symposium (IGARSS)*, pages 3404–3407. IEEE, 2022
- Roland Akiki, Jérémy Anger, Carlo de Franchis, Gabriele Facciolo, Jean-Michel Morel, and Raphaël Grandin. A brief evaluation of InSAR phase denoising and coherence estimation with Φ -Net. *Image Processing On Line*, submitted paper
- Roland Akiki, Carlo de Franchis, Gabriele Facciolo, Jean-Michel Morel, and Raphaël Grandin. Phase Unwrapping using a Joint CNN and SQD-LSTM Network. *Image Processing On Line*, 12:378–388, oct 2022

- Roland Akiki, Carlo de Franchis, Gabriele Facciolo, Raphaël Grandin, and Jean-Michel Morel. On The Potential Of Insar For Estimating Crude Oil Volume Changes From The Deformation Of Storage Tanks. In *International Geoscience and Remote Sensing Symposium (IGARSS)*, pages 7993–7996. IEEE, 2023

### Brevets soumis

- Roland Akiki, Jérémy Anger, Carlo de Franchis, Gabriele Facciolo, and Jean-Michel Morel. Method, device and storage medium for reconstructing a corrected mosaic image from burst images, submitted patent
- Roland Akiki, Carlo de Franchis, Gabriele Facciolo, Raphaël Grandin, and Jean-Michel Morel. Method, device and computer program for measuring a difference of fill ratio of a tank, submitted patent

### Logiciels libres et démos en ligne

- Logiciel d'estimation de RPC : rpcfit
- Démo du réseau de débruitage de phase et d'estimation de cohérence ici
- Démo du réseau de déroulement de phase ici
- EOS-SAR : Logiciel pour le pipeline de traitement SAR et InSAR. L'accès peut être accordé aux collaborateurs connus de la communauté des chercheurs. Parmi les fonctions prises en charge, citons le recalage des séries temporelles et l'assemblage des bursts SLC de Sentinel-1, la simulation des franges orbitales et topographiques, le débruitage de phase avec le filtre uniforme ou le filtre Goldstein [GW98], le déroulement de phase avec la méthode du flux de coût minimum [Cos98]. Une autre caractéristique intéressante est la possibilité de réaliser des mosaïques sur de petites zones d'intérêt sans avoir à traiter les données de l'ensemble du burst.

### Autres

- présentation orale au séminaire MDIS-2022 intitulée : "Improved Sentinel-1 IW Burst Stitching through geolocation error correction considerations" (Amélioration de l'assemblage des bursts de Sentinel-1 IW grâce à la correction des erreurs de géolocalisation).
- Poster à l'atelier FRINGE 2023 intitulé : "Measuring The Deformation Of Crude Oil Storage Tanks With Interferometry" (Mesure de la déformation des cuves de stockage de pétrole brut à l'aide de l'interférométrie)

# Part I

# Precise coregistration and geometric modeling

# 3 Comparison of Sentinel-1 TOPS deramping techniques

In this chapter, we compare the different spectral centering methods (referred to as deramping) for the Sentinel-1 images acquired with the TOPSAR mode, in the context of interferometry. Deramping is a necessary step that centers the frequencies in the Fourier domain around 0 Hz, prior to image interpolation. We show the analogy between two approaches in the literature, the conventional deramping function prescribed by ESA and the one implemented in the NSBAS software. We show that the NSBAS deramping function might induce a small quadratic phase ramp error in the interferometric phase along the azimuth. We propose a deramping method that does not suffer from this imprecision. We validate with experiments on real Sentinel-1 data that the error that reaches 0.12 rad on the burst boundaries with the NSBAS deramping is not present in our method. However, both the proposed and the NSBAS deramping methods only approximately re-center the spectrum, meaning that a small residual spectral shift remains. We derive a closed-form expression for the expected residual shift and show that the residual shift is typically small on a Sentinel-1 dataset (less than 35 Hz). We also verify that interpolating the images containing this residual spectral shift should not induce considerable drops in interferometric coherence. The proposed deramping method is only advantageous when co-registering a time series of N secondary SAR images onto a primary image. In this case, N + 1 deramping operations are needed with the proposed method, in contrast with the 2 * N de/re-ramping operations with the conventional approach.

## 3.1 Introduction

SAR (synthetic aperture radar) images have become an important data source in the remote sensing community, especially because images are acquired independently of the time of day and the weather conditions. Their usefulness has increased especially with the emergence of some advanced applications like interferometry.

For convenience, we repeat Equation 1.14 from Section 1.2.2 for interferometry

$$\Gamma_{12} = \Gamma_1 \times \Gamma_2^* = A_1 A_2 \exp\{j\,(\Phi_1 - \Phi_2)\}, \tag{3.1}$$

where $\Gamma_{12}$ is the interferogram formed between the two SAR images $\Gamma_1$ and $\Gamma_2$. The phase of the interferogram contains valuable information about the change in time of flight from the ground scatterers to the sensor on the satellite platform and can be used to measure their deformation between the two dates. Therefore, improving our ability to generate interferograms is a subject of great interest.

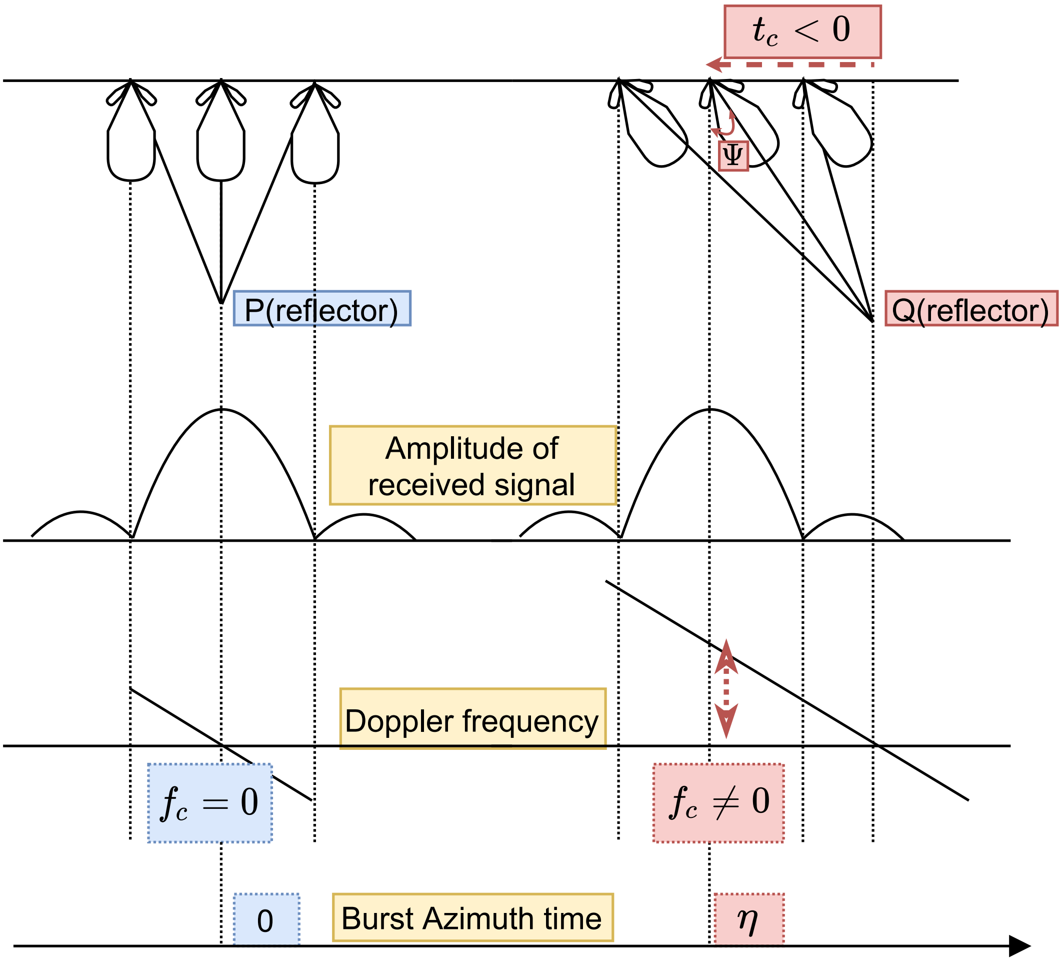

Figure 3.1: Downward view of the slant range plane during a TOPSAR burst acquisition. On the left, in blue, the antenna beam is orthogonal to the trajectory (near the middle of the burst). The Doppler frequency at the point of maximum amplitude is 0 Hz. On the right, in red, at azimuth time $\eta$, the beam has a squint angle $\Psi$ w.r.t. the zero Doppler plane. The point of max amplitude is reached earlier, and the Doppler frequency at this position is not null and is proportional to the radial velocity component (projection on line of sight)

In interferometric processing, the secondary image $\Gamma_2$ is resampled in order for it to be aligned with the primary image $\Gamma_1$. Resampling complex data requires cautious handling due to the possibility that the Fourier domain spectrum might not be centered around the 0 Hz frequency. For SAR images, as seen in Section 1.2.1, a frequency shift in azimuth (Doppler frequency) is usually present and might also induce aliasing. Certain operations, such as resampling or spectral shift filtering, necessitate realigning frequencies around 0 Hz and counteracting frequency shifts through a procedure referred to as deramping or demodulation [YMPIG+16]. In this chapter, we examine the deramping operation for Sentinel-1.

We focus on Sentinel-1's Interferometric Wide (IW) swath mode since it is the preferred and predominant acquisition mode for interferometry with this satellite. As seen in Figure 1.1, using the TOPSAR (Terrain Observation with Progressive Scans SAR) technique, the antenna beam is steered "instantly" in the elevation (range) direction in order to observe a series of subswaths. In each subswath, and in each cycle, a succession of pulses are emitted to record a burst. During the burst acquisition, the antenna beam is steered "continuously" in the azimuth direction with a steering rate of $k_\Psi$ as seen in Figure 3.1. This introduces a linear squint $\Psi$ with azimuth time $\eta$. The steering of the antenna beam will of course modify the Doppler properties of the signal. For example, in Figure 3.1, the Doppler frequency of point Q is linearly dependent on $\eta$ and $f_c(\eta) \neq 0$ since $\Psi(\eta) \neq 0$. This phenomenon thus induces a linear frequency shift with the azimuth time in the spectrum of the focused data.

As previously mentioned, interferometry often requires the co-registration of a set of secondary acquisitions with a primary acquisition. However, special care should be taken when resampling this complex signal that has a linearly shifted spectrum. A deramping correction needs to be applied prior to interpolation.

The main contributions of this chapter are:

- Detailing the mathematical equations of a deramping method [Gra15], and showing the analogy with another method of the literature [YMPIG+16];
- Showing the pros and cons of each deramping method, and proposing our own modifications.

## 3.2 Related work

Deramping is extensively explained in the ESA (European Space Agency) guidelines [Mir15], where the reader is provided with the necessary tools to perform the deramping and the demodulation operations from Sentinel-1 metadata. First, define $\eta$ as the azimuth time referenced to the center of the burst, $\tau$ as the range time and $k_t(\tau)$ as the Doppler rate in the focused data

$$k_t(\tau) = \frac{k_a(\tau)k_s}{k_a(\tau) - k_s} = \frac{k_s}{\alpha(\tau)}, \quad \alpha(\tau) = 1 - \frac{k_s}{k_a(\tau)}, \tag{3.2}$$

where $k_a(\tau)$ is the classical azimuth FM rate. $k_s$ is the Doppler rate induced by the steering of the beam

$$k_s \approx \frac{2v_s}{\lambda} k_\psi, \tag{3.3}$$

where $v_s$ is the satellite velocity and $\lambda$ the carrier wavelength and $k_\psi$ the rate of rotation in rad/s.

We also need to define $\eta_{ref}(\tau) = \eta_c(\tau) - \eta_c\left(\frac{Ns_{\text{swath}}}{2}\right)$ as the azimuth reference time,where $Ns_{\text{swath}}$ is the time corresponding to the number of samples in range and $\eta_c(\tau) = -\frac{f_{\eta_c}(\tau)}{k_a(\tau)}$ with $f_{\eta_c}(\tau)$ the mean Doppler centroid frequency over the burst. $f_{\eta_c}(\tau)$ and $k_a(\tau)$ are given as polynomials w.r.t $\tau$ in the metadata.

The deramping function is finally defined as the multiplication of the data, burst by burst, with

$$\phi(\eta,\tau) = \exp\left(-j\pi k_t(\tau)\left(\eta - \eta_{ref}(\tau)\right)^2\right). \tag{3.4}$$

After the deramping operation is performed, the spectrum will still be shifted by $f_{\eta_c}(\tau)$. Therefore, a demodulation operation is needed to shift the spectrum to baseband. If we wish to perform the demodulation with the deramping, the updated spectral centering function is

$$\begin{aligned}\phi(\eta,\tau) = \exp(&-j\pi k_t(\tau)\left(\eta - \eta_{ref}(\tau)\right)^2\\ &- j2\pi f_{\eta_c}(\tau)\left(\eta - \eta_{ref}(\tau)\right)).\end{aligned} \tag{3.5}$$

Reramping/remodulation correspond to the application of the complex conjugate of the functions defined in Equations 3.4 or 3.5.

In [YMPIG$^+$16], a detailed study of the complete processing chain for Sentinel-1 interferogram formation is provided. The authors distinguish between two different options for the complex burst interpolation. One of the options consists in modulating the interpolation kernel with the Doppler shift. This option is not going to be considered for our study for the sake of simplicity, since it requires an implementation of interpolation kernels. The second option consists in applying the centering function of Equation 3.5. Then the data is resampled with a real valued kernel. The reramping function is also resampled before applying it, i.e. if $T$ is the forward transform such that $(\eta', \tau') = T(\eta,\tau)$ , then for every position in the new grid $(\eta', \tau')$, the original position $(\eta,\tau) = T^{-1}(\eta', \tau')$ is estimated and inserted in the complex conjugate of Equation 3.5. The need for deramping is justified by the fact that a real-valued interpolation kernel acts as a low-pass filter. Therefore, it is necessary to bring the signal to baseband before applying the real-valued kernel. The need for reramping is justified by the fact that deramping is an operation that is performed to re-center the spectrum prior to interpolation, but it biases the interferometric phase, and should therefore be compensated. Indeed, interferometry is performed with the two SAR images in their original frequency band, provided that the coregistration error between the two images is sufficiently small.

The study conducted in [Gra15] shows that it is possible to apply an appropriate deramping function on a secondary acquisition burst prior to resampling and omit the step of reramping. This only works if a matching deramping function has also been applied in the primary acquisition. Note that this way of processing the data was also hinted for the TOMOSAR software [HNBM16]. This method is only relevant in the context of interferometry. Since this method is the one implemented in the interferometric NSBAS software, we were able to carefully reexamine the equations of [Gra15]. The details of this method, along with our own modifications are reported in the next section.

## 3.3 Deramping methods and proposed improvements

For the sake of simplicity, we denote the method exposed in [Mir15] and [YMPIG$^+$16] as "EsaDeramping", the one of [Gra15] as "NsbasDeramping". First, we will present

"NsbasDeramping", then we will introduce some modifications, that we will refer to in the following sections by "Ours". As mentioned previously, "NsbasDeramping" is specific for interferometry. Suppose we have a primary acquisition on which N secondary acquisitions need to be coregistered. Even though the primary burst will not be resampled, the essence of the method lies in multiplying it with the deramping function defined as

$$\phi(\eta^{(p)}, \tau^{(p)}) = \exp\left(-j\pi\, k_t^{(p)}(\tau^{(p)})\, \left(\eta^{(p)}\right)^2\right), \tag{3.6}$$

where the superscript $^{(p)}$ stands for primary.

Then, for the corresponding burst in a secondary acquisition, the deramping function applied should be matched to the deramping value of the primary, i.e. the same ground feature at coordinates $(\eta^{(p)}, \tau^{(p)})$ and $(\eta^{(s)}, \tau^{(s)})$ for the primary and secondary bursts respectively should have the same deramping factor applied. Recall that $\eta$ is referenced to the burst middle time and is defined in

$$\eta^{(p)} = t_0^{(p)} + \frac{y_R^{(p)}}{PRF} - t_{start}^{(p)} - \frac{lpb - 1}{2PRF}, \tag{3.7}$$

for the primary acquisition, where $t_0^{(p)}$ refers to the azimuth time of the first line in the image, $y_R^{(p)}$ is the azimuth coordinate of the reflector, $PRF$ is the pulse repetition frequency and $t_{start}^{(p)}$ is the time of the first line in the burst and $lpb$ is the number of lines per burst. The same equation is valid for the secondary acquisition.

It is then possible to estimate the lag in azimuth time $\eta$ between the location of the ground feature in the secondary and the primary burst as

$$\eta_{lag} = \eta^{(s)} - \eta^{(p)} = \eta_{off} + \eta_{shift}, \tag{3.8}$$

where

$$\eta_{off} = \frac{y_R^{(s)} - y_R^{(p)}}{PRF}$$

is computed from the transform of the registration and

$$\eta_{shift} = t_0^{(s)} - t_0^{(p)} - (t_{start}^{(s)} - t_{start}^{(p)})$$

is computed from the timing information in the metadata. We can also proceed in the same manner for the range time

$$\tau^{(p)} = \frac{x_R^{(p)}}{F_r} + \tau_0^{(p)},$$

where $x_R^{(p)}$ is the range coordinate of the reflector in the primary burst, $F_r$ is the range sampling frequency, $\tau_0^{(p)}$ is the time of the first range sample in the image. $\tau^{(s)}$ has the same equation as $\tau^{(p)}$. Thus we can find, $\partial\tau = \tau^{(s)} - \tau^{(p)}$. Using a simple approximation for $k_a \approx \frac{-2v_{eff}^2}{\lambda R}$, where $R = \frac{c\tau}{2}$ is the range expressed in (m) and $c$ the light speed in (m/s), and $v_{eff}$ is the effective velocity defined from $k_a$, we combine with Equation 3.2 and 3.3 and get

$$\alpha = 1 + \frac{vs}{v_{eff}^2} k_\Psi R \approx 1 + \frac{k_\Psi R}{v_{eff}},$$

$$\partial k_t = -\frac{k_s \partial \alpha}{\alpha^2} = -\frac{k_s k_\Psi c \partial \tau}{2v_{eff}\left(1 + \frac{k_\Psi R}{v_{eff}}\right)^2} \quad . \tag{3.9}$$

Finally, using $\partial k_t = k_t^{(s)}(\tau^{(s)}) - k_t^{(p)}(\tau^{(p)})$, the deramping function that multiplies the secondary acquisition at $(\eta^{(s)}, \tau^{(s)})$ is defined by

$$\begin{aligned}\phi(\eta^{(s)}, \tau^{(s)}) = \exp\{-j\pi &\left(k_t^{(s)}(\tau^{(s)}) - \partial k_t\right) \\ &\cdot \left(\eta^{(s)} - \eta_{lag}\right)^2\}\,.\end{aligned} \tag{3.10}$$

Afterwards, the secondary acquisition burst can be resampled.

It is easy to see how a clear analogy can be made with the method "EsaDeramping" since the deramping function applied at the primary burst in Equation 3.6 acts similarly to the reramping step during the interferogram formation (because of the complex conjugation in Equation 3.1). In other words, "NsbasDeramping" is actually starting with the deramping on a regular grid in the primary burst coordinate system (the conjugate of the reramping function is applied). Then, this deramping function is "resampled" to the secondary burst coordinate system and applied. Finally, the secondary burst is resampled.

With this analogy, it is clear that we can improve the deramping applied to the secondary acquisition, especially the part related to $\partial k_t$. Instead of using (3.9), we can simply do the following: for each pixel in the secondary burst, use the registration's transform $T$ to obtain the subpixel position in the primary burst $(\eta^{(p)}, \tau^{(p)}) = T(\eta^{(s)}, \tau^{(s)})$ and plug these values in (3.6). This method will be henceforth called "Ours".

For "NsbasDeramping" and "Ours", If we have N secondary acquisitions, we perform the deramping once per image. Taking into account the deramping performed at the primary acquisition, we would have in total N + 1 deramping operations. Comparing with "EsaDeramping", for each secondary acquisition, we need to deramp and then reramp. Hence, we would have 2 * N de/re-ramping operations. The computational gain of "NsbasDeramping" and "Ours" comes mainly from the fact that there is a single deramping operation applied in the primary image that replaces all the rerampings of the secondary acquisitions.

Their disadvantage stems from the fact that the phase in the deramping applied to the secondary acquisition in (3.10) is different from the one specified in (3.5) by

$$\begin{aligned}\Delta\Phi = &-\pi k_t(\tau)\left(\eta_{ref}(\tau) - \eta_{lag}\right)\left(2\eta - \eta_{lag} - \eta_{ref}(\tau)\right) \\ &+ \pi \partial k_t \left(\eta - \eta_{lag}\right)^2 + 2\pi f_{\eta_c}(\tau)\left(\eta - \eta_{ref}(\tau)\right),\end{aligned} \tag{3.11}$$

where the superscript $^{(s)}$ has been dropped for simplicity. The burst spectrum in azimuth will not be exactly in baseband prior to resampling, and the shift will be equal to $f_{shift}$ as

$$\begin{aligned}f_{shift} = \frac{1}{2\pi}\frac{\partial \Delta\Phi}{\partial \eta} = &-k_t(\tau)\left(\eta_{ref}(\tau) - \eta_{lag}\right) \\ &+ \partial k_t\left(\eta - \eta_{lag}\right) + f_{\eta_c}(\tau)\,.\end{aligned} \tag{3.12}$$

## 3.4 Experiments: Error evaluation on resampled bursts

The dataset used in the experiments consists of 32 Sentinel-1 images acquired over Albania (18.82°E;41.02°N) from 20190803 to 20200205 on the $73^{rd}$ relative orbit. We set the first

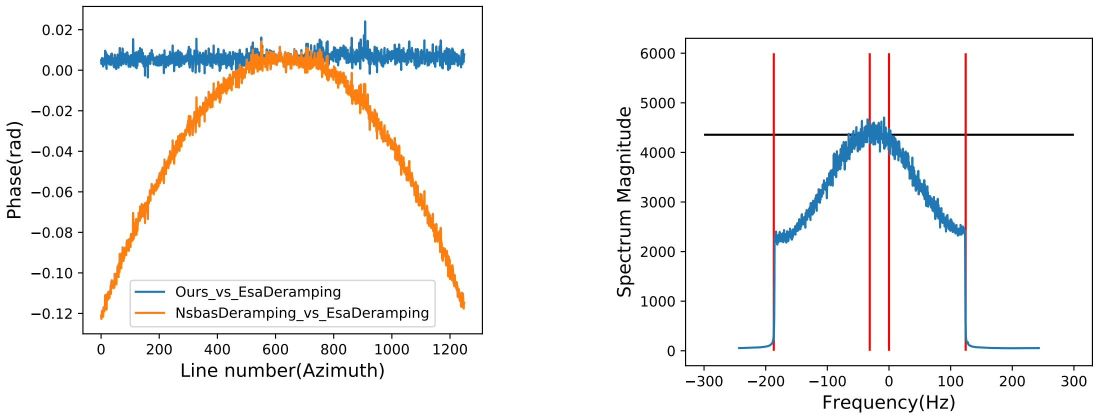

(a) The interferometric phase difference profile

(b) The spectral shift of "Ours"

Figure 3.2: The disadvantages of "NsbasDeramping" and "Ours". On the left, "NsbasDeramping" introduces a quadratic phase along the azimuth. On the right, both methods feature a spectral shift prior to resampling

image as the primary acquisition, and restricted the study on the second burst of the third subswath. The first test conducted consisted in taking the second image of the dataset as a secondary acquisition. The interferometric phase difference profile along the azimuth between "EsaDeramping", "NsbasDeramping", "Ours" is shown in Figure 3.2a. We can see that "NsbasDeramping" contains a quadratic phase ramp with respect to "EsaDeramping", that can reach perceptible values at the burst limits. "Ours" has the same phase content as "EsaDeramping" in the interferogram. Therefore, the quadratic ramp is attributed to a slight imprecision in (3.9). As for Figure 3.2b, the azimuth spectrum at a certain range in the secondary burst has been computed after the deramping of method "Ours". We can see that there is a spectral shift from the 0 frequency. We verified that the shift corresponds to (3.12). We also verified that because of the burst synchronization property of Sentinel-1, and of typical values of quantities in (3.12), we can simplify the formula to

$$f_{shift} = k_t(\tau)\eta_{lag} + f_{\eta_c}(\tau)\,. \tag{3.13}$$

We then predicted this spectral shift for all the bursts of the 31 secondary images in the dataset with (3.13) and the histogram is shown in Figure 3.3a. The maximal shift in absolute value is ≈ 35 Hz. Again, this is due to the Sentinel-1 timing properties, and we should be able to safely assume that the spectral shift will be small in general for any dataset.

We also performed a test where (3.5) is modified into

$$\begin{aligned}\phi(\eta,\tau,\eta_{delay}) = \exp\{&-j\pi k_t(\tau)(\eta-\eta_{ref}(\tau)\\ &-\eta_{delay})^2 - j2\pi f_{\eta_c}(\tau)\,(\eta-\eta_{ref}(\tau))\}\,,\end{aligned} \tag{3.14}$$

with $\eta_{delay}$ a delay introduced in the de/re-ramping function such that the spectrum would be shifted by $k_t\eta_{delay}$. Resampling is then performed with a cubic spline. We can hence assess the effect of resampling a spectrally shifted burst on the interferometric phase coherence. Figure 3.3b shows that the coherence doesn't drop until we reach high values of the spectral shift ($\approx 100Hz$). Therefore, since the typical spectral shifts that we obtain

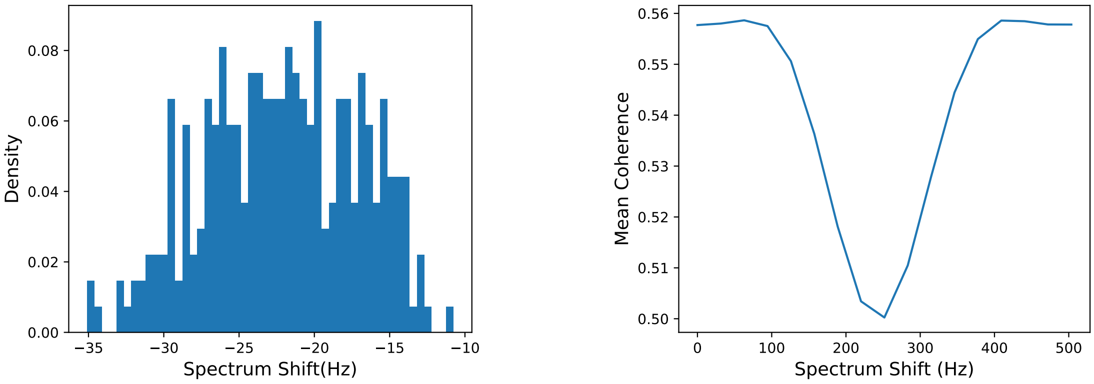

(a) Histogram of the distribution of the spectral shifts

(b) The interferometric coherence vs simulated spectral shift

Figure 3.3: The effect of spectral shift on the coherence. On the left, the distribution of the spectral shifts on the datastet. On the right, the degradation of the coherence after resampling the image with the spectral shift

with "Ours" should be small (for this dataset $\leq 35$ Hz), the resampling should not induce a coherence loss.

## 3.5 Conclusion

In conclusion, we have compared two deramping methods of the literature "EsaDeramping" [YMPIG+16] [Mir15] and "NsbasDeramping" [Gra15]. We introduced some improvements for the latter in "Ours". Those improvements were demonstrated experimentally on Sentinel-1 data. Nevertheless, the proposed method, like its predecessor in [Gra15], only centers the spectrum to a certain degree and a small spectral shift will remain. Experiments showed that Sentinel-1 timing properties should limit the value of the residual spectral shift. Interpolating the signal should not induce a loss of interferometric phase coherence. Future work should examine the spatial structure of the phase error w.r.t. the spectral shift. Further studies should look into the safety of using this method, especially the effect of changing the interpolation kernel on the phase errors introduced.

# 4 Robust RPC camera Modelling

The Rational Polynomial Coefficients (RPC) camera model can be used to describe a variety of image acquisition systems in remote sensing, notably optical and Synthetic Aperture Radar (SAR) sensors. RPC functions relate 3D to 2D coordinates and vice versa, regardless of physical sensor specificities, which has made them an essential tool to harness satellite images in a generic way. This chapter describes a terrain-independent algorithm to accurately derive an RPC model from a set of 3D-2D point correspondences based on a regularized least squares fit. The regularization parameter is set using an L-curve heuristic. The fitting algorithm is also iteratively weighted, i.e. the solution of an iteration is used to set the weight for the next iteration. The performance of the method is assessed by varying the number of point correspondences and the size of the area that they cover. We test the algorithm on Sentinel-1 SAR and WorldView-3 optical data, to derive RPCs from physical sensor models or from other RPC models after composition with corrective functions. We show that increasing the number of correspondences slightly reduces the RMSE. We also show that it is easier to fit the RPC function on a smaller surface area. For most configurations, the RPC fitted has errors on the order of $10^{-4}$ pixels in terms of RMSE on a validation grid of points, confirming the ability of the model to capture complex geolocation mappings.

## 4.1 Introduction

Developing a remote sensing application requires a set of tools, one of which is geolocation. Geolocation relates the 3D world coordinates to the 2D image. This is represented by means of a *projection* function $\mathcal{P} : \mathbb{R}^3 \rightarrow \mathbb{R}^2$, that maps 3D points to the image plane, and its inverse, the *localization* function $\mathcal{L} : \mathbb{R}^2 \times \mathbb{R} \rightarrow \mathbb{R}^3$. When all the physical phenomena and components involved in the acquisition process are known, the geolocation functions can be defined by a chain of operations that model such factors, in what is known as a *physical* or *rigorous* sensor model.

For optical satellite images, pushbroom scanners are the most common acquisition system, typically consisting of a single line of pixel sensors mounted on a platform that captures each line of the image at a different moment in time. As a result, the exterior orientation parameters, i.e. the perspective center and the attitude angles, change from line to line. The intrinsic parameters (e.g. pixel size, focal length, lens distortion), related to the physical design of the sensor, are constant across the image [Gro01]. A detailed description of a simplified physical sensor model for pushbroom scanners can be found in [dFMLGF15]. In the case of Synthetic Aperture Radar (SAR) images, the most used physical sensor model is the Range-Doppler model detailed in [Cur82]. SAR satellites send an electromagnetic wave that is reflected on the ground. The image is acquired line by line (similar to a pushbroom system), and the position of a ground patch in the image is related to its distance to the sensor, known as the *range*. The Range-Doppler model is constructed based on ephemeris data (time, position and velocity samples along the orbit) and the acquisition timing information. The ephemeris data needs to be interpolated to obtain continuous geolocation functions along the orbit. For more details on the SAR sensor model, refer to section 1.2.3.

Image providers (especially optical) have adopted the generic Rational Polynomial Coefficients (RPC) camera model to save customers from having to deal with the complex specificities of rigorous sensor models. The RPC model is independent of physical properties and offers flexibility to work with different coordinate systems. RPCs have become essential metadata to process satellite images in a generic way, from different sources and for multiple tasks, e.g. photogrammetry and radargrammetry based 3D reconstruction or image ortho-rectification and coregistration.

In this chapter, we describe a terrain-independent algorithm to fit an RPC model from a physical sensor model or any other geolocation model. Our contributions are:

- An open-source implementation of the method as an easy-to-use Python package, which is available at `https://github.com/centreborelli/rpcfit`.
- An evaluation of the algorithm's precision and robustness based on real scenarios. We test our method using Sentinel-1 and WorldView-3 images, to fit a SAR physical sensor model or correct an existing RPC model by composing it with a complementary transformation.

### 4.1.1 Mathematical formulation of the RPC model

The RPC model defines the projection function $\mathcal{P}$ as

$$r_n = \frac{a\left(X_n, Y_n, Z_n\right)}{b\left(X_n, Y_n, Z_n\right)} \quad c_n = \frac{e\left(X_n, Y_n, Z_n\right)}{f\left(X_n, Y_n, Z_n\right)}, \tag{4.1}$$

where $a, b, e, f$ are cubic polynomials. $X, Y, Z$ represent the longitude, latitude and height of a 3D point; and $r, c$ are the row and column of its projection on the image plane.

Equation 4.1 uses normalized coordinates for better numerical stability, hence the subscript $n$. Normalized values are in the range [-1, 1], and they are obtained using two scalars, an

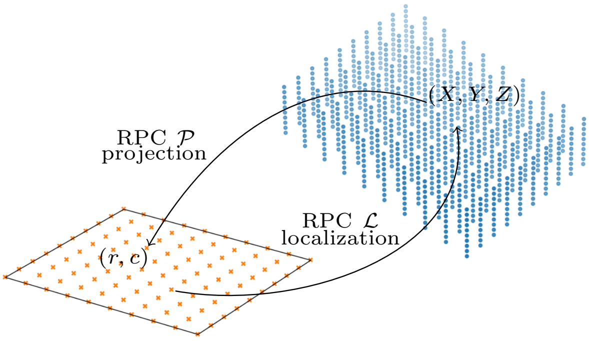

Figure 4.1: The RPC model is derived using a grid of 3D CNPs (Control Points) and its projection onto the satellite image.

offset and a scale factor: $X_n = (X - X_{\text{offset}})/X_{\text{scale}}$, where $X$ could be $r, c, X, Y$ or $Z$ from Equation 4.1.

Each RPC polynomial $p$ is defined by 20 coefficients as

$$\begin{aligned} p(X,Y,Z) = \ & p_0 + p_1 Z + p_2 Y + p_3 X + p_4 ZY + p_5 ZX \\ & + p_6 YX + p_7 X^2 + p_8 Y^2 + p_9 Z^2 + p_{10} ZYX \\ & + p_{11} Z^2 Y + p_{12} Z^2 X + p_{13} Y^2 Z + p_{14} Y^2 X \\ & + p_{15} ZX^2 + p_{16} YX^2 + p_{17} Z^3 + p_{18} Y^3 + p_{19} X^3, \end{aligned} \tag{4.2}$$

where $p_i$ is the $i$-th coefficient of $p$. Since we set $p_0 = 1$ for the RPC denominator polynomials, a total of 78 coefficients need to be determined to define $a$, $b$, $e$ and $f$ in Equation 4.1.

## 4.2 Related work

RPCs have been used for high-resolution optical satellite imaging since the launch of Ikonos in 1999 [Gro01, TH01, FDG06, LJH15]. In the last decade, they have been proven to be extremely accurate for SAR acquisition systems as well [ZFL+10, ZHB+11].

The RPC model of a satellite image can be constructed using a set of correspondences between image and object space coordinates. Depending on the nature of these correspondences, the literature can be classified into terrain-dependent or independent methods (or a combination of both). Terrain-dependent strategies use Ground Control Points (GCPs), whose object and image coordinates are known in advance, relying on manual labeling or on-site measurements. Oppositely, terrain-independent methods derive virtual sets of 2D-3D point correspondences from other geolocation functions, usually a physical sensor model. Once the point correspondences are available, least squares algorithms are typically used to estimate the RPC coefficients that minimize the error between the projected 3D points and their image locations.

Several works have underlined the importance of using uniformly distributed points in a sufficient amount, covering the different parts of the image and the whole altitude range of the scene [TH01, LJH15]. As a result, regularized least squares methods have become widely used to gain robustness to different configurations and enforce well-conditioned normal equations [TH01,LJH15,ZHB+11,WZS16]. Additionally, terrain-dependent strategies have explored the selection of optimal and balanced subsets of GCPs, e.g. [TH01] propose a bucketing strategy or [WZS16] study the benefits of encouraging correspondences located at building edges in urban scenarios. In contrast, terrain-independent methods can arbitrarily generate regular sets of points but require special care to the boundaries and density of the structure, e.g. [ZHB+11] investigate the impact of different numbers of elevation layers for flat and mountainous areas.

## 4.3 Method: Fitting the coefficients with an iterative optimization scheme

We follow a terrain-independent approach similar to [TH01] to fit an RPC model to another input geolocation model. The data used to fit the model consists of a 3D grid of uniformly distributed Control Points (CNPs) within some longitude, latitude and altitude boundaries (Fig. 4.1). The 2D image point of each CNP can be obtained by projecting it with the input geolocation model, so that each sample results in 5 normalized values, i.e. $(X_i, Y_i, Z_i, r_i, c_i)$. For simplicity, we drop the subscript $n$ of normalized coordinates and replace it by $i$ to refer to the sample index.

Using $N$ CNPs, Equation 4.1 can be rewritten as a system of equations, in matrix form, following the derivation of [TH01]:

$$WTI - WG = 0, \tag{4.3}$$

where

$$\begin{aligned}
W &= \text{diag}\left[\frac{1}{b(X_1,Y_1,Z_1)},\dots,\frac{1}{b(X_N,Y_N,Z_N)},\frac{1}{f(X_1,Y_1,Z_1)},\dots,\frac{1}{f(X_N,Y_N,Z_N)}\right]\\
T &= \text{block diag}\left[M_r, M_c\right] \quad M_r, M_c \in \mathbb{R}^{N\times 39}\\
i\text{-th row of } M_r &= \left[1, Z_i, Y_i, \dots, X_i^3, -r_iZ_i, -r_iY_i, \dots, -r_iX_i^3\right]\\
i\text{-th row of } M_c &= \left[1, Z_i, Y_i, \dots, X_i^3, -c_iZ_i, -c_iY_i, \dots, -c_iX_i^3\right],\\
I &= \left[a_0, \dots, a_{19}, b_1, \dots, b_{19}, e_0, \dots, e_{19}, f_1, \dots, f_{19}\right]^T,\\
G &= \left[r_0, \dots, r_N, c_0, \dots, c_N\right]^T.
\end{aligned}$$

In Equation 4.3, $W$ is a weight matrix with shape $2N \times 2N$, where $b(X_i, Y_i, Z_i)$ denotes the RPC polynomial $b$ evaluated with the 3D coordinates of the $i$-th CNP (similarly for $f(X_i, Y_i, Z_i)$); $T$ is the design matrix with shape $2N \times 78$; $I$ is the solution vector with the 78 RPC coefficients necessary to determine $a$, $b$, $e$ and $f$ in Equation 4.1; and $G$ is a vector of length $2N$ containing the CNPs image coordinates.

Equation 4.3 can be solved by least squares minimization to estimate $I$, using the normal equation

$$T^TW^2TI - T^TW^2G = 0. \tag{4.4}$$

To increase numerical stability, ridge estimation regularization [WZS16, ZHB+11] is often added so that the normal equation becomes

$$(T^TW^2T + h^2E)I - T^TW^2G = 0, \tag{4.5}$$

where $E$ is the identity matrix and $h$ is a scalar controlling the regularization that is applied. To choose the best regularization factor $h$, the L-curve criterion was introduced in [ZHB+11]. This heuristic computes the log norm of the solution ($\log \|I\|_h$) versus the log norm of the residual ($\log \|WTI - WG\|_h$) across different values of $h$ that extend from the minimal to the maximal singular value of T. This curve usually has an L-shape, in which the optimum corresponds to the maximum regularization parameter that achieves a small residual. The value corresponding to the corner of the curve, at the position of maximal curvature, is taken to set $h$ automatically. For non-weighted regularized least squares (i.e. weights are set to the identity, $W = E$), the L-curve criterion is fast since the curvature can be computed with closed-form expressions [HO93].

Therefore, we first set $W^{(0)} = E$ (where the superscript denotes the iteration number) and use the L-curve criterion to determine the optimal $h$ and an initial solution $I^{(0)}$. Then, for $i \geq 1$ , $W^{(i)}$ is determined from $I^{(i-1)}$ and is plugged in Equation 4.5 to solve for $I^{(i)}$ iteratively (the SVD least squares solver is used for stability). The iterations stop when the change in terms of RMSE between the RPC projected CNPs and their image coordinates becomes lower than a tolerance value. After convergence, some final ICCV (Iteration by Correcting Characteristic Value [ZHB+11]) iterations are computed to remove possible

| | **SAR dataset** | **Optical dataset** |
|---|---|---|
| platform | S1 A/B | WorldView-3 |
| number of images | 32 | 47 |
| geographic area<br>(lon, lat) center | Albania<br>(18.82,41.02) | Argentina<br>(-58.61,-34.47) |
| first acquisition date | 2019-08-03 | 2014-11-15 |
| last acquisition date | 2020-02-05 | 2016-01-13 |
| altitude range (m) | $[-533, 2969]$ | $[-513, 548]$ |

Table 4.1: SAR and optical data used in the experiments. The altitude range of the area covered by each collection of images is defined using the [min, max] values from the corresponding SRTM [FRC⁺07] digital elevation model ±500 m to consider tall buildings or fine irregularities beyond bare ground level.

biases introduced by the regularization. The same stopping criterion based on the RMSE improvement is used. Each ICCV iteration $k$ can be expressed as

$$(T^T(W^{(k)})^2T + E)I^{(k)} = T^T(W^{(k)})^2G + I^{(k-1)}. \tag{4.6}$$

## 4.4 Evaluation with SAR and optical imagery

### 4.4.1 Data and use cases description

Two datasets were used in the experiments:

- **SAR.** 32 Sentinel-1 SAR images (Table 4.1). The data is in Interferometric Wide Swath (IW) mode, each product contains 3 subswaths, and each subswath contains multiple bursts that need to be stitched together to get a continuous image. We construct the Range-Doppler physical sensor model and use the method from Section 4.3 to fit an equivalent RPC model for each image of the dataset.
- **Optical.** 47 WorldView-3 panchromatic images (Table 4.1), from the 2016 *IARPA Multi-View Stereo 3D Mapping Challenge* [BKHB16]. The original RPCs of the images exhibit small inaccuracies, mainly due to inexact knowledge of the satellite attitude angles, which cause a 3D point to be projected to non-corresponding pixels across different images. Bundle adjustment (BA) algorithms are a well-known approach to correct RPC errors [FDG06, BAM18, MDMLF19]. We apply a BA similar to [BAM18] to correct the projection function $\mathcal{P}$ of each RPC into a new $\mathcal{P}_{\text{BA}}$, expressed as

  $$\mathcal{P}_{\text{BA}}(X) = \mathcal{P}(R(X - T - C) + C), \tag{4.7}$$

  where $X$ is a 3D point. That is, each RPC is corrected by applying a translation $T$ followed by a rotation $R$ around an approximate camera center $C$, before applying the original projection $\mathcal{P}$. $C$ is derived by regressing a projective model from each RPC model. Our method from Section 4.3 is used to fit $\mathcal{P}_{\text{BA}}$ from the composition of $\mathcal{P}$ with $T, R, C$.

### 4.4.2 Performance assessment

To apply the method described in Section 4.3, the altitude limits of the grid of CNPs are set using the altitude ranges in Table 4.1. To assess the RPC fitting, we use a grid of Check

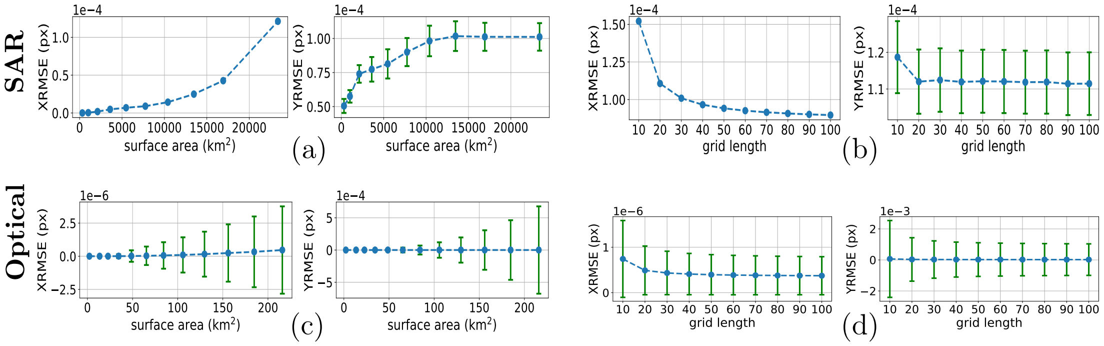

Figure 4.2: RPC fitting error varying grid length and surface area on the SAR (a-b) and optical data (c-d) described in Section 4.4.1. Each vertical bar corresponds to the $[-\sigma/2,\ \mu,\ \sigma/2]$ values of the root-mean-square error (RMSE) evaluated across the different images of the datasets, in each dimension of the image plane, where $\mu$ corresponds to the mean and $\sigma$ to the standard deviation.

Points (CKPs), which are located in the middle of each pair of consecutive CNPs. The evaluation metric is the RMSE measured in pixels. It is obtained by comparing the image coordinates of the projection of the CKPs with the output RPC and the input physical geolocation model. We set a tolerance of $10^{-10}$ for the stopping criterion based on the RMSE improvement on CNP grid, and a maximum of 20 iterations for the weighted least squares and the ICCV iterations.

Two types of experiments were conducted to assess the performance and robustness of the method:

- *Varying surface area.* For each image, we fit different RPCs by gradually increasing the longitude and latitude limits of the grid of CNPs from a small square centered at the image center to a larger square including the entire image. The number of CNPs is fixed, with $50 \times 50$ samples in the longitude and latitude dimensions and 10 elevation layers (25000 points in total).
- *Varying grid length.* For each image, we fit different RPCs, by increasing the number of CNPs in each elevation layer, i.e. $n \times n$ where $n$ is the *grid length*. The longitude and latitude boundaries of the grid are fixed using the equivalent limits of the image plane.

Overall, the results presented in Fig. 4.2 show that the RPCs constructed with our method approximate the geolocation models with very high accuracy for the two datasets and the two scenarios outlined in Section 4.4.1. The RMSE is in the order of $10^{-4}$ pixels or less in both dimensions of the image plane for the majority of configurations that were tested, which emphasizes the robustness of the method.

The experiments with different grid lengths (Fig. 4.2b and 4.2d) show that 10 samples in the longitude and latitude directions is already a good choice and increasing this number beyond 20 does not result in significant improvements. The experiments with varying surface area (Fig. 4.2a and 4.2c) show that both the overall RMSE values and its variation across the different images increase with the size of the area being fitted. This is probably due to the fact that the SAR physical sensor model is less smooth for large neighborhoods. A similar behavior is obtained with the optical dataset, where the original RPCs are known to behave locally as an affine camera [FDG06, MDMLF19].

## 4.5 Conclusion

This chapter described an automatic algorithm to fit the RPC model of a satellite image in a terrain-independent manner. The inputs of the method are a regular grid of 3D points (CNPs), with multiple elevation layers, and the 2D locations of the points on the image plane. We evaluated the method on real scenarios using collections of SAR and optical satellite images and assessed its performance by varying the CNPs' configuration. Finally, we release an open-source implementation of the algorithm as an easy-to-use Python package.

# 5 Sentinel-1 IW geolocation based burst stitching

Since the commissioning phase of Sentinel-1A, several calibration studies have improved the geolocation and geometric modeling of the data. The implementation of the corrections presented in these studies is left to the user. The issues found might be confusing when working with bursts in the interferometric wide swath mode because the geometric shifts in the data are not usually the same at the burst boundaries. This might introduce small inconsistencies in a mosaic product if not properly handled, which is especially inconvenient in high-precision applications. This chapter proposes a method to account for this effect by resampling the bursts before stitching. The method is based on a geolocation of a set of 3D points sampled from a Digital Elevation Model. This enables the method to support the computation of corrective shifts which not only rely on the image coordinates but also on their corresponding 3D geographic coordinates. The corrections are used in the fitting of an affine resampling matrix per burst. This procedure can be applied on a primary Sentinel-1 mosaic for a single date. It can also be used on secondary acquisitions to get a coregistered time series of geometrically precise Sentinel-1 mosaics. The method is validated with experiments on real Sentinel-1 data, where we show an improvement in the alignment of the burst overlaps. Indeed, the method successfully corrects intra-pulse shifts in the order of 0.5 meters in range between consecutive bursts.

## 5.1 Introduction

The Sentinel-1 (S1) mission has been undoubtedly attracting a lot of interest from the scientific community, spawning a growing number of applications. Some of these applications, like interferometry, sometimes focus on large-scale phenomena such as the measurement of ground deformation on the extent of a country. Other applications perform more localized measurements, e.g. in the case where specific sites need to be monitored. Depending on the application, a certain degree of geometric precision may be expected in the S1 image. Recent calibration studies have allowed the identification and modeling of geolocation errors for S1 [PRF+18, GSB+20]. However, the correction of these effects is left to the user since it is not activated by default in the S1 processor.

In this chapter, we will be addressing this issue. We will focus on S1 data acquired in the Interferometric Wide (IW) swath mode as seen in Figure 1.1, but the method also applies to the Extra Wide (EW) swath mode. The data is acquired in multiple swaths (3 for IW) along the range, each containing a set of bursts along the azimuth. The added difficulty of the IW mode to the processing is the need to mosaic the bursts into a continuous image. Then, the problem arises when burst-dependent shifts are present in the data, which would cause geometric discontinuities and inconsistencies at the burst boundaries in the mosaic. Our contributions are:

- Proposing a simple and generic resampling method for the correction of geometric errors in S1 bursts (IW mode) before the deburstING step. The correction is based on the geolocation of a set of points sampled from a digital elevation model (DEM). The geolocation has been explained in Section 1.2.3, and a fitted RPC model as shown in Chapter 4 could be used. For the resampling during coregistration, deramping should be applied as well from one of the methods exposed in Chapter 3.
- Validating the precision of the method using experiments on a real S1 dataset.

## 5.2 Related work

Many previous studies have presented the necessary steps for the correct processing of S1 bursts in IW mode. For example, the authors in [WWS+16] list some of the modifications needed to add the support for S1 IW in the GAMMA software. One aspect that is addressed is the combination of the data from individual bursts and subswaths into consistent mosaics. The suggested method is to cut the bursts in the overlap region and then simply concatenate them. This is indeed the intuitive way of dealing with the stitching of Sentinel-1 bursts since it is argued that the S1 mosaics are seamless radiometrically and geometrically in range and azimuth. Other articles follow the same logic to mosaic the burst interferograms, i.e. after the secondary burst has been resampled to the primary burst frame and the interferogram has been formed in the primary frame [YMPIG+16,MDZ+19]. In any case, the stitching in the primary frame is only dealt with as an operation of concatenating bursts while carefully handling the overlaps.

On the other hand, other studies tackle the problem of geolocation for Synthetic Aperture Radar (SAR) images, i.e. finding the image coordinate of a 3D point (referred to as projection or backward geocoding) or vice versa (localization or forward geocoding). For S1, it was shown [SS19] that a simple geolocation using the Range-Doppler (R-D) model with no additional correction would yield biases of the order of ∼3m in range and ∼2m in azimuth for IW mode. To correct these errors, many factors affecting the range and the azimuth arising from the SAR acquisition and processing chain need to be taken into account. The most important factor affecting the range is the Atmospheric Path Delay (APD). Other factors that help improve the accuracy of the geolocation are bistatic correction, instrument timing correction, topography-dependent Doppler centroid correction, intra-pulse motion correction...

Some of the previously mentioned corrections need to be applied at the burst level. This means that for the same target located in the overlap area between two bursts (at the burst boundary), the correction will be different in the upper burst from the lower burst. Therefore, the actual (corrected) position of a reflector in the overlap area is not the same between different bursts. To illustrate this concept, let us consider the intra-pulse motion correction [PRF+18, GSB+20]

$$\Delta\tau(f_{DC}) = \frac{f_{DC}}{K_r}. \tag{5.1}$$

This correction can be modeled as a removal of a range shift dependent on the Doppler centroid frequency as seen in Equation 5.1, where $\Delta\tau(f_{DC})$ is the two-way range time shift present in the data in seconds, $f_{DC}$ is the Doppler centroid (DC) in Hz and $K_r$ is the chirp rate in Hz/second. $K_r$ is constant on the swath, while $f_{DC}$ varies linearly inside a burst w.r.t. the azimuth time referenced to the middle of the burst. For IW mode, the range shift present in the data can therefore reach approximately -0.5 m at the start of the burst and increase linearly with azimuth time to reach +0.5 m at the end of the burst. Hence, a target with range $r_{target}$ located in the overlap area between burst i and burst i+1 will have a corrected actual range $r'_{target,i} \approx r_{target} - 0.5$ m in burst i and $r'_{target,i+1} \approx r_{target} + 0.5$ m in burst i+1. Therefore, the intra-pulse motion correction proves that there is a range shift up to ∼1 m at the boundary of the bursts. Considering that the range pixel spacing is ∼2.3 m, this shift is non-negligible for high-precision applications.

In [PRF+18], the authors acknowledge that these biases are confusing and need to be addressed. These corrections are not currently activated in the S1 processor to avoid incorrect phase patterns during interferogram formation with older data where the corrections are not applied. Instead, the computation of the various shifts should be simplified with the upcoming release of the Extended Timing Annotation Dataset (ETAD) product for Sentinel-1 [GLM+22]. The dissemination of ETAD products is planned for the end of 2023, but only for future S1 products (no historical data). The importance of considering these shifts is demonstrated in [GLM+22], where the use of ETAD to resample the Single Look Complex (SLC) S1 data showed an increase in precision in the subsequent offset tracking result.

On the other hand, during typical S1 processing, a geometric coregistration is performed using the geolocation of DEM points [YMPIG+16]. Therefore, this pipeline can be adapted with minimal changes to account for ETAD-like corrections computed during the geolocation operation. This chapter aims to show how these corrections can be applied and validate the results with experiments.

## 5.3 Method: Burst stitching with geolocation corrections

This section illustrates the method we propose to correct the difference in the shifts from one burst to another. Since some of the corrections are performed during the geolocation of a 3D point and cannot be performed based on the pixel position alone, the correction procedure will be based on geolocation. Our aim is to construct a mosaic of a set of S1 bursts for one image at a specific date. For example, one S1 IW product contains 3 swaths, each containing around 9 bursts. The bursts that need to be stitched can come from different swaths or the same swath. For simplicity, for the rest of the chapter, we assume that we are working on a set of consecutive bursts within a swath, as shown in Figure 5.1. The method can be defined as follows:

- For a set of bursts in a swath, define the burst limits (origin $\mathrm{B}_\mathrm{i}^{(\mathrm{p})}$ and size) from the metadata, then deduce the mosaic limits.
- Using the metadata, deduce the mosaic's geographic extent and download a Digital Elevation Model (DEM) covering it.
- For a set of points $\{\mathrm{Q}\}$ lying on the surface of the DEM, find the projected coordinates in the mosaic $\{\mathrm{Q}^{(\mathrm{p})}\}$.
- Use the burst cuts (red dashed lines in Figure 5.1) to find the appropriate burst id "i" for each projected point.
- Apply the corrections on each point $\mathrm{Q}^{(\mathrm{p})}$ to find $\hat{\mathrm{Q}}^{(\mathrm{p})}$. Some of the corrections might depend on the burst id "i", on the geometry (incidence angle, for example), and

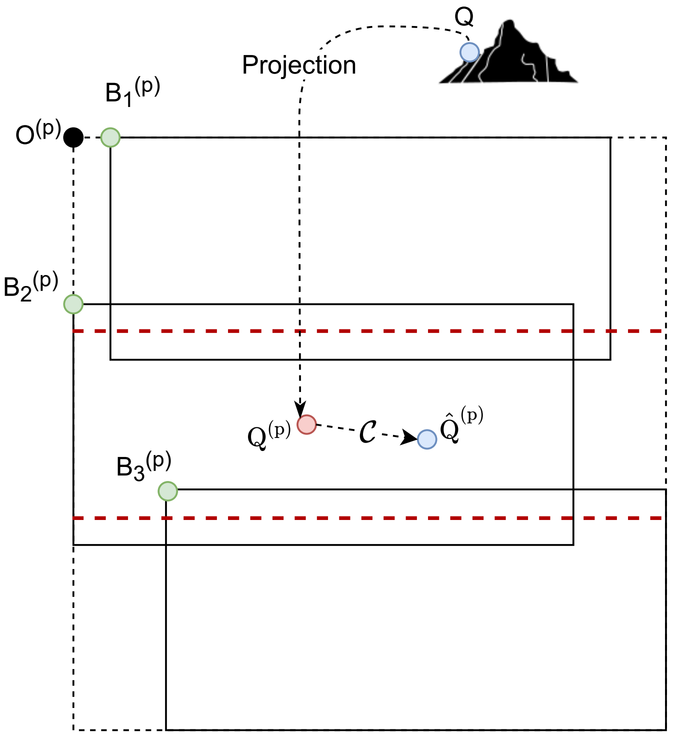

Figure 5.1: S1 IW mosaic consisting of many bursts. The mosaic (dashed boundary) can be defined as the minimal continuous image containing the valid parts of the bursts. Here only 3 bursts are shown in the mosaic. The bursts within the mosaic contain some overlap, i.e. some targets are acquired twice by consecutive bursts. The horizontal cuts (dashed red lines) are defined in the overlap region to guide the stitching strategy. $\mathrm{O}^{(\mathrm{p})}$ is the mosaic origin. $\mathrm{B}_{\mathrm{i}}^{(\mathrm{p})}$ is the ith burst origin. Q is a 3D point located on the surface of the DEM. $\mathrm{Q}^{(\mathrm{p})}$ is the R-D projection of Q and $\hat{\mathrm{Q}}^{(\mathrm{p})}$ is the corrected position of the target using the correction $\mathcal{C}$. The notation $^{(\mathrm{p})}$ indicates the primary image.

on other specific variables denoted as $\theta$. The correction $\mathcal{C}(\mathrm{Q}^{(\mathrm{p})}, \mathrm{i}, \theta)$ will simply be referred to as $\mathcal{C}$.

- Use the set of points $(\{\mathrm{Q}^{(\mathrm{p})}\}, \{\hat{\mathrm{Q}}^{(\mathrm{p})}\})$ to fit a warp function. For simplicity, we suggest fitting an affine resampling matrix per burst $\mathrm{A}_{\mathrm{i}}^{(\mathrm{p})}$ such that

$$\mathrm{Q}^{(\mathrm{p})} - \mathrm{B}_{\mathrm{i}}^{(\mathrm{p})} \xrightarrow{\mathrm{A}_{\mathrm{i}}^{(\mathrm{p})}} \hat{\mathrm{Q}}^{(\mathrm{p})} - \mathrm{B}_{\mathrm{i}}^{(\mathrm{p})}.$$

- Read each burst from the TIFF file, resample with $\mathrm{A}_{\mathrm{i}}^{(\mathrm{p})}$ and stitch into the mosaic using the cuts.

The previous method simplifies the estimation of the warp function by using a limited set of DEM points and an affine matrix. While a dense pixel-by-pixel warp function is the ideal way to apply the corrections, the proposed method is simpler and more computationally efficient.

In the case where we need to register a secondary image onto the primary image mosaic, the approach can be adapted with slight modifications as follows:

| (lon, lat) | Rel. orbit | Start date | End date |
|---|---|---|---|
| (151.57, -33.08) | 147 | 2019-09-07 | 2021-09-08 |

Table 5.1: The S1A dataset used in the experiments.

- Find the bursts in the secondary product that match the bursts in the primary product and define the secondary mosaic limits from the limits of the bursts.
- For each point Q that was projected into burst "i" of the primary image, project and correct it in the burst "i" of the secondary image to get $\hat{\mathrm{Q}}^{(\mathrm{s})}$.
- Use the set of points $(\{\mathrm{Q}^{(\mathrm{p})}\}, \{\hat{\mathrm{Q}}^{(\mathrm{s})}\})$ to fit a warp function. For simplicity, we suggest fitting an affine resampling matrix per burst $\mathrm{A}_\mathrm{i}^{(\mathrm{s})}$ such that

$$\mathrm{Q}^{(\mathrm{p})} - \mathrm{B}_\mathrm{i}^{(\mathrm{p})} \xrightarrow{\mathrm{A}_\mathrm{i}^{(\mathrm{s})}} \hat{\mathrm{Q}}^{(\mathrm{s})} - \mathrm{B}_\mathrm{i}^{(\mathrm{s})}.$$

- Read each burst from the secondary TIFF, resample with $\mathrm{A}_\mathrm{i}^{(\mathrm{s})}$, and stitch into the primary mosaic using the primary cuts.

## 5.4 Experiments: Evaluation of overlap alignment

We conducted our experiments on 31 Sentinel-1 images around the eastern coast of Australia acquired from September 2019 over a span of 2 years as shown in Table 5.1. Even if not all available S1 acquisitions were used, the interval was sampled somewhat uniformly in time by 31 images.

The first image in the time series was considered as the primary, i.e. it defined the reference frame onto which all other images would be aligned. We restricted the study to the VV polarization and on all the bursts of the first swath. SRTM30 [FRC⁺07] was used to provide a DEM that covers the extent of the image. The precise S1 orbit data was downloaded and used with all products.

Then, the method defined in Section 5.3 was used to estimate the burst resampling matrices for the primary image, as well as the secondary images. The correction $\mathcal{C}$ used was the composition of the APD correction, intra-pulse correction, and fine bistatic correction [SS19], which we introduced in Sections 1.2.3 and 5.2.

Afterward, since it is fairly simple to adapt a burst resampling matrix to work on a specific area within the burst by accounting for the necessary translation, we restricted the experiment to the burst overlap areas. Since there are 9 bursts per swath, we got $8 \times 2$ overlaps per image. Therefore, $31 \times 8 \times 2$ overlaps were read from the TIFF files as crops and resampled. In theory, each forward overlap (end of burst "i") should be well aligned with the backward overlap (start of burst "i+1") after resampling. The overlaps should also be well-aligned across the time series. To validate the method, we checked the precision of the registration by re-estimating a residual shift using the phase-correlation method [HdFFM21] on the amplitude of the overlap crops. The baseline against which we compared our results is the case where $\mathcal{C}$ is the identity. In that case, in the primary image, the resampling matrices are equal to the identity, and the overlaps were simply read from the TIFF files without resampling. For the secondary images, the overlaps were resampled, and the affine matrix used accounts for the orbit difference but didn't include the finer corrections previously considered.

| | Before correction | After correction |
|---|---|---|
| az shift (m) | 0.086 ± 0.35 | 0.15 ± 0.334 |
| rg shift (m) | -0.57 ± 0.16 | -0.021 ± 0.15 |

Table 5.2: Measured shift between the overlaps of bursts "i" and "i+1". The measurement was performed on 31 S1 images on the first swath and on the 8 overlaps. Each measurement is shown with and without the application of the proposed method. The table shows the average value and the standard deviation in meters.

The results are shown in Tables 5.2 and 5.3. Table 5.2 shows that before the correction, the end of the burst "i" is shifted by approximately 0.57 m in range to the left of the start of the burst "i+1". This observation is mainly due to the intra-pulse effect. After the corrections, we can see that the alignment of the two consecutive burst overlap areas has significantly improved (approximately -0.021 m). As for the azimuth shift, the average value of the shift is slightly higher after applying the corrections. This result is counter-intuitive, and we attribute it to the remaining azimuth corrections that were not taken into consideration. Indeed, similar experiments on a flat region showed much-improved azimuth accuracy after correction, indicating that the topography-dependent DC correction, which is missing from our processing, is key to achieving high-precision registration.

| | Before correction | After correction |
|---|---|---|
| az shift (m) | 0.057 ± 0.2 | 0.08 ± 0.2 |
| rg shift (m) | -0.074 ± 0.099 | -0.063 ± 0.098 |

Table 5.3: Measured shift between the images in the time series. The measurement was performed on 30 (secondary) S1 images on the first swath and on the 8 overlaps (16 crops per image) with respect to the primary image (the first date). Each measurement is shown with and without the application of the proposed method. The table shows the average value and the standard deviation in meters.

For Table 5.3, two observations can be made. The first is that even without using the fine projection corrections aggregated in $\mathcal{C}$, the measured precision of the registration on the time series is satisfactory. The second observation is that the applied corrections do not improve the precision of the registration. We should be careful while interpreting this result since, in theory, the registration should be less precise without the corrections. However, this shows that the corrections included in $\mathcal{C}$ here affect the primary and the secondary images in a similar way. For example, looking back at Equation 5.1, we can see that if the Doppler centroid reaches similar values within a primary and secondary burst, the intra-pulse shift would be similar. Therefore, instead of performing the match on Q, we perform it on a pixel slightly shifted. Since the shift is approximately the same in both bursts, the targets would still provide a good correspondence for the registration estimation. However, we would not recommend generalizing this result, since, depending on the corrections applied and their implementation, the amount of impact they have on a primary and secondary burst can be very different. Furthermore, even though the bursts can be well aligned in the time series without corrections, they would not be well-aligned with respect to each other in the mosaic.

## 5.5 Conclusion

In this study, we have proposed a method to correct the geometric inconsistencies between bursts before forming a mosaic. The relative shift between the bursts at the boundaries stems from effects that arise when processing IW burst data, like the intra-pulse shift, which affects each burst differently. To account for these effects, it is suggested to use a geolocation-based procedure, in which points on the surface of a DEM are projected into the scene with and without corrections. The warp function in the burst coordinates is then approximated as an affine matrix, and each individual burst is resampled before stitching. This procedure can be adapted to secondary image alignment.

Experiments on a dataset of real S1 images showed significant improvements in the burst alignment in the overlap areas with the proposed method, especially in the range direction. This can mainly be attributed to the compensation of the intra-pulse shift. It was also argued that even though the improvement of the registration in a time series of secondary images is not evident, it is preferable to apply the proposed method to ensure good precision in general with any type of correction and to get a consistent burst mosaic.

In the future, we wish to apply the method with more of the well-known S1 geolocation corrections [SS19], especially with the release of the Extended Timing Annotation Dataset for Sentinel-1 [GLM+22]. It would also be interesting to validate our geolocation on sites containing corner reflectors, like the calibration site in the Surat Basin, Australia. Finally, designing a pixel-by-pixel resampling procedure and comparing the accuracy and computational efficiency of both methods would also be relevant.

# Part II

# Exploring Deep Learning for InSAR

# 6 Phase denoising and coherence estimation network

In this chapter, we examine the joint denoising and coherence estimation performance of the network known as Φ-Net (Sica et al. 2021). We briefly examine the method, network architecture, training data and strategy. Then, in the experimental section, we compare the network's performance against the simple boxcar uniform filter on real Sentinel-1 interferograms containing topographic fringes. We verify the observations made by the authors, in particular concerning the superior denoising performance and preservation of fine details in the coherence estimation. Furthermore, we notice a link between the boxcar filter and Φ-Net when comparing their results, especially in areas heavily impacted by noise. We assume that this is naturally explainable by interpreting Φ-Net as a network that acts on the residual of a strided boxcar filter. Finally, we notice some discontinuities in the Φ-Net fringes. Hence, it is likely that an end-to-end deep learning method might bring a small improvement to the patch-based approach by increasing the receptive field.

## 6.1 Introduction

As we saw in Section 1.2.2 but with a slightly different notation, Interferometric Synthetic Aperture Radar (InSAR) consists of combining two different Synthetic Aperture Radar (SAR) Single Look Complex (SLC) images $z_1$ and $z_2$, and an interferogram $\Gamma$ is computed by applying the complex multiplication

$$\Gamma = z_1 \cdot z_2^*, \tag{6.1}$$

where $*$ denotes the conjugation operation. The interferometric phase $\Phi_z$ is defined and interpreted by

$$\Phi_z = \angle \Gamma = \frac{-4\pi}{\lambda} \Delta R + \Phi_{noise}, \tag{6.2}$$

where $\angle$ refers to the phase of the complex number $\in [-\pi, \pi)$, $\lambda$ is the radar carrier wavelength, and $\Delta R$ is the change of distance between the reflector and the satellite. Therefore, $\Phi_z$ is related to the change in distance to the target, which can be linked to the scene topography and deformation in the satellite's line of sight, among other factors. Since $\Phi_z$ can only be observed in a $2\pi$ interval, phase jumps called fringes will be present in the signal. Phase unwrapping is, therefore, a necessary processing step to obtain a consistent phase field. However, in practice, the observed phase is contaminated by noise $\Phi_{noise}$ due to several decorrelating effects (thermal noise, speckle, change in the scattering mechanism, different acquisition geometries, and processing errors...). This increases the difficulty of phase unwrapping. Therefore, phase denoising is usually performed before phase unwrapping. Phase unwrapping is discussed in more detail in chapter 7

Furthermore, it is usually of interest to measure the local complex signal correlation $\gamma_0$ of the two SAR images defined as

$$\gamma_0 = \frac{\mathbb{E}\left(z_1 \cdot z_2^*\right)}{\sqrt{\mathbb{E}\left(|z_1|^2\right) \cdot \mathbb{E}\left(|z_2|^2\right)}} = \rho \cdot \mathrm{e}^{j\phi}. \tag{6.3}$$

Here, $\gamma_0$ can be decomposed into the coherence $\rho = |\gamma_0| \in [0, 1]$ and the denoised phase $\phi = \angle\gamma_0$. The coherence $\rho$ is usually a good indicator of the phase noise level and, consequently, of the reliability of pixels for further analysis. For example, it can be used as a quality map in phase unwrapping. Coherence estimation can also be useful in other applications, such as change detection, where a local coherence loss could indicate that the area is affected by a change between the two dates [MMSP22](flood mapping [GWV96], volcanic ash mapping [JKLY16]...)

Therefore, algorithms for estimating the InSAR denoised phase and coherence have been actively developed throughout the years. Here, we will mention a few algorithms and refer to [XGLX20] for a more comprehensive overview. The most straightforward method is to the multilook filter [LMM94], i.e. a simple boxcar moving average filter chosen as a proxy of the expectation operation $\mathbb{E}$ in Equation 6.3. Its main drawback is that the estimation quality deteriorates when the signal is not locally stationary within the estimation window. This has motivated the introduction of adaptive filtering techniques such as the Lee filter in [Lee98], where directional windows are used to consider the fringe direction. Also, local noise statistics are considered in the final estimation. On the other hand, it is also possible to filter the interferogram in a transformed domain. For example, a widely used filter in the frequency domain is known as the Goldstein filter [GW98]. This method denoises patches in the image separately and then recombines them to form the final denoised image. The filter is designed as the power $\alpha$ of the smoothed modulus of the Fourier transform of the patch ($\alpha$ varies between 0 and 1 and controls the filtering power). Similarly, sparse representations have been used to tackle this problem in the method termed SpInPhase [HBDK15], where a dictionary of patches is learned from the data, and each patch is represented as a sparse linear combination of dictionary patches. More recently, non-local patch-based filters have been applied to InSAR data because of their texture preservation properties. These methods start by assigning weights to patches in a local search window based on a similarity measure to the central patch. Then, the patches are typically used for joint filtering before recombining to provide the final filtered result. NL-InSAR [DDT11] is a typical patch-based method characterized by its iterative scheme. At each iteration, similarity weights with neighboring patches are set based on the posterior probability of having the same underlying parameters. Then, a weighted maximum likelihood estimate is used to provide the filtered phase, coherence and reflectivity for the current iteration. Simply put, the similarity criterion and the estimate are based on the SAR data statistics. In [SCZ+18], the BM3D [DFKE07] non-local collaborative filtering algorithm is extended to InSAR and denoted InSAR-BM3D. Then, in [SCVP18], an offset compensation criterion for patch similarity evaluation is established. Thus, OC-INSAR-BM3D is the offset-compensated version of InSAR-BM3D and demonstrates state-of-the-art filtering performance.

On the other hand, in recent years, Convolutional Neural Networks (CNNs) have been applied successfully to image processing tasks. In [ZZC+17], the DnCNN network was

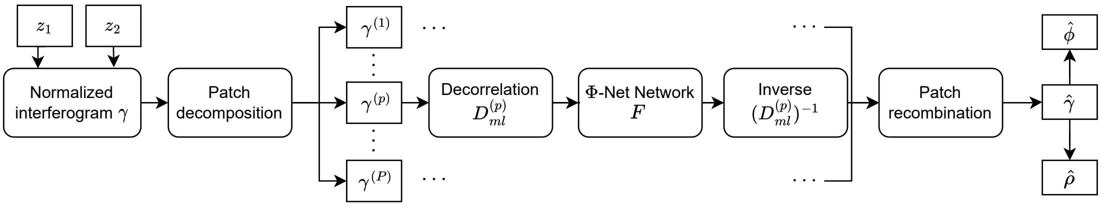

Figure 6.1: Denoising workflow with Φ-Net. We can see that the normalized interferogram is decomposed into P patches. Each patch is decorrelated and then fed to the network. The inverse transform is then applied, and the patches are recombined.

proven to perform highly effective image denoising. Residual learning is highlighted as an important factor to boost denoising performance. In [KZM+18], the first CNN with residual connection is used for InSAR phase denoising. Φ-Net [SGRB21] combines residual learning with the well-known U-net architecture [NHWF15] to solve the interferometric phase denoising and coherence estimation task. Even though more recent articles tackling the problem of InSAR phase denoising using CNN architectures have emerged [VFP22, VFPS22], Φ-Net [SGRB21] showed state-of-the-art performances at the time of its release. Furthermore, the model is available online for testing, which makes our evaluation study possible.

In this chapter, we examine and test the network Φ-Net [SGRB21]. The chapter is organized as follows: in Section 6.2, we briefly inspect the method, the network architecture, the simulated dataset, and the training strategy. In Section 6.3, we perform experiments on some Sentinel-1 interferograms and compare the estimates of Φ-Net against the boxcar uniform filter. Section 6.4 provides a short guide for running the demo.

## 6.2 Method: Network design

This section will first explain the forward inference for estimating the noise-free parameters $\rho$ and $\phi$ of a couple of Single Look Complex (SLC) images $z_1$ and $z_2$. Specifically, some pre-processing and post-processing are highlighted, as well as the network architecture. Then, we will briefly look at the training data and the training strategy used by the authors since we did not re-train the network. Note that the code for this part is not made public and that the following section is based solely on the original article [SGRB21].

### 6.2.1 Forward estimation

Starting from the two images $z_1$ and $z_2$, several steps are needed for the forward estimation as seen in Figure 6.1:

1. A normalized interferogram is computed. To do so, it is assumed that both images have the same amplitude $A$, and an estimate $\hat{A}$ is obtained using the maximum likelihood expression

$$\hat{A} = \sqrt{\frac{1}{w^2} \sum_{w \times w} \frac{|z_1|^2 + |z_2|^2}{2}}. \tag{6.4}$$

   Note that we added the term $\frac{1}{w^2}$ to the equation from the original article [SGRB21] so that the sum corresponds to an averaging uniform filter. In simple words, the intensity $|z_i|^2$ $(i \in \{1, 2\})$ is first averaged between the two dates, then a uniform

$w \times w$ ($w = 3$) filter is applied, and the square root is finally taken. Then, the interferogram is normalized with the estimated amplitude:

$$\gamma = \frac{\Gamma}{\hat{A}^2} = \gamma_R + j\gamma_I. \tag{6.5}$$

2. The interferogram image is decomposed into 64 × 64 overlapping patches with a stride 8 in both dimensions. The superscript $^{(p)}$ is used to designate quantities related to the patch $p$. Note that because of the patch decomposition and the fact that the stride is taken as 8, it is preferable to have an image size multiple of 8 in both dimensions; otherwise, some nan pixels will appear at the border of the result. The number of nan pixels is the remainder of the division of the image dimension by 8.

3. For each patch, the decorrelating Karhunen–Loève transform $D_{ml}^{(p)}$ is applied:

$$x^{(p)} = \begin{pmatrix} a^{(p)} \\ b^{(p)} \end{pmatrix} = D_{ml}^{(p)} \begin{pmatrix} \gamma_R^{(p)} \\ \gamma_I^{(p)} \end{pmatrix}, \tag{6.6}$$

   where $\gamma_R^{(p)}$ and $\gamma_I^{(p)}$ are the real and imaginary parts of $\gamma^{(p)}$ and $a^{(p)}$ and $b^{(p)}$ are the corresponding decorrelated quantities. The decorrelating matrix $D_{ml}^{(p)}$ has the following expression:

$$D_{ml}^{(p)} = \begin{pmatrix} \cos\phi_{ml}^{(p)} & \sin\phi_{ml}^{(p)} \\ -\sin\phi_{ml}^{(p)} & \cos\phi_{ml}^{(p)} \end{pmatrix}, \tag{6.7}$$

   where $\phi_{ml}^{(p)} = \angle \sum_{64\times 64} \gamma^{(p)}$ is the phase maximum likelihood estimate over the patch. The matrix $D_{ml}^{(p)}$ is a rotation matrix with angle $-\phi_{ml}^{(p)}$ and can be interpreted as the matrix containing the eigenvectors of the noise covariance matrix (see [SCZ⁺18] for more details).

4. $x^{(p)} = (a^{(p)}, b^{(p)})$ is fed to the network $F$ as two separate channels, and a denoised estimate $F(x^{(p)}) = (\hat{a}^{(p)}, \hat{b}^{(p)})$ is obtained.

5. The inverse transform $(D_{ml}^{(p)})^{-1}$ is applied on the filtered patch

$$\begin{pmatrix} \hat{\gamma_R}^{(p)} \\ \hat{\gamma_I}^{(p)} \end{pmatrix} = (D_{ml}^{(p)})^{-1} \begin{pmatrix} \hat{a}^{(p)} \\ \hat{b}^{(p)} \end{pmatrix}. \tag{6.8}$$

6. The patches are recombined with averaging at overlapping positions. This gives an estimate of $\hat{\gamma} = \hat{\gamma_R} + j\hat{\gamma_I}$.

7. The denoised phase is taken as $\hat{\phi} = \angle\hat{\gamma}$ and the coherence as $\hat{\rho} = |\hat{\gamma}|$.

### 6.2.2 Network architecture

The network architecture is shown in Figure 6.2. It is inspired by the U-Net network, with a shallower architecture since the input patches are small (M = 64). The first stage is an encoder, where the image size is successively reduced with 2x2 max pooling, whereas the number of channels increases. Since the parameter P that dictates the number of channels is set to P=64, the output of the encoder has a size $[\frac{M}{8}, \frac{M}{8}, 8P] = [8, 8, 512]$ (the size specified in the original article network description is $[4, 4, 512]$, which might indicate a

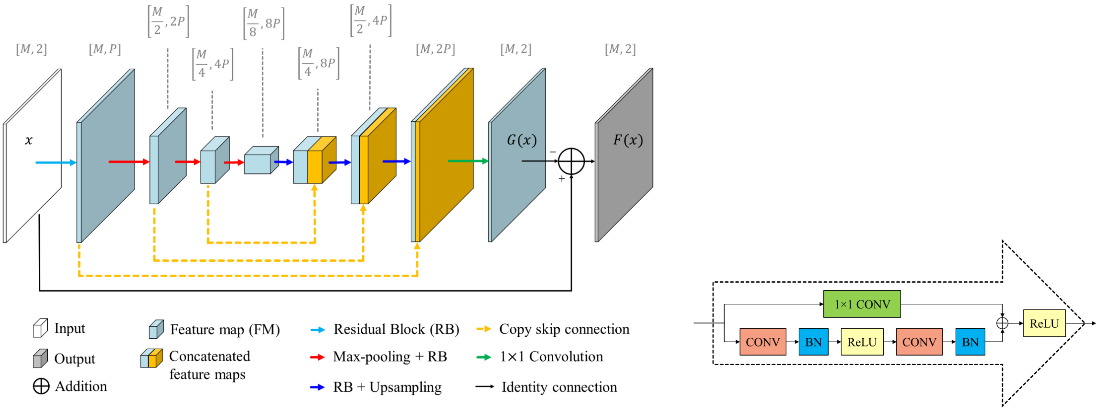

(a) General network architecture. The array dimensions are shown in grey between brackets: [M, P] denotes a M x M array with P channels.

(b) Residual block architecture

Figure 6.2: Figures taken from the original article [SGRB21]. The network architecture is shown on the left. The residual block is shown on the right.

small mistake regarding the array size). The second stage is the decoder, characterized by the inverse process, where the upsampling is conducted using bilinear interpolation. Skip connections are used to copy features (channels) from the encoding stage to the decoding stage. Figure 6.2b shows that the convolutional blocks have been replaced with residual blocks. The convolutional kernels are of size $3 \times 3$, except for the $1 \times 1$ residual connection. The last convolution has a kernel of size $1 \times 1$ as well, and it is used to get two channels representing the noise prediction $G(x)$. The last residual connection defines the denoised output as $F(x) = x - G(x)$.

### 6.2.3 Dataset

#### Signal Model

The dataset is constructed via simulation of the phase, amplitude, and coherence images. The objective is to have both noiseless $(a_0, b_0)$ and noisy simulations $(a, b)$ of the decorrelated channels. Under Goodman's model, $z_1$ and $z_2$ follow a zero mean circular Gaussian distribution with a covariance matrix given by

$$\begin{aligned}\Sigma &= \mathbb{E}\left\{\begin{pmatrix} z_1 \\ z_2 \end{pmatrix}\begin{pmatrix} z_1^* & z_2^* \end{pmatrix}\right\} \\ &= \begin{pmatrix} A^2 & A^2\rho e^{j\phi} \\ A^2\rho e^{-j\phi} & A^2 \end{pmatrix},\end{aligned} \tag{6.9}$$

where $\rho$ and $\phi$ are the noiseless coherence and phase as seen in equation 6.3, and A is the amplitude, considered equal for both images as previously mentioned.

Then, the model used for the simulation of the noisy images $z_1$ and $z_2$ from the underlying noiseless parameters $A, \phi, \rho$ is based on the following equation:

$$\begin{aligned}\begin{pmatrix} z_1 \\ z_2 \end{pmatrix} &= T\begin{pmatrix} u_1 \\ u_2 \end{pmatrix}, \\ T &= \begin{pmatrix} A & 0 \\ A\rho e^{-j\phi} & A\sqrt{1-\rho^2} \end{pmatrix},\end{aligned} \tag{6.10}$$

| Data | Case 1 | Case 2 | Case 3 | Case 4 | Case 5 | Case 6 |
|---|---|---|---|---|---|---|
| Amplitude | LR | TB | NP | TB | NP | NP |
| Coherence | LR | LR | LR | NP | NP | NP |
| Phase | LF/HF | LF/HF | LF/HF | LF/HF | LF/HF | LF+Step |

Table 6.1: The combination of different patterns for the noiseless data simulation. LR refers to Left-Right ramp, TB refers to Top-Bottom ramp, NP refers to Natural Patterns. LF/HF refers to 50 images of Low-Frequency fringes and 50 of High-Frequency fringes, while LF+Step refers to 100 images of Low-Frequency fringes on which random phase Steps were added in some segments based on the coherence. Each column is a simulation of 100 images, which gives a total of 600 images. The image size is 256x256.

where $u_1$ and $u_2$ are two standard circular Gaussian random variables, and T is the Cholesky decomposition of the covariance matrix $\Sigma$. The simulation using equation 6.10 is a simple way to ensure that obtained data $z_1$ and $z_2$ follow a zero mean circular Gaussian distribution and that their covariance matrix equals $TT^* = \Sigma$. Then, the noisy $(a, b)$ simulations are obtained from $z_1$ and $z_2$ by applying the normalization, patch decomposition, and decorrelation steps as shown in Figure 6.1. To get $(a_0, b_0)$, the same decorrelation transform $D_{ml}^{(p)}$ should be applied to the noiseless $\gamma_0 = \rho e^{j\phi}$.

### Noiseless data simulation

We need to simulate $A$, $\rho$ and $\phi$ for the noiseless data simulation. First, For the amplitude and coherence, two types of simulations were used:

1. Linear horizontal Left-Right (LR) ramps or vertical Top-Bottom (TB) ramps,
2. Natural Patterns (NP) from optical images taken from the NWPU-RESISC45 dataset [CHL17].

As for the phase, the SRTM [FRC$^+$07] (30 meters resolution) digital elevation model was used at two locations in Austria with Tandem-X acquisition parameters to generate topographic phase simulations. From the simulations, two subsets of 250 patches presenting Low-Frequency (LF) and High-Frequency (HF) spatial variations, respectively, were selected. These phase simulations were associated with different combinations of amplitude and coherence simulations (linear ramps or natural patterns). Also, another 100 low-frequency phase patches were selected and combined with amplitude and coherence images selected from natural patterns. In this case, the coherence images were segmented based on a watershed technique with two segmentation intervals: $0.6 < \rho < 0.8$ and $0.8 < \rho < 1$. In each segment, a random phase Step was added to the Low-Frequency pattern (LF+Step). The phase steps were simulated from a zero mean Gaussian distribution with standard deviation $\sigma = \pi\frac{\sqrt{2}}{6}$ which ensures that $3 * \sigma$ is in the $[-\pi, \pi)$ interval. Table 6.1 summarizes the combinations used for the noiseless simulation. In the end, 600 simulations of size 256 x 256 were obtained. These simulations reflect different patterns and correlations between the amplitude, coherence and phase.

| Idx | Area | Primary date | Secondary date | Centroid (lon, lat) | orbit | $B_\perp(m)$ |
|---|---|---|---|---|---|---|
| A | Etna | 20220411 | 20220505 | 14.9863, 37.7429 | 124 | -139 |
| B | El Capitan | 20210710 | 20210728 | -119.6358, 37.7422 | 144 | -107 |
| C | War Jan | 20230118 | 20230130 | 65.3277, 32.4301 | 42 | -310 |
| D | Kilimanjaro | 20180809 | 20180821 | 37.3586, -3.0648 | 79 | 130 |

Table 6.2: Sentinel-1 dataset consisting of image couples selected over mountainous regions at two dates with small temporal separation and big geometric baseline $B_\perp$ separation. This setting is designed to optimize the observation of topographic fringes.

### 6.2.4 Training

The loss used for the training is as follows

$$\begin{aligned} L\left(a_0, b_0, \hat{a}, \hat{b}\right) &= L_2\left(a_0 - \hat{a}, b_0 - \hat{b}\right) + \lambda R(\hat{a}, \hat{b}) \\ &= \left\| \begin{bmatrix} a_0 - \hat{a} \\ b_0 - \hat{b} \end{bmatrix} \right\|_2 + \lambda \cdot \left\| \begin{bmatrix} \max(0, |\hat{a}| - 1) \\ \max(0, |\hat{b}| - 1) \end{bmatrix} \right\|_1 . \end{aligned} \tag{6.11}$$

The first term is an $L_2$ loss term between the predicted denoised channels $(\hat{a}, \hat{b})$ and the ground truth noiseless data $(a_0, b_0)$. The second term is a regularization that encourages the output to be less than 1 in absolute value. It is only active when at least one of the outputs $(\hat{a}, \hat{b})$ is greater than 1 in absolute value, and in this case, the $L_1$ loss is used to penalize it. Parameter $\lambda$ was used to adjust the regularisation amount and was empirically set to $\lambda = 10^{-2}$.

The dataset was split into 540 training images and 60 validation images. The training data was also split into $64 \times 64$ patches of stride 8. Since the patches have a lot of overlap, to augment the diversity of the data, each patch was rotated by 90° with respect to the neighboring patch, and the sign was switched every four patches. This process yielded $N_T = 337408$ patches for the training and $N_V = 37376$ patches for the validation. The batch size was taken as $B_s = 128$, and the learning rate as $l_r = 10^{-4}$ and was decreased every 15 epochs by a factor [10,20,30]. The training converged after 50 epochs, and the validation loss indicated no over-fitting.

## 6.3 Experiments: Evaluation on Sentinel-1 data

In this section, we conducted a few experiments with the Φ-Net network to assess its denoising capabilities.

We compared the results against the simple boxcar filter given by

$$\hat{\gamma}_{\text{box}} = \frac{\sum_{s\times s}\left(z_1 \cdot z_2^*\right)}{\sqrt{\sum_{s\times s}\left(|z_1|^2\right) \cdot \sum_{s\times s}\left(|z_2|^2\right)}} = \hat{\rho}_{\text{box}} \cdot \mathrm{e}^{j\hat{\phi}_{\text{box}}}, \tag{6.12}$$

where the expectation in Equation 6.3 is replaced by the empirical sum on a moving window of size $s \times s$. We chose $s = 5$, as it is the same size selected in the Φ-Net article in its experimental section [SGRB21].

We conducted experiments using Sentinel-1 data on mountainous regions, for which the characteristics are listed in Table 6.2. Two aligned image crops $c_1$ and $c_2$ of size 256x256

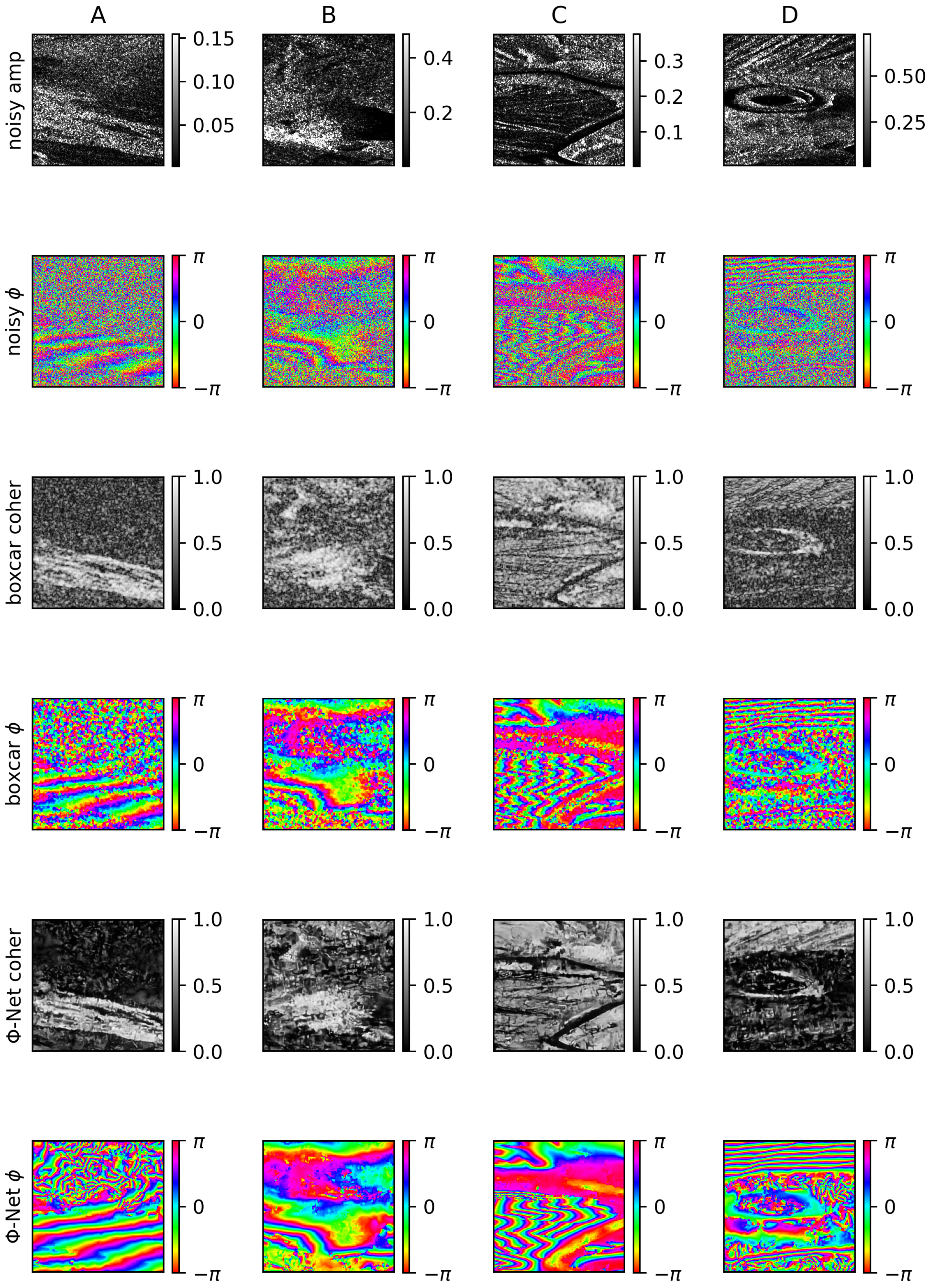

Figure 6.3: Performance comparison on the four areas of interest of Table 6.2. The first two rows show the noisy interferogram; then we show the denoised phase and coherence estimation with the boxcar filter and the Φ-Net network.

were computed for each area of interest. The orbital phase contribution was also simulated as $\phi_{orb}$, and compensated from the secondary image, such that

$$\begin{aligned} z_1 &= c_1, \\ z_2 &= c_2 \cdot e^{j\phi_{orb}}. \end{aligned} \tag{6.13}$$

After compensation, the interferogram $\Gamma$ obtained through Equation 6.1 is mainly affected by topographic phase components, which is the most interesting contribution to observe on this terrain.

The results are shown in Figure 6.3. Looking at the results globally, we can see that the $\Phi$-Net phase and coherence are cleaner than the boxcar estimation. In particular, the fringes on the top of the image in example D are perfectly denoised with $\Phi$-Net, whereas the boxcar filter struggles to remove the noise in this area completely. Notice that the fringes are dense and difficult to discern in the original noisy phase. $\Phi$-Net also succeeds in estimating the coherence, attributing it a high value in this area, which indicates robustness to the fringe density.

Another observation can be made on the $\Phi$-Net phase estimation in areas highly contaminated with noise (low coherence). At first glance, we might say that the network produces two different types of results in these regions. It either introduces high-frequency fringes, such as the ones in A and D, or some low-frequency smooth phase estimation. In fact, when looking at the boxcar results for the same areas, we notice a link with the $\Phi$-Net results. When the boxcar is applied on areas completely noisy (top of image A), we see some small random color patches in the denoised phase. In this case, $\Phi$-Net hallucinates fringes consistent with the boxcar pattern. Conversely, when the boxcar filter finds a common phase in the noisy region, i.e. the small patch colors are slightly coherent (bottom of B, or river in C), $\Phi$-Net provides a filtered phase with this common color. This observation might be better interpreted if we look at the $\Phi$-Net workflow in Figure 6.1. Indeed, the input image is decomposed into overlapping patches, and then the patch phase is subtracted (Decorrelation) before going into the network. Finally, the patch phase is added back, and the patches are recombined. Thus, the Decorrelation of patches is analogous to the boxcar estimation, and $\Phi$-Net can be thought of as being a network that extracts an additional signal from the residual of the boxcar filter. This might explain the visual link we see in the results of $\Phi$-Net and the boxcar filter. In any case, even though introducing fringes in noisy areas might be considered undesirable, $\Phi$-Net designates these areas as incoherent.

An interesting feature of $\Phi$-Net is the very good resolution of the coherence estimation. For example, in image C, we can see the preservation of small details around the river. The river edges look very sharp, and the coherent pixels from the river bank do not propagate to the river, i.e. the network is sure that the river area is incoherent and assigns it a low value. Other details that can be seen are small bright spots or linear structures. The width of such structures seems to be around 2 pixels, indicating only a small loss of resolution compared to the original Sentinel-1 image, which is impressive.

Our last observation is on image C, where some horizontal discontinuities can be seen very clearly in the $\Phi$-Net phase fringes. These discontinuities can also be slightly seen in the boxcar results, which brings us back to the analogy between both methods. However, looking at the original interferogram, one could hope to recover fringes without these discontinuities. This might be attributed to the patch-based processing upon which $\Phi$-Net is built. Perhaps using a fully convolutional neural network, one might increase the

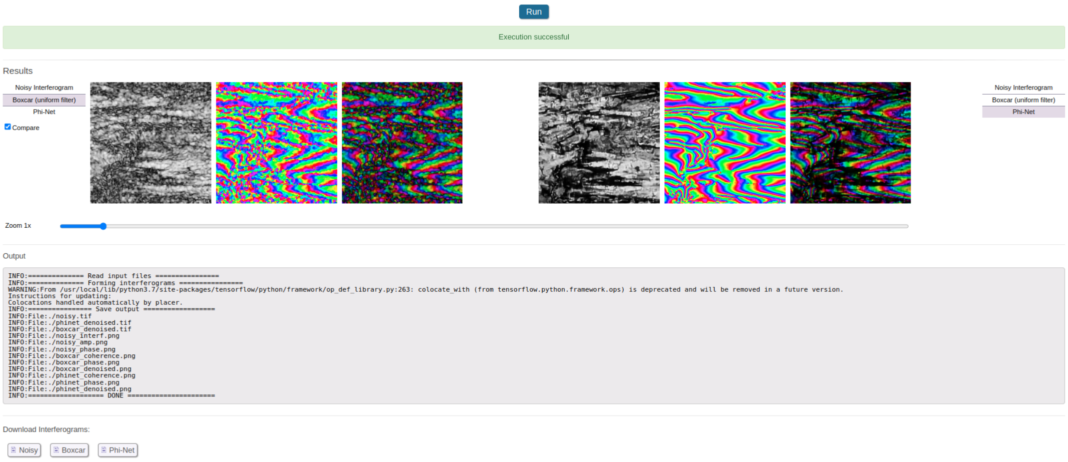

```
INFO:============== Read input files ================
INFO:============== Forming interferograms ================
WARNING:From /usr/local/lib/python3.7/site-packages/tensorflow/python/framework/op_def_library.py:263: colocate_with (from tensorflow.python.framework.ops) is deprecated and will be removed in a future version.
Instructions for updating:
Colocations handled automatically by placer.
INFO:================ Save output =================
INFO:File:./noisy.tif
INFO:File:./phinet_denoised.tif
INFO:File:./boxcar_denoised.tif
INFO:File:./noisy_interf.png
INFO:File:./noisy_amp.png
INFO:File:./noisy_phase.png
INFO:File:./boxcar_coherence.png
INFO:File:./boxcar_phase.png
INFO:File:./boxcar_denoised.png
INFO:File:./phinet_coherence.png
INFO:File:./phinet_phase.png
INFO:File:./phinet_denoised.png
INFO:=================== DONE =====================
```

Figure 6.4: The interface of the demo result. The image gallery allows flipping between results and a side-by-side comparison as well. Messages are printed out to indicate the correct execution of the demo. It is also possible to click the download buttons to get the images in TIFF format.

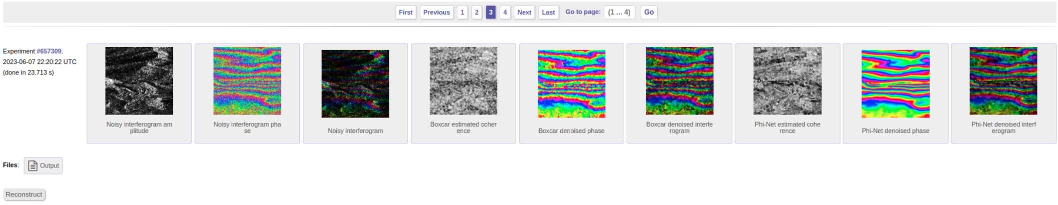

Experiment #657309.
2023-06-07 22:20:22 UTC
(done in 23.713 s)

Figure 6.5: The archive interface. All the plots are saved and the output gallery can be reconstructed by clicking on the “Reconstruct" button.

receptive field beyond the prescribed patch size (64 in this case) and recover globally consistent fringes.

## 6.4 Demo

In this section, we will illustrate the demo usage through an example. On the main page of the demo website, the user will find an exhaustive overview of the input and output description.

In particular, we highlight the image format, order, preprocessing, and size. The output order and colormap descriptions are also detailed. The demo doesn't have parameters, so the user only has to select the inputs by clicking on the “Upload data" button or picking any of the suggested examples. After clicking the “Run" button, the user has to wait until the execution completes. The typical runtime for 256 x 256 images is around 30 seconds. When the execution finishes, the result will be displayed in a gallery, as seen in Figure 6.4. The plots of the results and the log text file are stored in the demo's archive (Figure 6.5) and can be revisited later, downloaded, or visualized with the “Reconstruct" button. However, the TIFF arrays are not archived, and attempting to download the files will result in a failure.

## Acknowledgment

- Original article in [SGRB21], and source code at github

# 7 Phase unwrapping network

Phase unwrapping techniques are used in various applications, including Synthetic Aperture Radar (SAR) interferometry (InSAR). Deep learning methods have been recently proposed to tackle this problem. This chapter aims to explain and evaluate the method proposed by Perera et al. in [A joint convolutional and spatial quad-directional LSTM network for phase unwrapping, ICASSP 2021]. Furthermore, we provide an online demo to simulate phase images and run them through the network. The network performance can be tested visually and through metrics such as the error standard deviation. The simulation can provide some out-of-distribution data, especially with the added atmospheric signal specific to the InSAR phase. We observe from our experiments that the network performance is adequate on in-domain data, with some deterioration on out-of-domain data. The resulting error is structured and might contain stripes, textures, and under-estimated peaks. Finally, we address the fact that the network mutually performs the tasks of phase denoising and unwrapping. We propose to separate the two tasks and restrict the network responsibility on phase unwrapping, which would simplify the evaluation procedure.

## 7.1 Introduction

In many signal processing applications, the quantity of interest is a phase, i.e., an angle that can only be observed in the $[-\pi, \pi)$ interval. Phase unwrapping refers to the process of retrieving the true unseen phase signal, knowing that it can span any arbitrary range. Phase unwrapping is an ill-posed problem since it can have an infinite number of solutions. Nevertheless, it is an essential processing step for many interferometric measurement techniques, such as Synthetic Aperture Radar (SAR) interferometry (InSAR) [GZW88], magnetic resonance imaging [RBR$^{+}$03], and optical interferometry [PJJ94].

For DInSAR, as exposed in Section 1.2.5, unwrapping is usually performed on the differential interferometric phase, which is essential in retrieving an interpretable result. When applied to an image sampled on a uniform grid (an array), it is usually preceded by phase denoising. The topic of phase denoising is exposed in Chapter 6.

In order to solve the phase unwrapping problem, it is necessary to make some assumptions about the structure of the solution, in particular, stating that the actual phase varies slowly along the unwrapping dimension. This assumption is often referred to as the Itoh condition [GP98]. For a 2D image, according to the Itoh condition, the actual phase difference between neighboring pixels does not exceed $\pi$. Using this condition, the true phase gradients in the row and column direction are often approximated from the wrapped phase image gradients. However, in the presence of noise or of a fast varying signal (aliasing of the actual phase) or a discontinuity in the unwrapped signal (for instance, the InSAR phase of a tectonic fault rupturing the surface during an earthquake), the Itoh condition does not hold. Solving this problem is the primary motivation of phase unwrapping. Several approaches exist.

"Path following" methods try to identify the regions where the Itoh condition has potentially failed, and choose a reliable integration path by avoiding these regions. The branch cut method [GZW88], and the quality guided methods such as [GDB$^+$12] belong to that category. On the other hand, optimization-based techniques minimize the $L^p$ norm of the difference between the true phase gradient and the rewrapped gradient of the wrapped image. If $p = 1$, this corresponds to the minimum cost flow method [Cos98]. For p=2, the least-squares method can be solved efficiently with implementations based on the Fast Fourier Transform (FFT) [PS94]. Also under the umbrella of optimization techniques are statistics-based methods like SNAPHU [CZ01].

More recently, several works using deep learning have started to tackle the problem of phase unwrapping [ZYLX21a]. Some deep networks are trained to assist previous classical methods and improve some of their aspects. For instance, in [ZYLX21b], a deep neural network is used to predict the branch cuts, i.e., the regions the integration process should not cross. Therefore, the neural network improves and assists the branch-cut method in [GZW88]. Other networks [ZYL20] predict the phase gradients and are mainly followed by an $L^p$-norm unwrapping step. On the other hand, several deep learning works have attempted to reconstruct the unwrapped phase directly from the wrapped phase image or to predict the ambiguity number, i.e., the integer multiple of $2\pi$ that needs to be added to the wrapped phase in order to retrieve the unwrapped solution. One of the best works that follow this methodology is Phasenet 2.0, detailed in [SGG20].

The article [PD21] analyzed here tackles the problem of phase unwrapping using deep learning. In particular, its objective is to predict the unwrapped phase directly from the wrapped phase image as a regression problem. The proposed network is composed of a novel convolutional architecture, the Convolutional Neural Network (CNN) encoder-decoder architecture, that incorporates a Spatial-Quad Directional - Long short-term memory (SQD-LSTM) module. It is one of the most recent works on the subject and claims to have the best performance in terms of robustness to severe noise conditions and in terms of computational efficiency.

In the following sections, we present the details of the method, including network architecture, simulation of the training data, and the training process. We test the network performance and show some results in the experimental section. The final section provides a complete guide to the online demo.

## 7.2 Method: Network design

### 7.2.1 Network Architecture

The network architecture used is shown in Figure 7.1a. It consists of a convolutional encoder-decoder structure. The output of the encoder is fed to the decoder through an SQD-LSTM module. Each convolutional block shown in grey consists of a $3 \times 3$ convolution layer followed by a batch normalization operation and Rectified Linear Unit (ReLU) activation. In the encoder section, the number of channels (features) is progressively increased while the spatial resolution is decreased through the use of $2 \times 2$ average pooling. In the decoder section, the inverse process occurs as the number of features is decreased,

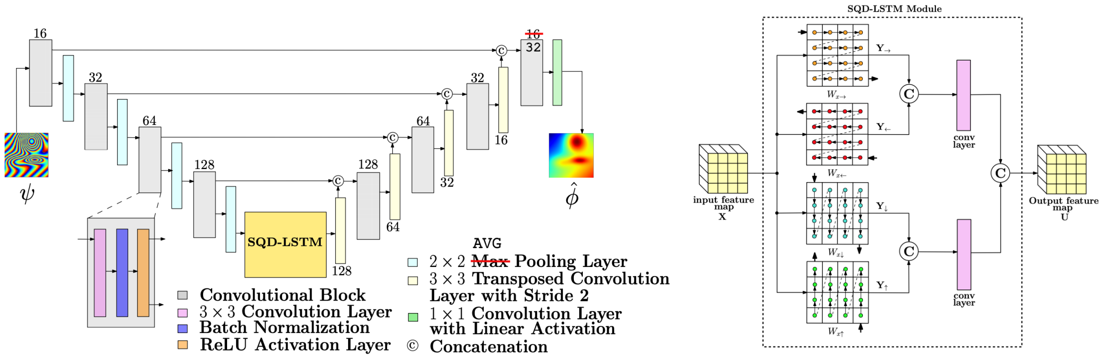

(a) General Network Architecture

(b) SQD-LSTM Architecture

Figure 7.1: Figures taken from the original article [PD21] and slightly modified. The network architecture is shown. The network takes a wrapped image as input and outputs the unwrapped result. Feature size (number of convolutions) is indicated at the top/bottom of the blocks. Max Pooling has been replaced by Average pooling to match the source code. The last convolutional block feature number has been updated to match the source code. The SQD-LSTM module is also shown.

and the image is upsampled with 3 × 3 transposed convolutions. Skip connections are added to concatenate features from the early stages of the encoder with features of the latter decoder stages. The last convolutional block feature number has been updated in the figure to 32 to match the source code. Finally, the last layer consists of a single 1 × 1 convolution with linear activation (the identity). It combines the 32 features from the previous layer into a single pixel-wise scalar output (the unwrapped result).

As for the SQD-LSTM, the detailed structure of this module is shown in Figure 7.1b.

Let $\mathbf{X} = x_{ij} \in \mathbb{R}^{w\times h\times c}$ be the input feature map where $w$, $h$, $c$ refer to width, height, channel number respectively. Let $x_{\rightarrow}$, $x_{\leftarrow}$, $x_{\downarrow}$, $x_{\uparrow}$ be the sequences obtained when one traverses $X$ from left to right, right to left, downwards and upwards respectively as shown in Figure 7.1b. Each element of the sequence is a feature vector $x^{(s)} \in \mathbb{R}^c$, where $s \in [1, \cdots, w \times h]$. These four sequences obtained from $\mathbf{X}$ are passed through 4 different LSTM modules separately. The LSTM output is given by,

$$y^{(s)} = \mathbb{LSTM}(x^{(s)}, y^{(s-1)}; W_x, u) \tag{7.1}$$

where $y^{(s)} \in \mathbb{R}^u$ is the LSTM output at $s$, $W_x$ the unified weights and $u$ the number of units. Therefore, the four LSTM have weights $W_{x_\rightarrow}$, $W_{x_\leftarrow}$, $W_{x_\downarrow}$, $W_{x_\uparrow}$ respectively. The output sequences $y_{\rightarrow}$, $y_{\leftarrow}$, $y_{\downarrow}$, $y_{\uparrow}$ are reordered into feature blocs $\mathbf{Y}_{\rightarrow}$, $\mathbf{Y}_{\leftarrow}$, $\mathbf{Y}_{\downarrow}$, $\mathbf{Y}_{\uparrow}$. The horizontal ($\mathbf{Y}_{\rightarrow}$, $\mathbf{Y}_{\leftarrow}$) and vertical ($\mathbf{Y}_{\downarrow}$, $\mathbf{Y}_{\uparrow}$) directions are concatenated and passed through two different convolutional layers containing $d$ filters each. The final $\mathbb{R}^{w\times h\times 2d}$ is obtained by concatenating the two results from the convolutional layers. For the model at hand, $u$ was set to 32 and $d$ to 64.

### 7.2.2 Data generation

The training is done in a supervised manner and requires wrapped phase images with their unwrapped ground truth. Therefore, a simulation is a simple way to get a training dataset. The authors of [PD21] generated unwrapped images of dimension 256 × 256 by combining a mixture of Gaussians with a phase ramp and additive centered Gaussian noise. The wrapped phase image $\psi(x, y)$ of the synthetic unwrapped phase image $\phi(x, y)$ can be simply obtained by

$$\psi(x, y) = \angle \exp(j\phi(x, y)), \tag{7.2}$$

where $\angle$ is the angle operator that returns a value in the $[-\pi, \pi)$ interval.

By examining the code of the simulation provided by the authors, we can look more closely into the details of the training data. The number of Gaussians is chosen randomly as an integer in $[2, 5]$. Each Gaussian amplitude is selected randomly as an integer in $[50, 1000]$ radians. The location of the Gaussians is chosen randomly in the image (but a 20 pixel margin on the borders is taken so that the center of the Gaussians is always more than 20 pixels away from the border). Each Gaussian's standard deviation (which controls the spatial extent) is taken randomly from $[10, 45]$. Then the Gaussians are summed and multiplied by 0.1. On the other hand, the ramp's slopes in the $x$ and $y$ direction are drawn from a uniform distribution $\mathcal{U}(0, 0.5)$ and the ramp's constant is chosen as a random integer in $[1, 10]$. The ramp is added to the Gaussian mixture.

It is beneficial at this point to stop and examine the interval values chosen by the authors. Each Gaussian in the mixture should yield a phase with a range of at most $\approx 100$ radians (because it is later multiplied by 0.1). Similarly, for the maximum slope for the ramp of 0.5 rad/px, considering the image dimension, the ramp should yield at most 128 rad of phase variation in the image. Therefore, the intervals of values are chosen to balance the Gaussians and the ramp. Then the combination of the Gaussian and the ramp is rescaled to $[-2\pi a, 2\pi b]$, where $a$ and $b$ are chosen random integers in $[1, \text{max\_lower\_bound} + 1]$ and $[1, \text{max\_upper\_bound} + 1]$.

According to the article, the training dataset consists of 6000 images with a 5000-1000 train/test split. As for max_lower_bound and max_upper_bound, they might have been fixed to 6 since the article says that the unwrapped phase range is $[-44, 44]$. However, from the naming of the model in the open source code, we suspect that the given weights correspond to a model trained on 1000 image pairs with $\text{max\_lower\_bound} = \text{max\_upper\_bound} = 4$.

Finally, the standard deviation was determined for the noise simulation from fixed Signal to Noise Ratio (SNR) levels, assuming the signal power was equal to 1 dB. The SNR levels were chosen randomly from $[0, 5, 10, 20, 60]$, which is equivalent to saying the noise standard deviation was chosen randomly from $[1.12, 0.63, 0.35, 0.11, 0.0011]$ radians.

Finally, all the components are added, which gives us the unwrapped phase $\phi(x, y)$. The wrapped phase $\psi(x, y)$ is obtained following Equation (7.2).

### 7.2.3 Training

As mentioned in the introduction, the phase unwrapping problem does not have a unique solution, i.e. many $\phi(x, y)$ can correspond to the same wrapped phase $\psi(x, y)$. Therefore, the network should learn that multiple solutions are possible. Furthermore, it should not be penalized if its output is shifted by a constant w.r.t. the ground truth. Therefore, the loss reflects this last statement,

$$\mathcal{L}_c = \lambda_1 \mathcal{L}_{var} + \lambda_2 \mathcal{L}_{tv}, \tag{7.3}$$

where

$$\mathcal{L}_{\text{var}} = \mathbb{E}\left[(\hat{\phi} - \phi)^2\right] - (\mathbb{E}[(\hat{\phi} - \phi)])^2, \tag{7.4}$$

$$\mathcal{L}_{tv} = \mathbb{E}\left[\left|\hat{\phi}_x - \phi_x\right| + \left|\hat{\phi}_y - \phi_y\right|\right], \tag{7.5}$$

and $\lambda_1 = 1$, $\lambda_2 = 0.1$. $\hat{\phi}$ is the predicted phase and $\phi$ is the ground truth phase.

$\mathcal{L}_{\text{var}}$ minimizes the variance of the difference between the predicted and the ground truth phase (i.e., the difference should be ideally constant). $\mathcal{L}_{tv}$ is the total variation loss that minimizes the $L^1$-norm of the difference between the gradients of the predicted and ground truth phase.

We did not retrain the model and will only explain the training procedure of [PD21]. The model was implemented in Keras and trained using the ADAM optimizer with a 0.001 learning rate. It is worth mentioning that the input phase is the wrapped noisy phase, and the ground truth output is the unwrapped noiseless phase. So the network also learns to denoise the phase during unwrapping. The weights of the convolutional layers were initialized with the he_normal method [HZRS15], i.e. the weights are drawn as samples from a truncated normal distribution centered on 0 with $\sigma = \sqrt{\frac{2}{\text{fan\_in}}}$ where fan_in is the number of input units in the weight tensor.

### 7.2.4 Evaluation

The authors of [PD21] evaluated their method against others, such as Phasenet2.0 [SGG20], on 1000 test samples generated with the same simulation procedure as the one used to get the training data. The other networks were retrained on the same training data for a fair comparison. The metric used is the Normalized Root Mean Square Error (NRMSE - normalized by the max-min range of the corresponding true unwrapped phase image). Each prediction was rescaled by an affinity to match the range of the ground truth before NRMSE computation. Using this evaluation procedure, the authors showed that their method had the lowest NRMSE (0.9%) with the lowest average run time per output (0.054 seconds).

Since the ground truth is not available in an actual phase unwrapping scenario, the rescaling procedure adopted is not really adapted prior to evaluation. In theory, we should only be allowed to add a constant to the result, but scaling is inappropriate. Furthermore, NRMSE might hide some method failures if the data range is significant. However, the authors' statement should still hold since visual comparison in their article shows that the method gives good results.

For our demo, we used the standard deviation of the error as an evaluation metric as seen in Equation (7.6) and (7.7) (similarly to Equation (7.4)), and we also look at its normalization w.r.t. ground truth data range, for completeness, as seen in Equation (7.8)

$$err = \hat{\phi} - \phi, \tag{7.6}$$

$$\sigma_{err} = \sqrt{\mathcal{L}_{var}}, \tag{7.7}$$

$$\text{NRMSE} = \frac{\sigma_{err}}{max(\text{gt}) - min(\text{gt})}, \tag{7.8}$$

where gt is the ground truth image.

## 7.3 Experiments: Evaluation with simulated data

In order to evaluate the performance of the method, we developed our own data simulation. The idea is to generate samples from the training data distribution by wisely choosing specific parameters, and to be able to get out-of-distribution data as well. This will enable us to examine the effect of the chosen parameters on the performance, by visual inspection and by looking at the evaluation metrics.

### 7.3.1 Simulation

The simulation for the demo is inspired by the previous simulation detailed in Section 7.2.2. For brevity, only the differences will be explained here. For the Gaussian mixture, the amplitude is taken this time from $\mathcal{U}(0.2, 1)$. There is also an option to invert (multiply by -1) the amplitude of half the Gaussians. This option is added because the original simulation only had extruding Gaussians. The Gaussians are rescaled to a given interval $[-\frac{\text{gauss\_scale}}{2}, \frac{\text{gauss\_scale}}{2}]$, where gauss_scale is given by the user. The ramp's slopes and intercept are drawn from $\mathcal{U}(0, 1)$. The ramp is rescaled similarly to the Gaussian with a user input ramp_scale. For the noise, the standard deviation can be specified by the user.

An interesting feature added to the simulation is the ability to generate atmospheric phase images. The images occur in the context of InSAR due to the signal propagation delay in the atmosphere. It was shown that a simple way to generate the turbulent component of the atmospheric phase is to use fractal surfaces, typically with a dimension of 2.67, and the code was adapted from the DORIS software Matlab simulation files (insarfractal) [KHP04]. This feature allows us to test the network with out-of-distribution data. The atmospheric signal will be rescaled with a user input atmo_scale.

### 7.3.2 Results

In this section, we test the network with simulated data using different parameters. The parameters of the first configuration are shown in the first line of Table 7.1, for experiment *good*. They should yield an image that looks like the training data. The results of the simulation, as well as the network unwrapping, can be seen in the first line of Figure 7.2. We can see that the network successfully retrieved a continuous unwrapped image that has a similar aspect to the ground truth. The error shows some patterns and is not constant. The error standard deviation is 0.276 rad, which can be acceptable or not depending on the application. Normalizing the error by the ground truth image range, we get NRMSE = 1.04%, where gt is the ground truth image. This result is comparable with the NRMSE values shown by the authors.

| exper_id | n_g | inv_g | g_scl | ramp_scl | $\sigma_{noise}$ | atmo_scl | $\sigma_{err}$ | NRMSE |
|---|---|---|---|---|---|---|---|---|
| good | 4 | no | 15 | 15 | 0.5 | 0 | 0.276 | 1.04 % |
| trivial | 1 | no | 2 | 1 | 0 | 0 | 0.376 | 14.33 % |
| invert_gauss | 4 | yes | 15 | 15 | 0.5 | 0 | 0.341 | 1.81 % |
| atmo | 4 | no | 15 | 15 | 0.5 | 8 | 0.643 | 2.58 % |
| fast_varying | 4 | no | 50 | 15 | 0.5 | 0 | 1.157 | 1.99 % |

Table 7.1: Experiment parameters and results. From left to right: the column abbreviation refers to experiment id, number of Gaussians, invert Gaussians, Gaussian scale, ramp scale, noise standard deviation, atmospheric scale, error standard deviation, normalized root mean squared error, i.e. the normalization of the error standard deviation w.r.t. ground truth range.

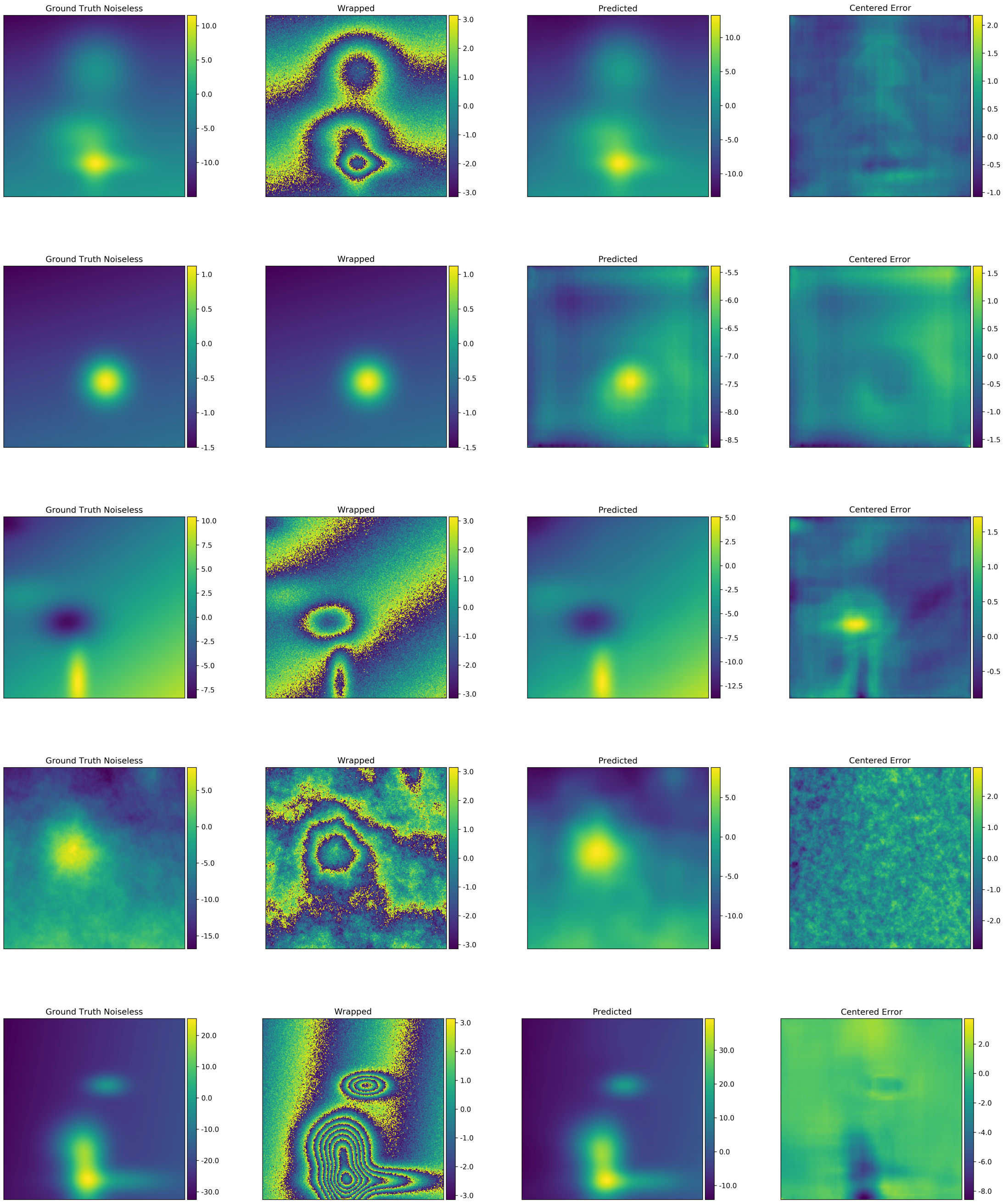

Figure 7.2: Results on the different sets of experiments in the same order as shown in Table 7.1 from top to bottom. From left to right: the ground truth noiseless image, the wrapped noisy image, the predicted unwrapped image, and the centered error.

For the *trivial* experiment, the parameters in Table 7.1 have been chosen to get a small range for the ground truth phase. This way, there would be no fringes (discontinuities) in the wrapped phase, as can be seen in the second line of Figure 7.2. Furthermore, no noise was added, so any traditional phase unwrapping technique would be able to perform the task with very high accuracy. In this case, the output should equal the input shifted by an arbitrary constant. However, the network modifies the input. The error standard deviation of 0.376 might be considered high because of the trivial nature of the problem. The NRMSE reaches the highest value of all our experiments because of the small range of the ground truth. In terms of the visual aspect, we can see clearly in this example, especially in the flat areas, how the network has a tendency to generate stripes and gridded structures in the output.

For the *invert_ gauss* experiment, all the parameters of the *good* experiment are kept, but half the Gaussians will be inverted. It is clear that the error metrics are higher, as seen in Table 7.1. Furthermore, by looking at the error plots, we can see that the error is structured and is higher around the Gaussian peaks. The error is positive for the negative peaks and negative otherwise. Therefore, the prediction underestimates the peaks in both the rising and decreasing cases.

For the *atmo* example, an atmospheric signal was added with a scale of 8 rad. Here, the ground truth is obtained by adding the Gaussians, the ramp, and the atmospheric phase. Since it is preferable to restrict the responsibility of the network, the network should only unwrap and denoise. Looking at the error plots in Figure 7.2, we can see that the network over-smoothed the result and eliminated some components of the atmospheric phase. The atmospheric phase dominates the error since it has been lost in the prediction. This phenomenon explains why the error shows such high values in Table 7.1.

For the *fast_ varying* experiment, the Gaussian scale is increased in a way that would yield a range of values in the ground truth phase near the limits of the ranges seen during training. The resulting wrapped image has many fringes that are close to each other. The network's prediction has a similar aspect to the input image, but the prediction underestimates the peak of the Gaussians. The standard deviation of the error is the biggest in this case, but the NRMSE of 1.99% is reasonable.

We can observe from the previous experiments that the network performed reasonably well on in-domain data. The performance deteriorates on out-of-domain data. This behavior is natural and can be circumvented by simply re-training the network on this type of data. However, the question of network responsibility remains relevant. Even though the association between phase denoising and phase unwrapping might seem reasonable, this complicates the evaluation procedure. Indeed, in this case, part of the error might be due to the denoising task (over/under smoothing). For future studies, predicting the noisy unwrapped image might be interesting, i.e., the network would only try to unwrap the image.

## 7.4 Demo

In this section, the demo developed to showcase the method's performance is illustrated.

Figure 7.3 displays the demo's user interface. The parameters shown are needed to simulate the ground truth unwrapped image $\phi$ and deduce the noisy wrapped image $\psi$. The noisy wrapped image is then fed to the network, and the prediction $\hat{\phi}$ is used to estimate the

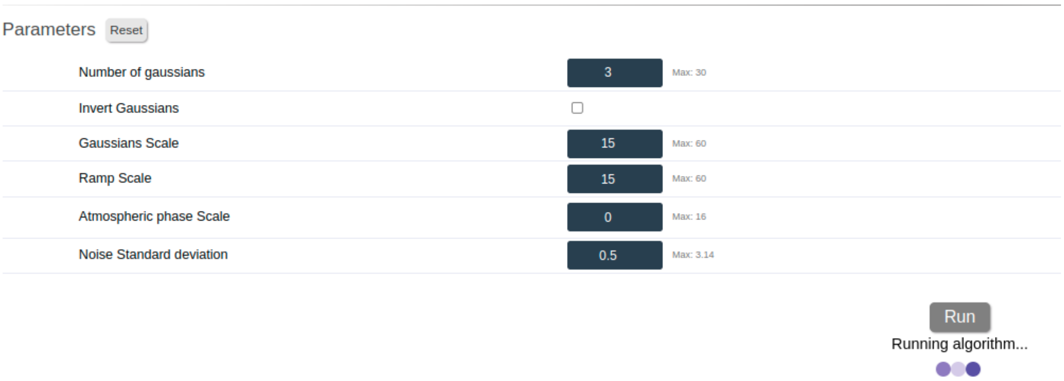

Parameters

Number of gaussians: 3 (Max: 30)
Invert Gaussians: ☐
Gaussians Scale: 15 (Max: 60)
Ramp Scale: 15 (Max: 60)
Atmospheric phase Scale: 0 (Max: 16)
Noise Standard deviation: 0.5 (Max: 3.14)

Running algorithm...

Figure 7.3: Interface of the demo. Each input in a blue box is of numeric type. The maximum value is shown on the right. The number of Gaussians should be an integer, while others can be floating-point scalars. Invert Gaussians is a Boolean represented by a checkbox on the interface. The default values that are shown yield images similar to the training data.

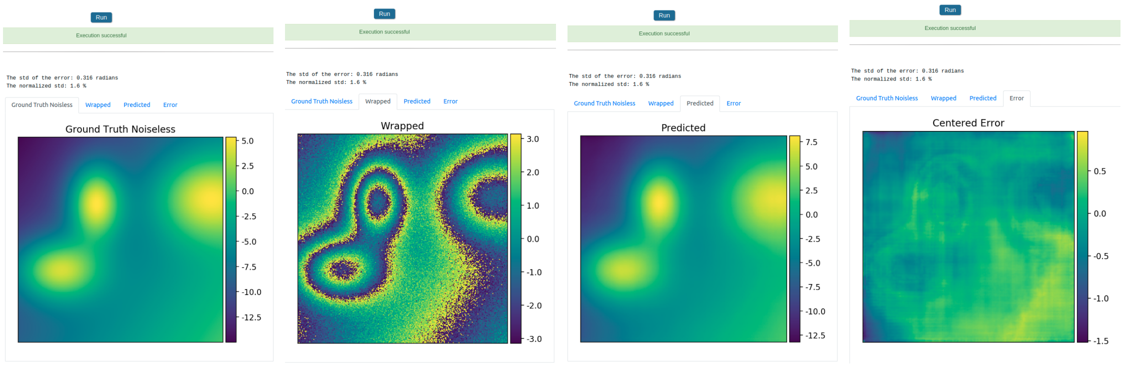

Execution successful

```
The std of the error: 0.316 radians
The normalized std: 1.6 %
```

Execution successful

```
The std of the error: 0.316 radians
The normalized std: 1.6 %
```

Execution successful

```
The std of the error: 0.316 radians
The normalized std: 1.6 %
```

Execution successful

```
The std of the error: 0.316 radians
The normalized std: 1.6 %
```

Figure 7.4: The output of the demo. The metrics are displayed on top of a tabset. Four tabs are available for the ground truth, wrapped noisy, predicted and error image.

error *err* according to (7.6).

The simulation is performed with a set of random variables that control the Gaussian positions, standard deviation, relative scale, ramp slopes, atmospheric phase pattern, and noise pattern. Therefore, re-running the demo with the same parameters will give different realizations of the random variables, different inputs to the network, and different results.

When the user presses the run button, three moving dots are displayed, like at the bottom right of Figure 7.3. When the execution is finished, the user gets a result in the form shown in Figure 7.4. The error standard deviation and its normalization are printed out. A tab set is displayed with the visualized results. Here, each tab was clicked in succession, and the successively displayed images are shown in a single row in Figure 7.4. From left to right, we see the ground truth unwrapped image, the wrapped noisy image, the predicted unwrapping by the network, and the prediction error.

The results are stored in the archive of the demo and can be revisited later and downloaded. As can be seen in Figure 7.5, the archived results not only correspond to the output plots, but also to the individual simulations in the TIFF format, the parameters used for the simulation, and a log text file. The log file contains the parameters of the simulation as

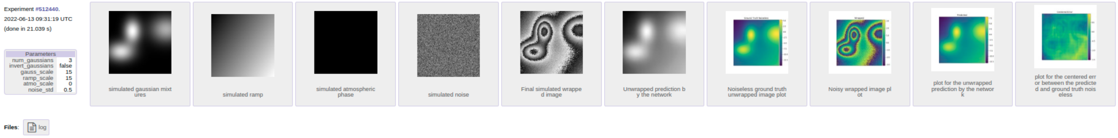

Experiment #512440.
2022-06-13 09:31:19 UTC
(done in 21.039 s)

| Parameters | |
|---|---|
| num_gaussians | 3 |
| invert_gaussians | false |
| gauss_scale | 15 |
| ramp_scale | 15 |
| atmo_scale | 0 |
| noise_std | 0.5 |

Files: log

Figure 7.5: Archive

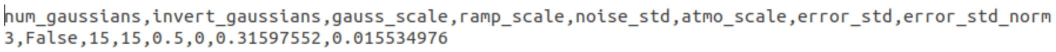

```
num_gaussians,invert_gaussians,gauss_scale,ramp_scale,noise_std,atmo_scale,error_std,error_std_norm
3,False,15,15,0.5,0,0.31597552,0.015534976
```

Figure 7.6: Log text file containing input parameters and output metrics in csv format.

well as the output metrics in csv format, as shown in Figure 7.6.

## Acknowledgment

- Original article in [PD21], and source code at github.
- Doris software for the simulation of the atmospheric phase [KHP04], on which our re-implementation is based.

# Part III

# DInSAR Application

# 8 InSAR on crude oil storage tanks

In this chapter, we examine the possibility of using the interferometric phase on some fixed corners of storage tanks to infer the tank fill ratio. For the study, we use Sentinel-1 data on a site of floating roof tanks for which the fill ratio can be inferred from the floating roof position. We observe a correlation between the phase double difference taken at the fixed roof of neighboring tanks and the fill ratio double difference. The trend suggests that when a tank fills up, the fixed roof corner undergoes a deformation of around 1 cm away from the satellite. We highlight the presence of uncompensated topographic effects and slow temporal trends. We also show the relationship between the noise level in the scatterplots and the amplitude dispersion of the reflectors. We also interpret the poor scatterplots obtained at the fixed base reflector as a result of the layover effect from the floating roof. The previously listed challenges require further investigation and the development of adapted InSAR techniques.

## 8.1 Introduction

A *floating roof tank* is a storage medium typically used for volatile liquids, such as crude oil. In order to reduce evaporation loss, the roof on top of the tank moves vertically as the volume of liquid changes. Since these storage tanks often have large dimensions, they are often visible on images from Synthetic Aperture Radar (SAR) satellite constellations, such as COSMO-SkyMed, TerraSAR-X or Sentinel-1. As shown in Figure 8.1, we typically distinguish three bright pixels per tank in the amplitude of a SAR image in slant range geometry. They appear aligned on the same image row with increasing column index according to range (distance to the satellite):

(A) The corner formed between the platform on top of the tank and the tank façade, i.e., the fixed roof corner.
(B) The corner between the tank façade and its base, i.e., the fixed base corner.
(C) The corner between the inner wall of the tank and the horizontal floating roof, i.e., the floating roof corner.

When looking at a co-registered time series of SAR images, the fixed roof (A) and fixed base (B) corners remain in the same position. Conversely, the floating roof corner (C) moves by a few pixels from one date to another, corresponding to a height change.

In this chapter, we use the previous algorithms exposed in Chapter 3 for deramping (ESA deramping [Mir15, YMPIG+16]) and in Chapter 5 for precise coregistration. We are then able to compute interferometric measurements on the coregistered time series. Our main contributions are:

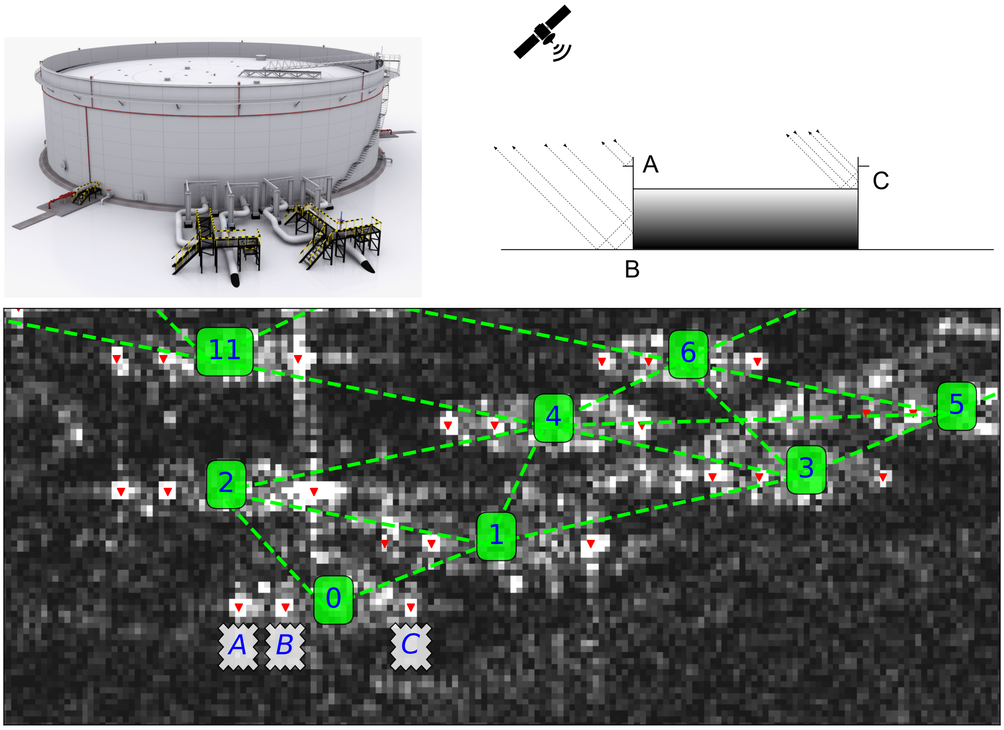

Figure 8.1: SAR acquisition of storage tanks. On the top left is a 3D representation of a storage tank. In the top right, the three corners that exhibit strong reflections in a SAR image. On the bottom, a crop of a SAR amplitude image around some storage tanks for our area of interest. The tank ids and corner positions are displayed. We selected neighboring tanks according to the green connections.

- Establishing a correlation between Interferometric Synthetic Aperture Radar (InSAR) measurements on corners (A) and (B) and tank fill ratio measured using corner (C).
- Presenting a novel InSAR use case that could motivate the development of adapted InSAR techniques.

## 8.2 Related work

Several methods [DLA+20, LS21] were previously developed to convert the floating roof corner (C) column index at a certain date into a crude oil volume (or a normalized "fill ratio" $\in [0,1]$) for the storage tank. On the other hand, InSAR techniques have demonstrated their accuracy in estimating millimetric surface deformation by comparing the phase of Single Look Complex (SLC) SAR images. Recently, InSAR was applied to a pair of Sentinel-1 images of storage tanks to study the potential of the technique in assessing the health and stability of these structures [NON22]. Also, relevant to this study, advanced InSAR algorithms were developed throughout the years [MHR20]. Among those, we distinguish the approach that restricts the analysis to a group of stable reflectors with high Signal-to-Noise Ratio (SNR), called Persistent Scatterers (PS) [FPR01, FPR00]. More precisely, the technique is performed on a time series of SAR images. The simplest metric to evaluate the stability of the scatterer in the PS technique is the amplitude dispersion index, given by

$$D_{\mathcal{A}}(Q) = \frac{\sigma_{\mathcal{A}}(Q)}{m_{\mathcal{A}}(Q)}, \tag{8.1}$$

where $m_{\mathcal{A}}$ and $\sigma_{\mathcal{A}}$ are the mean and the standard deviation of the amplitude values taken along the time series for any point Q in the image. The amplitude dispersion is an indicator of the phase stability, at least for high SNR values [FPR01] (lower $D_{\mathcal{A}}$ means better stability). Therefore, a point Q in the image is selected as a PS if $D_{\mathcal{A}}(\mathrm{Q}) < \tau$, where $\tau$ is a threshold (usually around 0.25).

Furthermore, the phase double difference on reflectors $p$ and $q$ for images $i$ and $j$ is defined as

$$\Delta\Phi_{i,j}\left(p,q\right) = \angle\left[\left(z_i\left(p\right) \cdot z_j\left(p\right)^*\right) \cdot \left(z_i\left(q\right) \cdot z_j\left(q\right)^*\right)^*\right], \tag{8.2}$$

where $z_i(p)$ is the complex number for image $i$ at reflector $p$, $^*$ denotes the conjugation operation, and $\angle$ is the observed angle $\in [-\pi, \pi)$. During PS processing, $\Delta\Phi_{i,j}\left(p,q\right)$ is estimated on two nearby PS reflectors to mitigate the atmospheric effects.

We test the same strategy to derive InSAR measurements between fixed reflectors on the tanks. We can expect that the deformation of the tank will be the predominant signal in the phase double difference. Other noteworthy effects that could have a meaningful impact on the phase double difference are the residual topographic error phase, the noise, and the phase wrapping. Nevertheless, we hope to measure small millimetric movements of the fixed reflectors between two dates, which may indicate crude oil volume change.

## 8.3 Experiments: Comparing InSAR and pixel tracking

Our Area Of Interest (AOI) contains $N_T = 19$ tanks in the Juaymah tank farm in Saudi Arabia (lon=49.987°, lat=26.819°). We selected Sentinel-1 relative orbit 101 and dates from 2017-01-05 to 2021-12-22, resulting in $N_I = 151$ images. We selected the first date as the primary image and generated co-registered crops of size $512 \times 1024$ pixels around our AOI using the procedure presented in chapter 5 based on the geolocation of a set of points sampled on the Shuttle Radar Topography Mission (SRTM) Digital Elevation Model (DEM) [FRC⁺07]. We also estimated an orbital phase $\phi^{orb}$ and a topographic phase $\phi^{topo}$ per image (relative to the primary image) such that the compensation operation is given by $z_i^{orb}(p) = z_i(p) \cdot \mathrm{e}^{j\phi_i^{orb}(p)}$ and $z_i^{topo}(p) = z_i^{orb}(p) \cdot \mathrm{e}^{j\phi_i^{topo}(p)}$. Consequently, phase double differences $\Delta\Phi_{i,j}^{orb}\left(p,q\right)$ and $\Delta\Phi_{i,j}^{topo}\left(p,q\right)$ can be defined according to Equation 8.2.

Since the floating roof may move by several meters between acquisitions, the phase double difference using (C) is affected by phase ambiguity ($2\pi$ cycle is 2.8 cm for Sentinel-1), hence unusable for interferometry. Instead, we attempt to derive a proxy of the tank fill ratio by analyzing the phase double difference using corners (A) and (B). Although corners (A) and (B) are at first order fixed, they may be subject to relative displacement due to tank deformation, presumably resulting indirectly from filling. An estimation of the fill ratio for each tank $k$ and each image $i$, $u_i^k \in [0,1]$, was provided by Kayrros [DLA⁺20]. We define the fill ratio double difference between two tanks and two dates as

$$\Delta u_{i,j}^{k,l} = (u_i^k - u_j^k) - (u_i^l - u_j^l), \quad \Delta u_{i,j}^{k,l} \in [-2, 2]\,. \tag{8.3}$$

We define $A^k$ and $B^k$ the fixed roof and fixed base corners of the tank $k$ respectively, with $k \in \{0 \dots N_T - 1\}$. We compared the values of $\Delta\Phi_{i,j}^{topo}\left(X^k, X^l\right)$ against the fill ratio double difference $\Delta u_{i,j}^{k,l}$, where $X$ can be either $A$ or $B$.

The experiments were conducted on the set of neighboring tanks

$$T = \{(k,l) \mid \text{distance}(k,l) < \tau_{dist}\}$$

as seen in the bottom image of Figure 8.1 (here $\tau_{dist} = 300$ m). The images were also selected from the set

$$S = \{(i,j) \mid \text{duration}(i,j) < \tau_{temp}\}$$

with $\tau_{temp} = 90$ days in this case.

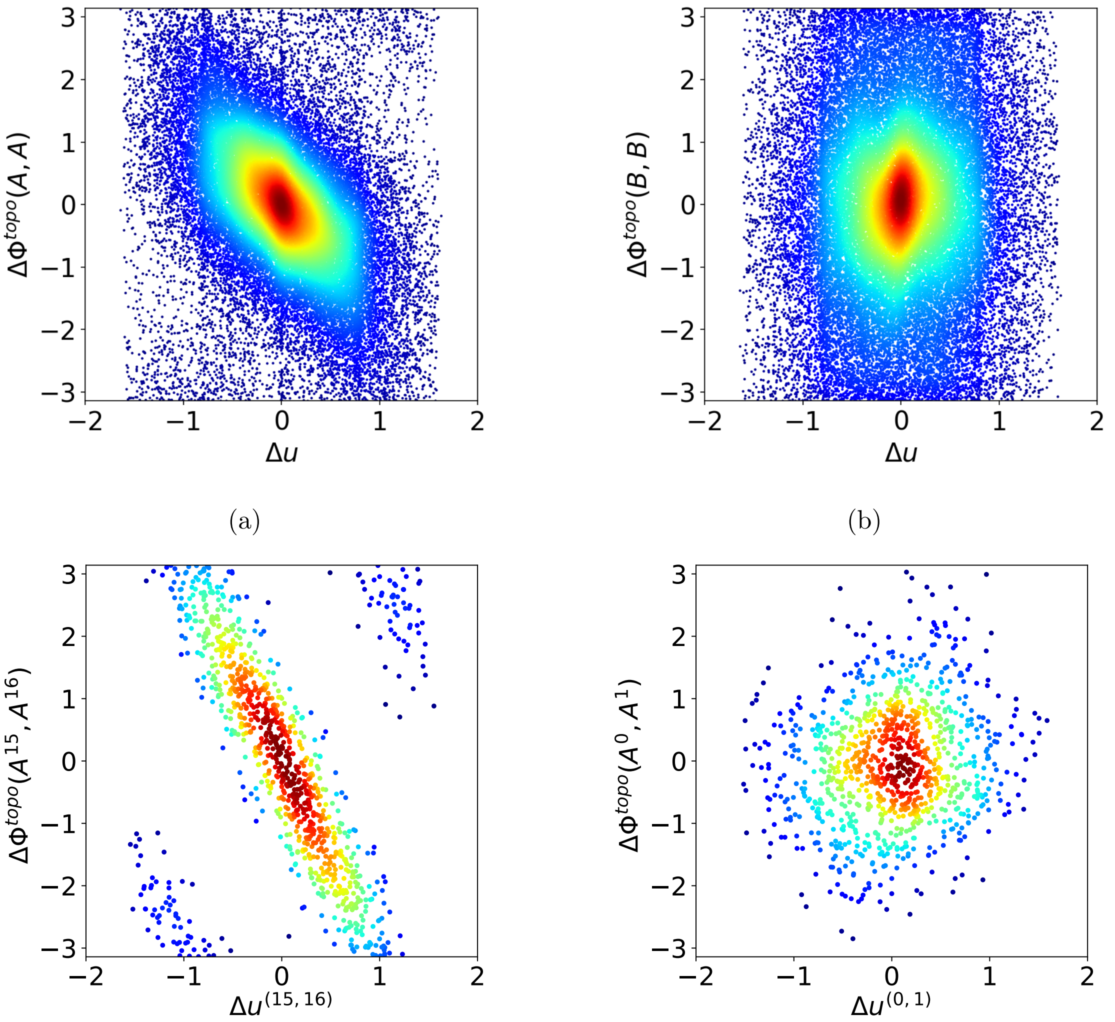

(a)

(b)

(c)

(d)

Figure 8.2: Scatterplots obtained for the phase double difference against the fill ratio double difference between neighboring tanks. The color indicates increasing point density from blue to red obtained using Gaussian kernel density estimation. Figures 8.2a and 8.2b correspond to taking all tank couples at the roof and base, respectively. We see a trend in the roof and no trend in the base. For the last two plots, we show tank couple (15, 16) that exhibits good linear behavior (8.2c) and tank couple (0,1) with no visible correlation (8.2d).

The results can be seen in Figure 8.2. In Figure 8.2a, the phase double difference is taken on the roof for all tank couples in $T$ and all image couples in $S$. When the roof corners $A^k$ are

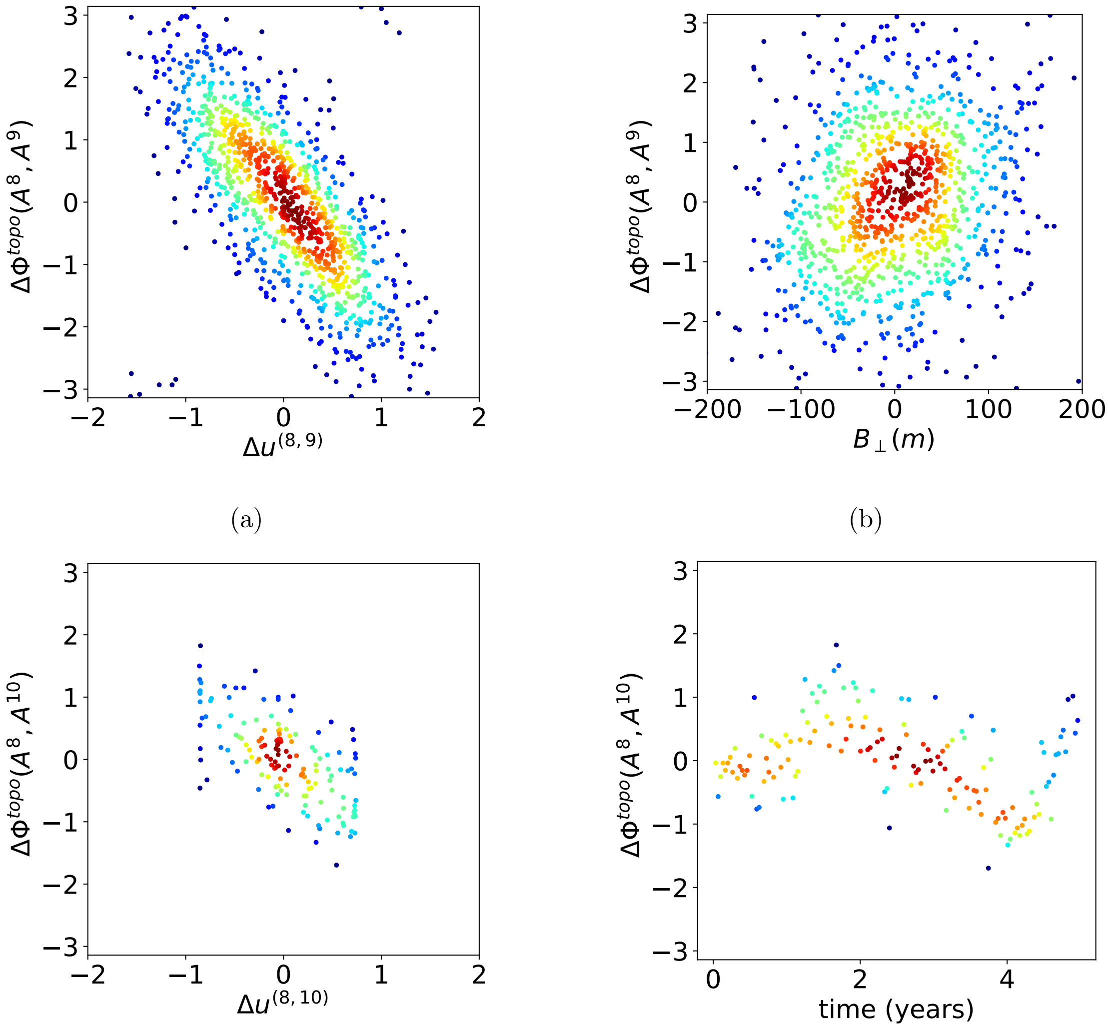

(a) (b)

(c) (d)

Figure 8.3: Scatterplots highlighting the presence of uncompensated effects in the phase. The phase double difference on the roof of tank couple (8, 9) vs. the fill ratio double difference (8.3a), and vs. the perpendicular baseline (8.3b). For the last two plots, all interferograms are done w.r.t. the first date, and the scatterplots were recentered by removing the bias induced by the first date for visualization purposes. We see the phase double difference on tank couple (8, 10) vs. the fill ratio double difference (8.3c) and vs. the temporal baseline (8.3d).

considered, a trend suggesting a negative correlation between the two quantities is visible in approximately half of the tank couples, e.g. couple $(A^{15}, A^{16})$ shown in Figure 8.2c. The plot suggests that the phase double difference is mostly already unwrapped since wrapping occurs on a limited set of points with the biggest absolute values of the fill ratio double difference. Therefore a tank filling up induces a fixed roof movement away from the satellite in the order of 1 cm. This relationship is not verified for the other half of tank couples, e.g. couple $(A^0, A^1)$ in Figure 8.2d. Furthermore, Figure 8.2b shows that no clear trend emerges when using the fixed base reflectors.

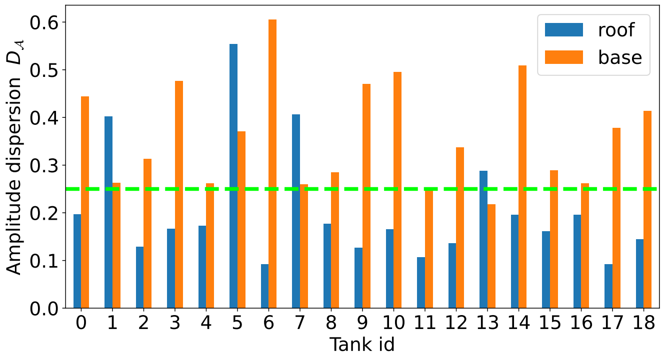

Figure 8.4: The measured amplitude dispersion for all tank ids at the fixed roof (A) in blue, and at the fixed base (B) in orange. The dashed green line indicates the threshold 0.25, usually used to detect stable reflectors in the PS technique.

On the other hand, Figure 8.3 shows the presence of some uncompensated factors affecting the phase. Indeed, we observe a dependence of the phase double difference on the orthogonal baseline for some tank couples, as can be seen in Figure 8.3b for the couple $(A^8, A^9)$. This indicates that there is an uncompensated topographic term due to inaccuracies in the simulated topographic phase $\phi^{topo}$. Furthermore, we also observe an occasional dependence on time, as can be seen in Figure 8.3d for couple $(A^8, A^{10})$. Note that for this plot, all interferograms are computed with respect to the first image in order to be able to show the evolution with time, i.e only for Figures 8.3c and 8.3d, the set $S$ of image couples is selected as $S = \{(0, j) \mid j = 1 \cdots N_I - 1\}$.

Moreover, we notice that the noise in the scatterplots increases when the corner is not a persistent scatterer, according to the traditional amplitude dispersion metric $D_{\mathcal{A}}$. We compute this metric on the roofs and bases of the tanks, $D_{\mathcal{A}}(A^k)$ and $D_{\mathcal{A}}(B^k)$ respectively, for $k = \{0 \cdots N_T - 1\}$. From Figure 8.4, we can make two observations:

- The amplitude dispersion of the base is globally higher than the amplitude dispersion of the roof (the value at the base is higher than the threshold of 0.25 for most of the tanks).
- The amplitude dispersion might indicate which scatterplots will be noisier. For instance, point $A^1$ for which the amplitude dispersion is high $(D_{\mathcal{A}}(A^1) = 0.4)$, is probably responsible for the noise seen in the scatterplot for couple $(A^0, A^1)$ in Figure 8.2d, whereas a trend can be seen in Figures 8.2c, 8.3a, 8.3c, for corners $(A^8, A^9, A^{10}, A^{15}, A^{16})$ which have low $D_{\mathcal{A}}$.

Finally, let us focus on the base corners (B). We already established that no clear trend emerges in Figure 8.2b, and that most amplitude dispersions are high. From Figure 8.5a, we see that this may be caused by the small reflections from the top of the floating roof, which often contaminate the base and drown it in clutter because of the layover effect. This phenomenon is emphasized by the fact that the tank is full at this date. However, a trend still sometimes emerges for some tank couples at the base, as seen in Figure 8.5b.

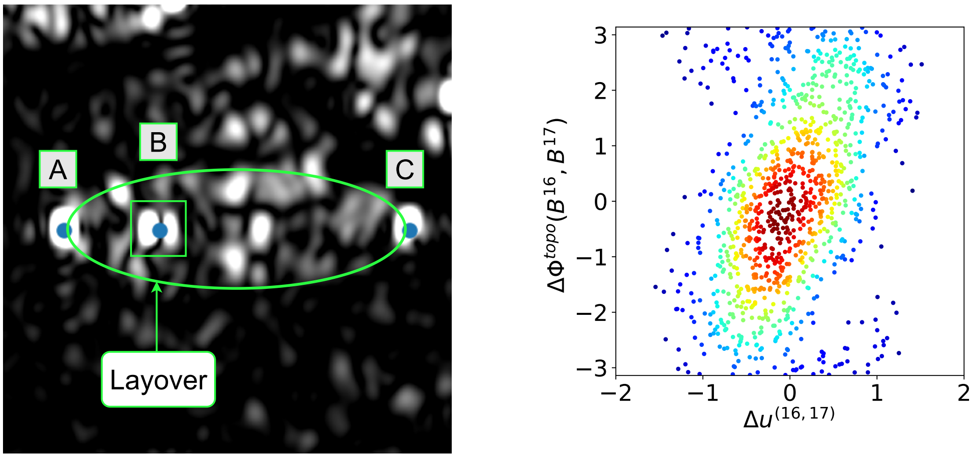

(a)

(b)

Figure 8.5: Base reflector behavior. On the left is a zoomed image of the tank 0. We clearly see the layover effect from the floating roof affecting the base and drowning it in clutter. On the right, we see a trend for tank couple (16, 17) between the phase double difference at the base and the fill ratio double difference.

## 8.4 Conclusion

In this study, we examined the relationship between the InSAR measurements on the fixed corners of floating roof storage tanks and the tank fill ratio inferred from the floating roof. We conclude that we sometimes observe a correlation between the fill ratio double difference and the phase double difference, mainly at the fixed roof corner of the tank. The trend suggests that a tank filling up induces a movement of the fixed roof corner away from the satellite in the order of 1 cm. On the other hand, some effects related to the residual topographic phase and some slow temporal trends may also be present. Furthermore, the noise level in the scatterplots is related to the amplitude dispersion index of the reflectors involved. In other words, unstable reflectors, according to traditional metrics, are less likely to exhibit visually compelling trends. Generally speaking, phase measurements from the fixed base reflector are noisy. We posit that this is due to the layover effect of the floating roof. Nonetheless, we can see some correlation between the phase and fill ratio double differences for some tank couples at the base.

All those challenges listed suggest the need to develop further adapted InSAR techniques to this specific use case. However, the experiments conducted on floating roof tanks are encouraging. In the future, by developing a method to infer a tank fill ratio from InSAR measurements, one could attempt to apply the same methodology on fixed roof tanks. It would then be possible to measure the fixed roof tank fill ratio from the small millimetric deformations of its fixed corners.

# 9 Conclusion

In this thesis, we have revisited various parts of the interferometric pipeline, mainly for Sentinel-1. Indeed, our goal was to design an efficient, precise, optimized, and automated processing chain. This is related to our end application which is monitoring several small assets around the world, which might exhibit complex deformation phenomena. Therefore, it was necessary to have an in-depth understanding of the different stages of the InSAR workflow and a control of their precision. Even though our requirement to perform localized measurements was behind many choices in our research, most presented contributions can also benefit wide-area processing (WAP).

## Part I. Precise coregistration and geometric modeling

This part of the thesis focuses on various algorithms of the processing pipeline leading up to obtaining a precise coregistered time series of Sentinel-1 images, which is necessary for InSAR.

In Chapter 3, we study the deramping algorithms for Sentinel-1. Deramping is the operation that recenters the Fourier spectrum of the data by compensating the Doppler centroid frequency shift. It is a necessary step before resampling the image. On this topic, we found that a simple workflow suggested by ESA [Mir15] and DLR [YMPIG+16] consists of deramping each SLC image with the function provided in the metadata, resampling with a standard interpolator, and then reramping with the conjugate of the "resampled" deramping function. We then compared this method to the method in [Gra15] and found it to be analogous to applying the primary deramping function on the whole time series while accounting for the registration shifts. Even though we propose a variant as our own deramping method, it is probably wise to approach this proposition with nuance. What we propose was heavily inspired by [Gra15], and was already hinted previously in at least one instance [HNBM16], although this reference didn't go into the equations or the practical implementation. In the end, even though our proposed method might have advantages related to the reduction of computational operations, in the scope of the full interferometric pipeline, its speedup is probably negligible. Since gaining a few seconds in processing might not be worth the risk of inducing small errors or coherence loss, we eventually implemented ESA's approach in our software EOS-SAR.

In Chapter 4, we provide an open-source implementation (rpcfit) of an algorithm to fit the coefficients of RPC functions for modeling geolocation operations. We applied the algorithm successfully to fit Sentinel-1's physical camera model, with a precision of the order of $10^{-4}$ pixels. For experts in SAR geolocation models, fitting the RPC function might only be interesting for computational purposes to accelerate subsequent algorithms requiring multiple geolocation operations such as geocoding (resampling a SAR image to a geographic frame) or backgeocoding (the inverse operation). For SAR image vendors, it might be interesting to include fitted RPC functions as metadata, which would simplify the manipulation of the images and facilitate user uptake. We intend to perform more experiments on this topic of efficient SAR processing with RPC functions since it could also simplify the fusion of SAR with data coming from different sensors (optical, weather, DEM, GPS...).

In Chapter 5, we propose a method to obtain a geometrically precise time series of aligned Sentinel-1 burst mosaics. The method resamples SLC bursts while taking into account small corrections related to physical effects such as the atmospheric delay or processing-induced timing shifts. It is especially interesting for applications where requirements on the geometric precision of the Sentinel-1 mosaics or geolocation are high, such as speckle tracking or precise coregistration for interferometry. We showed that considering the shifts can be easily integrated into a geometrical coregistration pipeline such as the one in [YMPIG$^+$16], but the user needs to implement the various formulas for the corrections highlighted in [GSB$^+$20]. Note that future work might involve replacing affine resampling with a dense resampling procedure to improve the modeling of the shifts impacted by the topography. Another point to consider is that once the ETAD product [GLM$^+$22] is released, there may no longer be a requirement for geolocation to estimate the corrections. However, the method can still be employed in its current form, utilizing ETAD solely as a means to estimate the corrections. In any case, the takeaway message is that considering these corrections, in particular during burst resampling and stitching, will surely be beneficial for some applications. This is demonstrated by the future OPERA coregistered SLC products which will use ETAD-like corrections in the coregistration process [FBJ$^+$23]. In contrast with the OPERA product which uses geocoding on a geographic Coordinate Reference System (CRS), our method performs the coregistration on the common grid defined by the primary image in the SAR Range-Doppler frame. This allows subsequent processing related to the generation of sub-apertures (or looks), the application of spectral diversity techniques [SM00], and the exploitation of burst overlap areas [YMPIPJ19, GKMV16]. The method is activated by default in the EOS-SAR software. Note that the method in the software is optimized to work on a small Area Of Interest (AOI). Indeed, from the start of the process, when an AOI is defined, only the relevant data in each burst is read, resampled, and stitched. This way, when coupled with efficient windowed reading inside a burst, it is possible to obtain very quickly a precisely aligned Sentinel-1 time series of small crops containing data from potentially different bursts and different swaths.

## Part II. Exploring Deep Learning for InSAR

This part of the thesis explores the potential of Deep Learning methods currently available for solving some InSAR tasks automatically.

In Chapter 6, we look at $\Phi$-Net [SGRB21], a method that uses a convolutional neural network on InSAR patches to predict the denoised InSAR phase and the estimated coherence. We also provide an online demo to reproduce the experiments. We confirmed the superior estimation performance of $\Phi$-Net w.r.t. the simple boxcar filter. We also noticed discontinuities in some fringes of the phase images. To mitigate this effect, it would be therefore interesting to develop $\Phi$-Net into a fully convolutional network applied on the whole InSAR image instead of the patch-based approach. In any case, $\Phi$-Net seems to be already advantageous and the application of Deep Learning for this task of phase denoising and coherence estimation is suitable. Indeed, Deep Learning networks have demonstrated their performance in image denoising tasks [ZZC+17], and this might also be the way to go with InSAR phase denoising and coherence estimation.

In Chapter 7, we examine the performance of a phase unwrapping Deep Learning method [PD21], and provide an online demo as well. The method showed good performance on in-domain data, but the results naturally degraded on out-of-domain data. What is slightly concerning is the fact that the network jointly performs the tasks of phase unwrapping and phase denoising. We observed how this denoising can filter some of the turbulent atmospheric simulations from the result. It would be better suited in the future to develop methods that only perform phase unwrapping, which would give more control over the potential loss of information induced by denoising.

## Part III. DInSAR Application

In this part, we perform DInSAR experiments for a challenging novel application. Indeed, Chapter 8 shows the potential of DInSAR in measuring the crude oil volume of storage tanks from the deformation of some of their reflectors. What is noteworthy is the fact that the storage tanks are generally made of steel, and have a fixed corner on the roof formed between the facade and the maintenance platform. The platform is circular and the corner's reflection will generally be good from the different viewpoints. Thus storage tanks are structures that are actively filled and emptied, on which we have some decent "corner reflectors", undergoing complex deformation phenomena. Hence, this use case should be interesting for the InSAR community since it is not conventional. To elaborate on the complexity of the problem, since the fill ratio might change drastically between consecutive acquisitions (from empty to filled or vice-versa), the deformation will exhibit fast temporal variations. Furthermore, the deformation is very localized spatially because it is related to each tank fill ratio. We are still unsure as to what is causing the movement of the fixed reflector on the roof. Among the different options is the loading effect of the fluid which might cause a localized subsidence when the tank fills up. Another potential cause is the stress of the fluid on the tank walls which might cause a deformation of the structure. Finally, thermal effects on the steel tanks might also be present, if the coefficient of thermal expansion varies with the crude oil volume for example. In any case, the deformation occurring should be very localized spatially. Indeed, we found that the relative deformation between reflectors on neighboring tanks is informative, which probably indicates that the impact of change in oil volume in one tank is minimal on its neighbors. In short, the deformation phenomenon is not typical, and tailored processing should yield better results than a generic pipeline. Our research has highlighted these issues, but providing a comprehensive answer to these questions proved to be difficult. How can we unwrap the phase without making smoothness assumptions temporally and to a lesser extent spatially? How can we perform temporal atmospheric filtering when the deformation has similar temporal behavior to the atmosphere? How much is the resolution of Sentinel-1 a limiting factor in the measurements? Future research in advanced DInSAR could focus more on these challenging use cases, especially on what can be achieved with Sentinel-1.

## Final remarks

Performing localized measurements on predefined assets is not the most predominant application for InSAR. In fact, recent trends show a tendency for Wide Area Processing (WAP) [AGPB13, MDZ+19, LSG+20, TCD+21, CSM+20], which is completely justified by the need to scan large areas on the scale of nations or continents for the detection of deformation events. However, WAP suffers from various limitations:

- Computational burden: because of the large amount of data.
- Complexity: The pipelines that are used to produce the results contain many processing steps. Also, a lot of filtering is usually done, which makes it hard to interpret the results.
- Generic: Only the most common use cases are covered.

The most recent example of WAP can be found in the European Ground Motion Service (EGMS) [CSM+20], which mainly provides the deformation products over most of the European continent. Level 2 (L2) EGMS measurements are sampled at the full Sentinel-1 resolution, because of the use of the Persistent Scatter (PS) technique. In this sense, these measurements are obviously interesting for localized insights on assets as well and cover the needs of most users. However, in some cases, the generic processor will fail to capture the real deformation phenomenon. This is the typical scenario in the presence of very high and nonlinear displacement rates, such as for storage tanks as seen in Chapter 8 or open pit mines [CSM+20], where an ad hoc approach needs to be set up. It would be therefore interesting to continue to push the boundaries on challenging use cases for Sentinel-1, in particular on localized assets where measurements need to be done with a few pixels and with rapidly changing deformation.

# Bibliography

[AAD$^+$22] Roland Akiki, Jeremy Anger, Carlo De Franchis, Gabriele Facciolo, Jean Michel Morel, and Raphael Grandin. Improved Sentinel-1 IW Burst Stitching Through Geolocation Error Correction Considerations. In *International Geoscience and Remote Sensing Symposium (IGARSS)*, pages 3404–3407. IEEE, 2022.

[AAdF$^+$er] Roland Akiki, Jérémy Anger, Carlo de Franchis, Gabriele Facciolo, Jean-Michel Morel, and Raphaël Grandin. A brief evaluation of InSAR phase denoising and coherence estimation with $\Phi$ -Net. *Image Processing On Line*, submitted paper.

[AAdF$^+$nt] Roland Akiki, Jérémy Anger, Carlo de Franchis, Gabriele Facciolo, and Jean-Michel Morel. Method, device and storage medium for reconstructing a corrected mosaic image from burst images, submitted patent.

[ADB18] Homa Ansari, Francesco De Zan, and Richard Bamler. Efficient Phase Estimation for Interferogram Stacks. *IEEE Transactions on Geoscience and Remote Sensing*, 56(7):4109–4125, 2018.

[AdFF$^+$22] Roland Akiki, Carlo de Franchis, Gabriele Facciolo, Jean-Michel Morel, and Raphaël Grandin. Phase Unwrapping using a Joint CNN and SQD-LSTM Network. *Image Processing On Line*, 12:378–388, oct 2022.

[AdFF$^+$23] Roland Akiki, Carlo de Franchis, Gabriele Facciolo, Raphaël Grandin, and Jean-Michel Morel. On The Potential Of Insar For Estimating Crude Oil Volume Changes From The Deformation Of Storage Tanks. In *International Geoscience and Remote Sensing Symposium (IGARSS)*, pages 7993–7996. IEEE, 2023.

[AdFF$^+$nt] Roland Akiki, Carlo de Franchis, Gabriele Facciolo, Raphaël Grandin, and Jean-Michel Morel. Method, device and computer program for measuring a difference of fill ratio of a tank, submitted patent.

[AGdF$^+$21] Roland Akiki, Raphaël Grandin, Carlo de Franchis, Gabriele Facciolo, and Jean Michel Morel. A Comparative Study of Deramping Techniques for Sentinel-1 Tops in the Context of Interferometry. In *International Geoscience and Remote Sensing Symposium (IGARSS)*, pages 3372–3375. IEEE, 2021.

[AGPB13] Nico Adam, Fernando Rodriguez Gonzalez, Alessandro Parizzi, and Ramon Brcic. Wide area Persistent Scatterer Interferometry: Current developments, algorithms and examples. In *International Geoscience and Remote Sensing Symposium (IGARSS)*, pages 1857–1860, 2013.

[AMdF$^+$21] Roland Akiki, Roger Marí, Carlo de Franchis, Jean Michel Morel, and Gabriele Facciolo. Robust Rational Polynomial Camera Modelling for Sar and Pushbroom Imaging. In *International Geoscience and Remote Sensing Symposium (IGARSS)*, pages 7908–7911. IEEE, 2021.

[BAM18] Ross A. Beyer, Oleg Alexandrov, and Scott McMichael. The Ames Stereo Pipeline: NASA's Open Source Software for Deriving and Processing Terrain Data. *Earth and Space Science*, 5(9):537–548, 2018.

[BE05] Richard Bamler and Michael Eineder. Accuracy of differential shift estimation by correlation and split-bandwidth interferometry for wideband and Delta-k SAR systems. *IEEE Geoscience and Remote Sensing Letters*, 2(2):151–155, 2005.

[BFLS02] Paolo Berardino, Gianfranco Fornaro, Riccardo Lanari, and Eugenio Sansosti. A new algorithm for surface deformation monitoring based on small baseline differential SAR interferograms. *IEEE Transactions on Geoscience and Remote Sensing*, 40(11):2375–2383, 2002.

[BKHB16] Marc Bosch, Zachary Kurtz, Shea Hagstrom, and Myron Brown. A multiple view stereo benchmark for satellite imagery. In *Proceedings - Applied Imagery Pattern Recognition Workshop*, pages 1–9. IEEE, 2016.

[BPPJL20] Anǵelique Benoit, Beatrice Pinel-Puysśegur, Romain Jolivet, and Ćecile Lasserre. CorPhU: An algorithm based on phase closure for the correction of unwrapping errors in SAR interferometry. *Geophysical Journal International*, 221(3):1959–1970, 2020.

[CAT$^+$07] Ferdaous Chaabane, Antonio Avallone, Florence Tupin, Pierre Briole, and Henri Maître. A multitemporal method for correction of tropospheric effects in differential SAR interferometry: Application to the gulf of corinth earthquake. *IEEE Transactions on Geoscience and Remote Sensing*, 45(6):1605–1615, 2007.

[CBGE18] Xiaoying Cong, Ulrich Balss, Fernando Rodriguez Gonzalez, and Michael Eineder. Mitigation of tropospheric delay in SAR and InSAR using NWP data: Its validation and application examples. *Remote Sensing*, 10(10):1515, sep 2018.

[CDLB07] O. Cavalié, M. P. Doin, C. Lasserre, and P. Briole. Ground motion measurement in the Lake Mead area, Nevada, by differential synthetic aperture radar interferometry time series analysis: Probing the lithosphere rheological structure. *Journal of Geophysical Research: Solid Earth*, 112(3):1–18, 2007.

[CHL17] Gong Cheng, Junwei Han, and Xiaoqiang Lu. Remote Sensing Image Scene Classification: Benchmark and State of the Art. *Proceedings of the IEEE*, 105(10):1865–1883, 2017.

[CMCG$^+$16] Michele Crosetto, Oriol Monserrat, María Cuevas-González, Núria Devanthéry, and Bruno Crippa. Persistent Scatterer Interferometry: A review. *ISPRS Journal of Photogrammetry and Remote Sensing*, 115:78–89, 2016.

[CMM12] Mario Costantini, Fabio Malvarosa, and Federico Minati. A general formulation for redundant integration of finite differences and phase unwrapping on a sparse multidimensional domain. *IEEE Transactions on Geoscience and Remote Sensing*, 50(3):758–768, 2012.

[Cos98] Mario Costantini. A novel phase unwrapping method based on network programming. *IEEE Transactions on Geoscience and Remote Sensing*, 36(3):813–821, 1998.

[CSM$^+$20] Michele Crosetto, Lorenzo Solari, Marek Mróz, Joanna Balasis-Levinsen, Nicola Casagli, Michaela Frei, Anneleen Oyen, Dag Anders Moldestad, Luke Bateson, Luca Guerrieri, Valerio Comerci, and Henrik Steen Andersen. The evolution of wide-area DInSAR: From regional and national services to the European ground motion service. *Remote Sensing*, 12(12):1–20, 2020.

[Cur82] John C. Curlander. Location of Spaceborne SAR Imagery. *IEEE Transactions on Geoscience and Remote Sensing*, GE-20(3):359–364, 1982.

[CW05] Ian G Cumming and Frank H Wong. *Digital signal processing of synthetic aperture radar data.* Artech House, 2005.

[CZ01] Curtis W Chen and Howard A Zebker. Two-dimensional phase unwrapping with use of statistical models for cost functions in nonlinear optimization. *Journal of the Optical Society of America (JOSA) A*, 18(2):338–351, 2001.

[DCM$^+$14] Núria Devanthéry, Michele Crosetto, Oriol Monserrat, María Cuevas-González, and Bruno Crippa. An approach to persistent scatterer interferometry. *Remote Sensing*, 6(7):6662–6679, 2014.

[DDT11] Charles Alban Deledalle, Loïc Denis, and Florence Tupin. NL-InSAR: Nonlocal interferogram estimation. *IEEE Transactions on Geoscience and Remote Sensing*, 49(4):1441–1452, 2011.

[DDT$^+$15] Charles Alban Deledalle, Loic Denis, Florence Tupin, Andreas Reigber, and Marc Jager. NL-SAR: A unified nonlocal framework for resolution-preserving (Pol)(In)SAR denoising. *IEEE Transactions on Geoscience and Remote Sensing*, 53(4):2021–2038, apr 2015.

[De 14] Francesco De Zan. Accuracy of incoherent speckle tracking for circular gaussian signals. *IEEE Geoscience and Remote Sensing Letters*, 11(1):264–267, 2014.

[DFKE07] Kostadin Dabov, Alessandro Foi, Vladimir Katkovnik, and Karen Egiazarian. Image denoising by sparse 3-D transform-domain collaborative filtering. *IEEE Transactions on Image Processing*, 16(8):2080–2095, 2007.

[DFL$^+$21] Yanan Du, Haiqiang Fu, Lin Liu, Guangcai Feng, Xing Peng, and Debao Wen. Orbit error removal in InSAR/MTInSAR with a patch-based polynomial model. *International Journal of Applied Earth Observation and Geoinformation*, 102:102438, oct 2021.

[dFMLGF15] Carlo de Franchis, Enric Meinhardt-Llopis, Daniel Greslou, and Gabriele Facciolo. Attitude Refinement for Orbiting Pushbroom Cameras: a Simple

Polynomial Fitting Method. *Image Processing On Line*, 5(july):328–361, 2015.

[DLA+20] Carlo De Franchis, Guillaume Lostis, Hefdhi Abdennadher, Pablo Arias, Thomas Madaule, Axel Davy, Sylvain Calisti, Jean-Michel Morel, Raffaele Grompone, and Gabriele Facciolo. Method and system for remotely measuring the volume of liquid stored in external floating roof tanks, US Patent 10,672,139, 2020.

[FAS17] Heresh Fattahi, Piyush Agram, and Mark Simons. A Network-Based Enhanced Spectral Diversity Approach for TOPS Time-Series Analysis. *IEEE Transactions on Geoscience and Remote Sensing*, 55(2):777–786, 2017.

[FBJ+23] Heresh Fattahi, Virginia Brancato, Seongsu Jeong, Scott Staniewicz, Mary Grace Bato, Zhong Lu, Jinwoo Kim, Kang Liang, Simran Sangha, Bruce Chapman, Alexander Handwerger, Steven Chan, and David Bekaert. Impact of ETAD-like corrections on OPERA Coregistered Single Look Complex products from Sentinel-1 data. In *FRINGE 2023 Workshop*, 2023.

[FDG06] C. S. Fraser, G. Dial, and J. Grodecki. Sensor orientation via RPCs. *ISPRS Journal of Photogrammetry and Remote Sensing*, 60(3):182–194, 2006.

[FFN+11] Alessandro Ferretti, Alfio Fumagalli, Fabrizio Novali, Claudio Prati, Fabio Rocca, and Alessio Rucci. A new algorithm for processing interferometric data-stacks: SqueeSAR. *IEEE Transactions on Geoscience and Remote Sensing*, 49(9):3460–3470, 2011.

[FPC23] Alessandro Ferretti, Emanuele Passera, and Renalt Capes. End-to-end implementation and operation of the European Ground Motion Service (EGMS): Algorithm Theoretical Basis Document. Technical report, ORIGINAL Consortium, 2023.

[FPR00] Alessandro Ferretti, Claudio Prati, and Fabio Rocca. Nonlinear subsidence rate estimation using permanent scatterers in differential SAR interferometry. *IEEE Transactions on Geoscience and Remote Sensing*, 38(5 I):2202–2212, 2000.

[FPR01] Alessandro Ferretti, Claudio Prati, and Fabio Rocca. Permanent scatterers in SAR interferometry. *IEEE Transactions on Geoscience and Remote Sensing*, 39(1):8–20, 2001.

[FRC+07] Tom G. Farr, Paul A. Rosen, Edward Caro, Robert Crippen, Riley Duren, Scott Hensley, Michael Kobrick, Mimi Paller, Ernesto Rodriguez, Ladislav Roth, David Seal, Scott Shaffer, Joanne Shimada, Jeffrey Umland, Marian Werner, Michael Oskin, Douglas Burbank, and Douglas E. Alsdorf. The Shuttle Radar Topography Mission. *Reviews of Geophysics*, 45(2):2004, jun 2007.

[GDB+12] Raphaël Grandin, Marie Pierre M-P. Doin, Laurent Bollinger, Béatrice Pinel-Puysségur, Gabriel Ducret, Romain Jolivet, and Soma Nath Sapkota. Long-term growth of the Himalaya inferred from interseismic InSAR measurement. *Geology*, 40(12):1059–1062, 2012.

[GKMV16] R. Grandin, E. Klein, M. Métois, and C. Vigny. Three-dimensional displacement field of the 2015 Mw8.3 Illapel earthquake (Chile) from across-and along-track Sentinel-1 TOPS interferometry. *Geophysical Research Letters*, 43(6):2552–2561, 2016.

[GLM$^+$22] Christoph Gisinger, Ludivine Libert, Petar Marinkovic, Lukas Krieger, Yngvar Larsen, Antonio Valentino, Helko Breit, Ulrich Balss, Steffen Suchandt, Thomas Nagler, Michael Eineder, and Nuno Miranda. The Extended Timing Annotation Dataset for Sentinel-1-Product Description and First Evaluation Results. *IEEE Transactions on Geoscience and Remote Sensing*, 60:1–22, 2022.

[GP98] D C Ghiglia and M D Pritt. Two-dimensional phase unwrapping: theory, algorithms, and software. *A Wiley Interscience Publication*, 1998.

[Gra15] Raphaël Grandin. Interferometric processing of SLC Sentinel-1 TOPS data. *European Space Agency, (Special Publication) ESA SP*, SP-731(1):1–14, 2015.

[Gro01] J. Grodecki. IKONOS Stereo Feature Extraction - RPC Approach. In *ASPRS Annual Conference St. Louis*, 2001.

[GSB$^+$20] Christoph Gisinger, Adrian Schubert, Helko Breit, Matthew Garthwaite, Ulrich Balss, Martin Willberg, David Small, Michael Eineder, and Nuno Miranda. In-Depth Verification of Sentinel-1 and TerraSAR-X Geolocation Accuracy Using the Australian Corner Reflector Array. *IEEE Transactions on Geoscience and Remote Sensing*, 59(2):1154–1181, 2020.

[GW98] Richard M. Goldstein and Charles L. Werner. Radar interferogram filtering for geophysical applications. *Geophysical Research Letters*, 25(21):4035–4038, 1998.

[GWV96] D. Geudtner, R. Winter, and P. W. Vachon. Flood monitoring using ERS-1 SAR interferometry coherence maps. In *International Geoscience and Remote Sensing Symposium (IGARSS)*, volume 2, pages 966–968. IEEE, 1996.

[GZW88] Richard M. Goldstein, Howard A. Zebker, and Charles L. Werner. Satellite radar interferometry: Two-dimensional phase unwrapping. *Radio Science*, 23(4):713–720, 1988.

[Han02] Ramon Hanssen. *Radar Interferometry, Data Interpretation and Error Analysis.* Kluwer Academic Publishers, 2002.

[HBDK15] Hao Hongxing, Jose M. Bioucas-Dias, and Vladimir Katkovnik. Interferometric phase image estimation via sparse coding in the complex domain. *IEEE Transactions on Geoscience and Remote Sensing*, 53(5):2587–2602, 2015.

[HdFFM21] Charles Hessel, Carlo de Franchis, Gabriele Facciolo, and Jean Michel Morel. A GLOBAL REGISTRATION METHOD FOR SATELLITE IMAGE SERIES. In *International Geoscience and Remote Sensing Symposium (IGARSS)*, pages 3121–3124. IEEE, 2021.

[HG23] Arthur Hauck and Raphael Grandin. Tracking Topographic Changes on Erupting Volcanoes Using Radar Satellite Imagery. In *FRINGE 2023 Workshop*, 2023.

[HIKK08] T. Hobiger, R. Ichikawa, Y. Koyama, and T. Kondo. Fast and accurate ray-tracing algorithms for real-time space geodetic applications using numerical weather models. *Journal of Geophysical Research Atmospheres*, 113(20):1–14, 2008.

[HNBM16] Dinh Ho Tong Minh, Yen Nhi Ngo, Nicolas Baghdadi, and Pierre Maurel. TomoSAR platform: A new Irstea service as demand for SAR, interferometry, polarimetry and tomography. In *Proc. ESA Living Planet Symp*, volume SP-740, pages 1—-8, 2016.

[HO93] Per Christian Hansen and Dianne Prost O'Leary. The Use of the L-Curve in the Regularization of Discrete Ill-Posed Problems. *SIAM Journal on Scientific Computing*, 14(6):1487–1503, 1993.

[HZ07] Andrew Hooper and Howard A. Zebker. Phase unwrapping in three dimensions with application to InSAR time series. *Journal of the Optical Society of America A*, 24(9):2737, 2007.

[HZRS15] Kaiming He, Xiangyu Zhang, Shaoqing Ren, and Jian Sun. Delving deep into rectifiers: Surpassing human-level performance on imagenet classification. In *Proceedings of the IEEE International Conference on Computer Vision*, volume 2015 International Conference on Computer Vision, ICCV 2015, pages 1026–1034, 2015.

[JGL$^+$11] R Jolivet, R Grandin, C Lasserre, M. P. Doin, and G Peltzer. Systematic InSAR tropospheric phase delay corrections from global meteorological reanalysis data. *Geophysical Research Letters*, 38(17), 2011.

[JKLY16] Jungkyo Jung, Duk Jin Kim, Marco Lavalle, and Sang Ho Yun. Coherent Change Detection Using InSAR Temporal Decorrelation Model: A Case Study for Volcanic Ash Detection. *IEEE Transactions on Geoscience and Remote Sensing*, 54(10):5765–5775, oct 2016.

[JPS$^+$08] Michael Jehle, Donat Perler, David Small, Adrian Schubert, and Erich Meier. Estimation of atmospheric path delays in TerraSAR-X data using models vs. measurements. *Sensors*, 8(12):8479–8491, dec 2008.

[KH08] Bert Kampes and Ramon Hanssen. Delft object-oriented radar interferometric software: Users manual and technical documentation. Technical report, Delft University of Technology, 2008.

[KHP04] B M Kampes, R F Hanssen, and Z Perski. Radar interferometry with public domain tools. In *FRINGE 2003 Workshop*, volume 550, 2004.

[KZM$^+$18] Navaneeth Kamballur Kottayil, Aaron Zimmer, Subhayan Mukherjee, Xinyao Sun, Parwant Ghuman, and Irene Cheng. Accurate Pixel-Based Noise Estimation for InSAR Interferograms. In *2018 IEEE SENSORS*, pages 1–4. IEEE, IEEE, 2018.

[LCRCPIP21] Alejandro Linde-Cerezo, Marc Rodriguez-Cassola, Pau Prats-Iraola, and Muriel Pinheiro. Systematic Comparison of Backgeocoding Algorithms for SAR Processing and Simulation Environments. In *EUSAR 2021; 13th European Conference on Synthetic Aperture Radar*, pages 383–386, 2021.

[Lee98] Jong Sen Lee. A new technique for noise filtering of sar interferometric phase images. *IEEE Transactions on Geoscience and Remote Sensing*, 36(5 PART 1):1456–1465, 1998.

[LJH15] Tengfei Long, Weili Jiao, and Guojin He. RPC estimation via $\ell_1$-norm regularized least squares (L1LS). *IEEE Transactions on Geoscience and Remote Sensing*, 53(8):4554–4567, 2015.

[LMM94] Jong Sen Lee, Allen R. Miller, and Stephen A. Mango. Intensity and Phase Statistics of Multilook Polarimetric and Interferometric SAR Imagery. *IEEE Transactions on Geoscience and Remote Sensing*, 32(5):1017–1028, 1994.

[LMM$^+$04] Ricardo Lanari, Oscar Mora, Michele Manunta, Jordi J. Mallorquí, Paolo Berardino, and Eugenio Sansosti. A small-baseline approach for investigating deformations on full-resolution differential SAR interferograms. *IEEE Transactions on Geoscience and Remote Sensing*, 42(7):1377–1386, 2004.

[LQDT$^+$09] Penélope López-Quiroz, Marie Pierre Doin, Florence Tupin, Pierre Briole, and Jean Marie Nicolas. Time series analysis of Mexico City subsidence constrained by radar interferometry. *Journal of Applied Geophysics*, 69(1):1–15, sep 2009.

[LS21] Carlos Villamil Lopez and Uwe Stilla. Monitoring of Oil Tank Filling with Spaceborne SAR Using Coherent Scatterers. *IEEE Journal of Selected Topics in Applied Earth Observations and Remote Sensing*, 14:5638–5655, 2021.

[LSG$^+$20] Milan Lazeckỳ, Karsten Spaans, Pablo J. González, Yasser Maghsoudi, Yu Morishita, Fabien Albino, John Elliott, Nicholas Greenall, Emma Hatton, Andrew Hooper, Daniel Juncu, Alistair McDougall, Richard J. Walters, C. Scott Watson, Jonathan R. Weiss, and Tim J. Wright. LiCSAR: An automatic InSAR tool for measuring and monitoring tectonic and volcanic activity. *Remote Sensing*, 12(15):2430, 2020.

[MdFML$^+$21] Roger Marí, Carlo de Franchis, Enric Meinhardt-Llopis, Jérémy Anger, and Gabriele Facciolo. A generic bundle adjustment methodology for indirect rpc model refinement of satellite imagery. *Image Processing On Line*, 11:344–373, nov 2021.

[MDMLF19] Roger Mari, Carlo De Franchis, Enric Meinhardt-Llopis, and Gabriele Facciolo. To bundle adjust or not: A comparison of relative geolocation correction strategies for satellite multi-view stereo. In *Proceedings - 2019 International Conference on Computer Vision Workshop, ICCVW 2019*, pages 2188–2196, 2019.

[MDZ$^+$19] Michele Manunta, Claudio De Luca, Ivana Zinno, Francesco Casu, Mariarosaria Manzo, Manuela Bonano, Adele Fusco, Antonio Pepe, Giovanni Onorato, Paolo Berardino, Prospero De Martino, and Riccardo Lanari. The Parallel SBAS Approach for Sentinel-1 Interferometric Wide Swath Deformation Time-Series Generation: Algorithm Description and Products Quality Assessment. *IEEE Transactions on Geoscience and Remote Sensing*, 57(9):6229–6281, 2019.

[MEA+22] R. Marí, T. Ehret, J. Anger, C. De Franchis, and G. Facciolo. L1B+: a Perfect Sensor Localization Model for Simple Satellite Stereo Reconstruction From Push-Frame Image Strips. In *ISPRS Annals of the Photogrammetry, Remote Sensing and Spatial Information Sciences*, volume 5, pages 137–143. Copernicus GmbH, may 2022.

[MHR20] Dinh Ho Tong Minh, Ramon Hanssen, and Fabio Rocca. Radar interferometry: 20 years of development in time series techniques and future perspectives. *Remote Sensing*, 12(9):1–18, 2020.

[Mir15] Nuno Miranda. Definition of the TOPS SLC deramping function for products generated by the S-1 IPF. Technical report, Tech. rep., European Space Agency, available at: https://earth. esa. int∼. . . , 2015.

[MMSP22] Pietro Mastro, Guido Masiello, Carmine Serio, and Antonio Pepe. Change Detection Techniques with Synthetic Aperture Radar Images: Experiments with Random Forests and Sentinel-1 Observations. *Remote Sensing*, 14(14):3323, jul 2022.

[MN22] Dinh Ho Tong Minh and Yen Nhi Ngo. Compressed SAR Interferometry in the Big Data Era. *Remote Sensing*, 14(2):390, jan 2022.

[NHWF15] Nassir Navab, Joachim Hornegger, William M. Wells, and Alejandro F. Frangi. Medical Image Computing and Computer-Assisted Intervention - MICCAI 2015: 18th International Conference Munich, Germany, October 5-9, 2015 proceedings, part III. *Lecture Notes in Computer Science (including subseries Lecture Notes in Artificial Intelligence and Lecture Notes in Bioinformatics)*, 9351(Cvd):12–20, 2015.

[NON22] Geoffrey O. Nwodo, Francis I. Okeke, and Nixon N Nduji. Application of Interferometric Synthetic Aperture Radar (InSAR) Technique in Monitoring the Deformation of Large Oil Storage Tanks. *World Journal of Research and Review*, 15(6):18–25, 2022.

[PD21] M V Perera and A De Silva. A Joint Convolutional and Spatial Quad-Directional LSTM Network for Phase Unwrapping. In *IEEE International Conference on Acoustics, Speech and Signal Processing (ICASSP)*, volume 2021-June, pages 4055–4059. IEEE, Institute of Electrical and Electronics Engineers Inc., 2021.

[PINYM+17] Pau Prats-Iraola, Matteo Nannini, Nestor Yague-Martinez, Muriel Pinheiro, Jun Su Kim, Francesco Vecchioli, Federico Minati, Mario Costantini, Sven Borgstrom, Prospero De Martino, Valeria Siniscalchi, Michael Foumelis, and Yves Louis Desnos. Interferometric investigations with the Sentinel-1 constellation. In *International Geoscience and Remote Sensing Symposium (IGARSS)*, volume 2017-July, pages 5537–5540. Institute of Electrical and Electronics Engineers Inc., dec 2017.

[PISM+12] Pau Prats-Iraola, Rolf Scheiber, Luca Marotti, Steffen Wollstadt, and Andreas Reigber. TOPS interferometry with terraSAR-X. *IEEE Transactions on Geoscience and Remote Sensing*, 50(8):3179–3188, 2012.

[PJJ94] S. M. Pandit, N. Jordache, and G. A. Joshi. Data-dependent systems methodology for noise-insensitive phase unwrapping in laser interferometric surface characterization. *Journal of the Optical Society of America A*, 11(10):2584, 1994.

[PL06] Antonio Pepe and Riccardo Lanari. On the extension of the minimum cost flow algorithm for phase unwrapping of multitemporal differential SAR interferograms. *IEEE Transactions on Geoscience and Remote Sensing*, 44(9):2374–2383, sep 2006.

[PMR+22] Muriel Pinheiro, Nuno Miranda, Andrea Recchia, Alessandro Cotrufo, Niccolo Franceschi, Riccardo Piantanida, Kersten Schmidt, Christoph Gisinger, Guillaume Hajduch, and Pauline Vincent. Sentinel-1 instruments status and product performance update for 2022. In *EUSAR 2022; 14th European Conference on Synthetic Aperture Radar*, volume 2022-July, pages 413–417, 2022.

[PRF+18] R. Piantanida, A. Recchia, N. Franceschi, A. Valentino, N. Miranda, A. Schubert, and D. Small. Accurate geometric calibration of sentinel-1 data. *Proceedings of the European Conference on Synthetic Aperture Radar, EUSAR*, 2018-June:63–68, 2018.

[PS94] Mark D. Pritt and Jerome S. Shipman. Least-Squares Two-Dimensional Phase Unwrapping Using FFT's. *IEEE Transactions on Geoscience and Remote Sensing*, 32(3):706–708, 1994.

[RBR+03] Alexander Rauscher, Markus Barth, Jürgen R. Reichenbach, Rudolf Stollberger, and Ewald Moser. Automated unwrapping of MR phase images applied to BOLD MR-venography at 3 tesla. *Journal of Magnetic Resonance Imaging*, 18(2):175–180, 2003.

[SBM+06] Eugenio Sansosti, Paolo Berardino, Michele Manunta, Francesco Serafino, and Gianfranco Fornaro. Geometrical SAR image registration. *IEEE Transactions on Geoscience and Remote Sensing*, 44(10):2861–2870, 2006.

[SCVP18] Francescopaolo Sica, Davide Cozzolino, Luisa Verdoliva, and Giovanni Poggi. The offset-compensated nonlocal filtering of interferometric phase. *Remote Sensing*, 10(9), 2018.

[SCZ+18] Francescopaolo Sica, Davide Cozzolino, Xiao Xiang Zhu, Luisa Verdoliva, and Giovanni Poggi. InSAR-BM3D: A Nonlocal Filter for SAR Interferometric Phase Restoration. *IEEE Transactions on Geoscience and Remote Sensing*, 56(6):3456–3467, 2018.

[SGB+23] Victor Navarro Sanchez, Christoph Gisinger, Ramon Brcic, Steffen Suchandt, Lukas Krieger, Thomas Fritz, Antonio Valentino, and Muriel Pinheiro. Advancing Sentinel-1 InSAR applications using ESA ' s extended timing annotation dataset product. In *IGARSS 2022-2022 IEEE International Geoscience and Remote Sensing Symposium*, pages 7878–7881, 2023.

[SGG20] G. E. Spoorthi, Rama Krishna Sai Subrahmanyam Gorthi, and Subrahmanyam Gorthi. PhaseNet 2.0: Phase Unwrapping of Noisy Data Based on Deep Learning Approach. *IEEE Transactions on Image Processing*, 29:4862–4872, 2020.

[SGRB21] Francescopaolo Sica, Giorgia Gobbi, Paola Rizzoli, and Lorenzo Bruzzone. Φ-Net: Deep Residual Learning for InSAR Parameters Estimation. *IEEE*

*Transactions on Geoscience and Remote Sensing*, 59(5):3917–3941, may 2021.

[SM00] Rolf Scheiber and Alberto Moreira. Coregistration of interferometric SAR images using spectral diversity. *IEEE Transactions on Geoscience and Remote Sensing*, 38(5 I):2179–2191, 2000.

[SS19] David Small and Adrian Schubert. Guide to Sentinel-1 Geocoding. Technical report, Remote Sensing Lab. Univ. Zurich (RSL), Zürich, Switzerland, 2019.

[TCD+21] Franck Thollard, Dominique Clesse, Marie Pierre Doin, Joëlle Donadieu, Philippe Durand, Raphaël Grandin, Cécile Lasserre, Christophe Laurent, Emilie Deschamps-Ostanciaux, Erwan Pathier, Elisabeth Pointal, Catherine Proy, and Bernard Specht. Flatsim: The form@ter large-scale multitemporal sentinel-1 interferometry service. *Remote Sensing*, 13(18):3734, sep 2021.

[TH01] C. V. Tao and Y. Hu. A comprehensive study of the rational function model for photogrammetric processing. *Photogrammetric Engineering and Remote Sensing*, 67(12):1347–1357, 2001.

[TN15] F Tupin and J Nicolas. *Les Bases de l'Imagerie Radar à Synthèse d'Ouverture : Partie 1.* Telecom ParisTech, 2015.

[TNM98] Emmanuel Trouvé, Jean Marie Nicolas, and Henri Maître. Improving phase unwrapping techniques by the use of local frequency estimates. *IEEE Transactions on Geoscience and Remote Sensing*, 36(6):1963–1972, 1998.

[VFP22] Sergio Vitale, Giampaolo Ferraioli, and Vito Pascazio. A CNN Based Solution for InSAR Phase Denoising. In *International Geoscience and Remote Sensing Symposium (IGARSS)*, volume 2022-July, pages 931–934. IEEE, 2022.

[VFPS22] Sergio Vitale, Giampaolo Ferraioli, Vito Pascazio, and Gilda Schirinzi. InSAR-MONet: Interferometric SAR Phase Denoising Using a Multiobjective Neural Network. *IEEE Transactions on Geoscience and Remote Sensing*, 60, 2022.

[VTCB04] Gabriel Vasile, Emmanuel Trouvé, Mihai Ciuc, and Vasile Buzuloiu. General adaptive-neighborhood technique for improving synthetic aperture radar interferometric coherence estimation. *Journal of the Optical Society of America A*, 21(8):1455, 2004.

[web] User Guides - Sentinel-1 SAR - Interferometric Wide Swath - Sentinel Online - Sentinel Online.

[WWS+16] Urs Wegnüller, Charles Werner, Tazio Strozzi, Andreas Wiesmann, Othmar Frey, and Maurizio Santoro. Sentinel-1 Support in the GAMMA Software. *Procedia Computer Science*, 100:1305–1312, 2016.

[WZS16] Yiran Wang, Ye Zhang, and Nan Su. RPC estimation via feature points for urban areas. In *International Geoscience and Remote Sensing Symposium (IGARSS)*, volume 2016-November, pages 6684–6687, 2016.

[WZY+17] Taoyang Wang, Guo Zhang, Lei Yu, Ruishan Zhao, Mingjun Deng, and Kai Xu. Multi-Mode GF-3 Satellite Image Geometric Accuracy Verification Using the RPC Model. *Sensors*, 17(9), sep 2017.

[XGLX20] Gang Xu, Yandong Gao, Jinwei Li, and Mengdao Xing. InSAR Phase Denoising: A Review of Current Technologies and Future Directions. *IEEE Geoscience and Remote Sensing Magazine*, 8(2):64–82, 2020.

[YDLQ+12] Yajing Yan, Marie Pierre Doin, Penélope López-Quiroz, Florence Tupin, Bénédicte Fruneau, Virginie Pinel, and Emmanuel Trouvé. Mexico City subsidence measured by InSAR time series: Joint analysis using PS and SBAS approaches. *IEEE Journal of Selected Topics in Applied Earth Observations and Remote Sensing*, 5(4):1312–1326, 2012.

[YLPC18] Chen Yu, Zhenhong Li, Nigel T. Penna, and Paola Crippa. Generic Atmospheric Correction Model for Interferometric Synthetic Aperture Radar Observations. *Journal of Geophysical Research: Solid Earth*, 123(10):9202–9222, 2018.

[YLY+19] Hanwen Yu, Yang Lan, Zhihui Yuan, Junyi Xu, and Hyongki Lee. Phase unwrapping in InSAR : A review. *IEEE Geoscience and Remote Sensing Magazine*, 7(1):40–58, 2019.

[YMDPI17] Nestor Yague-Martinez, Francesco De Zan, and Pau Prats-Iraola. Coregistration of Interferometric Stacks of Sentinel-1 TOPS Data. *IEEE Geoscience and Remote Sensing Letters*, 14(7):1002–1006, jul 2017.

[YMPIG+16] Nestor Yague-Martinez, Pau Prats-Iraola, Fernando Rodriguez Gonzalez, Ramon Brcic, Robert Shau, Dirk Geudtner, Michael Eineder, and Richard Bamler. Interferometric Processing of Sentinel-1 TOPS Data. *IEEE Transactions on Geoscience and Remote Sensing*, 54(4):2220–2234, 2016.

[YMPIPJ19] Nestor Yague-Martinez, Pau Prats-Iraola, Muriel Pinheiro, and Marc Jaeger. Exploitation of burst overlapping areas of TOPS data. Application to sentinel-1. In *International Geoscience and Remote Sensing Symposium (IGARSS)*, pages 2066–2069. Institute of Electrical and Electronics Engineers Inc., 2019.

[Zeb21] Howard Zebker. Accuracy of a model-free algorithm for temporal insar tropospheric correction. *Remote Sensing*, 13(3):1–9, 2021.

[ZFL+10] Guo Zhang, Wen Bo Fei, Zhen Li, Xiaoyong Zhu, and De Ren Li. Evaluation of the RPC model for spaceborne SAR imagery. *Photogrammetric Engineering and Remote Sensing*, 76(6):727–733, 2010.

[ZHB+11] Lu Zhang, Xueyan He, Timo Balz, Xiaohong Wei, and Mingsheng Liao. Rational function modeling for spaceborne SAR datasets. *ISPRS Journal of Photogrammetry and Remote Sensing*, 66(1):133–145, 2011.

[ZYL20] Lifan Zhou, Hanwen Yu, and Yang Lan. Deep Convolutional Neural Network-Based Robust Phase Gradient Estimation for Two-Dimensional Phase Unwrapping Using SAR Interferograms. *IEEE Transactions on Geoscience and Remote Sensing*, 58(7):4653–4665, 2020.

[ZYLX21a] Lifan Zhou, Hanwen Yu, Yang Lan, and Mengdao Xing. Artificial Intelligence in Interferometric Synthetic Aperture Radar Phase Unwrapping: A Review. *IEEE Geoscience and Remote Sensing Magazine*, 9(2):10–28, 2021.

[ZYLX21b] Lifan Zhou, Hanwen Yu, Yang Lan, and Mengdao Xing. Deep Learning-Based Branch-Cut Method for InSAR Two-Dimensional Phase Unwrapping. *IEEE Transactions on Geoscience and Remote Sensing*, 60:1–15, 2021.

[ZZC$^+$17] Kai Zhang, Wangmeng Zuo, Yunjin Chen, Deyu Meng, and Lei Zhang. Beyond a Gaussian denoiser: Residual learning of deep CNN for image denoising. *IEEE Transactions on Image Processing*, 26(7):3142–3155, 2017.